9-11-2006

Design and fabrication of silicon on insulator optical waveguide devices

Eric Harvey

Design and Fabrication of Silicon on Insulator Optical Waveguide Devices

By
Eric J. Harvey

A Thesis Submitted in
Partial Fulfillment
of the Requirements for the Degree of

MASTER OF SCIENCE
In
Electrical Engineering

Approved by:

Thesis Advisor:_____
Dr. Mustafa A.G. Abushagur

Committee Member:_____
Dr. Lynn Fuller

Committee Member:_____
Dr. Jayanti Venkataraman

Department Head:_____
Dr. Vincent Amuso

Department of Electrical Engineering
Kate Gleason College of Engineering
Rochester Institute of Technology
Rochester, New York
August 2006

Design and Fabrication of Silicon on Insulator Optical Waveguide Devices

I, Eric J. Harvey hereby grant the permission to the Wallace Library of the Rochester Institute of Technology to reproduce my thesis in whole or in part. Any reproduction will not be for commercial profit.

Date: _____ Author: _____

Acknowledgments

The work done on this thesis over the past year would have not been possible without the help of several people in and outside of RIT. I would like to thank my advisor and mentor Dr. Mustafa A.G. Abushagur most of all for the direction and support he has provided along the way. He has given me valuable insight and an intuitive view on the behavior of micro-optic structures, as well provided me with knowledge and tools required to test these waveguide devices.

I would also like to thank my committee members, Dr. Lynn Fuller, for his help in designing the process steps required to fabricate these waveguide structures and Dr. Jayanti Venkataraman, for her help in carefully reviewing the thesis and providing feedback. Both have been a tremendous help.

The SMFL staff, particularly Sean O'Brien, has given much of his time and patience in certifying me on the tools that were required for fabrication. PHD students Karthik Narayanan, and Ajay Pasupuleti, have also been an invaluable resource for learning how to use many of the tools in the SMFL. I would also like to thank the Electrical engineering department staff, Ms. Florence Layton, and Ms. Patti Vicari, for there help in bringing the thesis requirements together.

During the testing phase of this thesis Ousama Abushagur was a great help, lending his expertise and knowledge on handling optical fibers, and operating equipment such as the fiber splicer. In addition I would like to thank Gary Reisdorf, a friend, for helping machine the mounting brackets used in edge polishing the devices.

Finally I want to thank my family and friends for all there support, and encouragement.

Design and Fabrication of Silicon on Insulator

Optical Waveguide Devices

By

Eric J. Harvey

Masters of Science in Electrical Engineering

Abstract

In this thesis we present design, fabrication and testing of several photonic devices on a silicon-on-insulator (SOI) substrate. The historical developments in micro-optic technology including problems it has faced and its current state of maturity is outlined. The most recent integration trends of electronics and optics, particularly the transition of micro-optics to silicon on insulator platform will be reviewed. With this foundation in silicon photonics several rib waveguide structures including directional couplers, WDM couplers, y-branches and MMI splitters are designed, simulated, and fabricated on an SOI substrate. Beam propagation method (BPM) was used in the modeling of these devices. Computation time is reduced by using a least squared regression to predict coupler behavior and losses in devices with varying dimensions and shape. A fabrication procedure is developed, characterized and implemented. The final devices are tested, and qualitative results provided.

Table of Contents

List of Tables

List of Figures

Chapter 1: Background

1.1 Introduction

The goal of this thesis is to investigate the design and fabrication of several photonic devices on Silicon-On-Insulator (SOI) wafers. The historical developments in micro-optic technology including problems it has faced and its current state of maturity will be outlined. The most recent integration trends of electronics and optics, particularly the

transition of micro-optics to silicon on insulator platform will be studied. With this foundation in silicon photonics several waveguide structures including directional couplers, wavelength splitters, and y-branches are designed, simulated, and fabricated on an SOI platform to prove their viability and performance at RIT.

1.2 Advantages of Optics

Historically optics and electronics have been two very disconnected technologies, each filling a unique role, and deployed in solving very different engineering problems. Optics is classically used in vision and imaging systems, where as electronics is used for complex mathematical computations. Despite the fact that microelectronics has been able to achieve unprecedented integration, and complexity, it comes with many limitations as the need for sizes to shrink and speeds to increase continues. In theory, optics can complement many of these anticipated drawbacks. The greatest advantage of optics is that it involves the manipulation of a chargeless particle called the photon. Because photons have no charge, optical signals have negligible interference with each other, and thus low cross talk. Optical beams can coexist in the same guiding medium, or pass through each other, and retain their individual properties. Light also travels at speeds greater than the electron as it is not governed by particle mobility and drift velocity. Finally, optical processing is parallel in nature, allowing for various operations to be preformed simultaneously [1]. These advantages give optical systems superior bandwidth (on the order of petahertz), and speed as compared to an equivalent electrical system. Many of these advantages have been realized in fiber optic based communication systems

that have tremendous bandwidths. The powerful potential optics has in solving the problems being faced in evolving electronics makes it highly desirable. The Achilles heel for optics applications has been the size and integration of optical devices. Optical systems in general are much larger, typically limited to bench top setups that are impractical, and overly expensive to produce. There are also many device and integration related issues that have yet to be solved.

1.3 Microfabrication and its impact on electronics

Since the early 1990's the design of optical systems have been evolving from the manipulation of discreet components such as lenses, mirrors and fiber optics, to the fabrication of integrated micro and even nanometer sized photonic devices [2]. It is this miniaturization of optic components that has the potential to move optics into the domain of computation and signal processing. The semiconductor microfabercation technology, which has set the foundation for this revolution in optical system fabrication, first began in the electronics industry as a method to create integrated circuits (IC). The semiconductor microfabrication process consists of patterning a substrate, typically silicon (Si), using lithography, then etching, doping, or depositing material on the exposed surface. By repeating these steps various materials can be layered with specific patterns to create devices such as the transistor. The power of this process technology is that it allows many devices to be fabricated at the same time with near identical behavior, and interconnected to build complex circuits. Because each lithography layer is defined by a mask, wafers can be printed with a great degree of reproducibility. Such a high yield

wafer scale process technology allows compact circuits with billions of transistors, such as the microprocessor, to be produced at a relatively low cost [3].

The manufacturability of complex microelectronics has allowed for rapid growth of IC technology. In 2003 aggregate sales in the microelectronics industry exceeded 163 billion USD and are forecasted to grow to $219 billion by the end of 2006 [4]. This growth drives better processing technology. Today's transistors have gate lengths of 65nm and are continually shrinking, 45nm and 30nm processes are in development at Intel. These improvements and innovations made to microfabrication process technology and circuit design have allowed processors to advance according to Intel's co founder Gordon E. Moore. In 1965 Moore proposed that computing power will exponentially increase over time, doubling every twenty four months [5]. Now referred to as Moore's Law, this theory has held true and continues to drive the microelectronics industry as it sets the benchmark for future technology. However it is expected that such trends in silicon technology can only continue for the next ten years or so before size limitations and RF effects will force a fundamental shift in how computing is preformed. Micro-optics is one such option being considered for the next generation of computing technology. With the help of new innovative ideas such as optical interconnects, and possibly one day and optical computer it is expected that these advancements will continue for decades to come.

1.4 Advantages of silicon in microfabrication

Another component that is fundamental in the fabrication of such complex IC's, and future micro-optic devices has been the advent of a viable substrate. Today almost all IC's are manufactured on single crystalline silicon (SCS) wafers. In IC design silicon is used primarily for its electrical properties. As a semiconductor it can be doped with a wide variety of impurities, such as boron and phosphorus, to accurately control its electrical characteristics. Silicon is unique from many other semiconductors in that it has a natural oxide (SiO_2), that is adhering, an excellent electrical insulator as well as diffusion barrier, and highly selective to etching [6]. In fact many modern Complementary Metal Oxide Semiconductor (CMOS) processes use an SOI substrate as a starting point for device fabrication. SOI substrates consist of a thin layer of silicon dielectrically separated from the bulk silicon by a buried oxide layer, typically sapphire, or more recently SiO_2 [7]. The original use of such process technologies were for producing radiation hardened IC's, however they provide many other advantages as well. By isolating the device layer from the substrate, junction capacitances and leakage current are dramatically reduced, increasing switching speed and reducing the power consumption of devices [7]. Another advantage that makes silicon desirable for IC processing is its thermal properties. The high thermal conductivity of silicon allows for dense integration as heat generated by devices can be easily dissipated [6]. Mechanically SCS is far more resilient then most glasses, with a young's modulus similar to that of stainless steel, yield strength of more than three times that and a hardness comparative to quartz [8]. The durability of silicon has allowed for its use in the fabrication of micro-

mechanical structures such as springs, gears, cantilever beams, motors, and even micro-fluidic pumps. All these devices are categorized into what is called MEMS (Micro Electrical Mechanical Machines). These silicon based devices are used in everything from printer cartridges, to the micro-mirrors for dynamically configurable fiber optic networks and DLP's (Digital Light Processors). In addition to the wide range of products made possible by silicon's mechanical properties silicon is also widely available; in fact silicon is the second most abundant element in the earth's crust [6]. Modern ingot's of silicon are some of the purest solids in existence, typically having fewer then 150 non SI parts per trillion [9]. The ability to chemically purify Si to this level and grow large crystals efficiently allows for fewer wafer defects, increasing device yield and performance.

1.5 Silicon as a micro- and nano-photonics platform

Micro and nano-photonics have benefited greatly from advances in process technology and the better understanding of materials such as silicon. Because the microfabrication infrastructure is already in place, implementation of such photonic devices requires only slight modification of existing process methodology for it to yield many of the same advantages. There are two major aspects of IC technology that have made micro and nano-optics possible. The first is the ability to accurately etch anisotropically, structures with nanometer dimensions. This provides the basis for fabrication of the single mode ridge waveguide and slab waveguide structures. The ability to define the location of these features through lithography makes alignment of waveguides with other optical devices

on the substrate possible [3]. In the world of discreet optical components this alignment process is one of the most costly parts of optical systems. The second aspect of IC technology that has made integrated optics possible is the development of the SOI substrate, particularly where a silicon dioxide dielectric layer is used. These SOI substrates provide several advantages in micro-optical systems, primarily as a result of the large index contrast between Si (n=3.45) and SiO_2 (n=1.46) [10]. In these substrates the core of the waveguide is fabricated out of the thin silicon top layer, and the underlying oxide is used as a cladding. This configuration provides an index difference of more then two to one in all directions for optical confinement (where air is the upper cladding) [11]. These optical properties of silicon and its native oxide allow for light to be confined at the material interface by total internal reflection (TIR). TIR occurs when the incident light at the interface is completely reflected; the angle from the normal of the surface at which this occurs, called the critical angle. It is derived from Snell's law to be a function of the ratio between the materials indicates. Similar to how electrons flow along the path of least resistance, photons tend to propagate in the region of highest index [4]. Because the light is so highly confined, single mode waveguides can have core cross-section with dimensions of only a few hundred nanometers and bending radii of a few micrometers with minimal losses. Because field leakage into the substrate and surrounding cladding is so low, these waveguides can be fabricated closer together without coupling occurring between them. The high index of silicon also allows devices to be shorter. SOI waveguides are so small they are commonly referred to as nano-photonic wires. In previous technologies where doping the silicon was used to locally

change the index by a small amount, confinement was relatively low, so dimensions had to be much larger, on the scale of micrometers and millimeters respectively. SOI technology is allowing for the miniaturization of these photonic structures on an order of ten to ten thousand leading to ultra dense integration [11]. The ability to integrate many optical components on the same substrate sets the foundation for the Photonic Integrated Circuit (PIC). Another advantage of silicon is that it is optically transparent at long haul communication wavelengths, between 1.3μm and 1.7μm [4]. This allows SOI waveguides as well as other nano-photonic devices fabricated on this platform to be easily integrated into existing silica based fiber optic networks.

The most attractive advantage of SOI as a photonics platform however is the ability it has to seamlessly merge with existing CMOS process technology. The potential for monolithic integration of optics and electronics onto a single substrate has the capability to revolutionize IC's as we know them [12]. This integration has the capacity to bring together the speed and bandwidth of optical systems with the complexity and well established engineering background of Integrated Circuits. The resulting superior hybrid systems have applications ranging from optical interconnects, to a wide range of networking devices such as multiplexers and de-multiplexers. Hybrid technologies may one day make optical computing, previously science fiction, a reality. The ability to connect peripherals optically avoids the latency issues experienced in electronics. No longer will the buss length be the bottle neck in computation systems. In fact this technology presents the possibility for a new form of distributed computing where

individual devices can plug into an optical buss and shared by many users, better optimizing the use of computation power. Current processors dissipate more then 50% of there power through the distribution of clock signals. Optical clock distribution on chip has the potential to considerable reduce power, and heat sinking requirements in electronic devices [13]. The advantages of such devices will have wide spread implications on the future of silicon based technology.

1.6 Problems Facing SOI Photonics

The development of micro and nano-PIC's is still in its infancy in many ways and therefore has several problems that must be addressed before the realization of a true hybrid, optics and electronics, technology can occur. Most of these problems result from a few undesirable properties of silicon that limit the degree of integration and level of performance of photonic components. These problems include the several poor optical properties of silicon, as well waveguide sensitivity to losses. Much research in the micro photonics area has provided the potential solutions to these problems which may mature as technology advices over the next several years. The primary problems being faced and there parental solutions will be discussed.

1.6.1 Elect-optic effect

One major disadvantage of silicon is that it doesn't exhibit the first order electro-optic effect or Pockel's effect as III-V semiconductors do. The electro optic effect states that a material's index of refraction, a critical optical property, is a function of the electric field

passing through it, and can be represented as a polynomial with various coefficients. This effect is the basis for most high speed modulators, and is a major link connecting optics and electronics. The first order Pockel's effect is typically dominant; however it only occurs in certain crystal lattice configurations were inversion asymmetry exists [14]. As silicon does not have this property, and higher order effects such as the Kerr effect that are lattice independent are so small, direct modulation by an electric field in silicon is difficult and many times requires the electric field to exceed the break down voltage of silicon.

Alternative methods for modulating the index in SOI waveguide devices are nonlinear carrier injection, also called the free-carrier dispersion effect, and the thermal optic effect. The injection of carriers (electrons or holes) into silicon can cause band shrinkage and band filling that change the index of the material [15]. The Thermal Optic Effect states that a materials index is dependent on its temperature. Although both of these effects are proven, they are considerably slower then the electro-optic effect, resulting in decreased modulations speed and thus reduced bandwidth in silicon based devices. The carrier injection method for modulation in silicon has a theoretical switching limit exceeding 1GHz; however practical devices are still limited to tens of megahertz [16]. These speeds are insufficient, particularly when many modern modulators fabricated in lithium niobate ($LiNbO_3$) are exceeding 40 Gbit/Sec. Much improvement in the use of silicon as a modulation medium is still required [17]. Advancements are continually being made in this area.

1.6.2 Infrared silicon photo detectors

Another disadvantage of silicon is caused by several undesirable characteristics of its band structure. The band structure of a material describes a series of "forbidden" and "allowed" electron energy states which determine many optical as well as electrical properties such as transmissivity and conductivity [18]. The transmission/absorption spectrum, particularly of crystals is dependent on what is called the energy bandgap, the energy difference between the top of the valence band (upper energy band) and the bottom of the conduction band (lower energy band) [19]. Absorption occurs where the energy of a photon is near that needed to excite an electron over the bandgap; the larger the bandgap the shorter the absorption wavelength and vice versa. The maximum absorption wavelength in covalently bonded materials can be approximated as Planks constant times the speed of light divided by the bandgap energy [20]. Silicon has a bandgap of approximately 1.14eV, corresponding to absorption in the range of 200nm to 1.1µm and transmition peeks at 1.3µm and 1.55µm [20]. These transmition peeks are advantageous for the integration of SOI devices with silica based fiber optics however, do not allow for the fabrication of photo detectors sensitive in this range. In order to detect light a photon must have sufficient energy to create free carriers by causing electrons to cross the bandgap [20]. Because silicon's bandgap is too large detectors in the 1.3 to 1.55 micron range can not be made in intrinsic relaxed silicon. The ability to create photo sensors is critical in converting optical information to an electrical form. In order to have

true integration of photonics and electronics on a SOI platform the development of such a sensor would be required.

Several methods, such as doping silicon with erbium (Er) a rare earth element commonly used as a dopent in fiber amplifiers, have been attempted in an effort to change the absorption spectrum. This method has had limited success due to constraints on the maximum allowable Er concentration in silicon [21]. One relatively new approach in solving this integration issue is manipulating the bandgap of the silicon device layer directly by inducing uniform biaxial tensile stress in the crystal lattice. By applying strain one can change the lattice parameter, the minimum length of periodicity in the crystal lattice, breaking the cubic symmetry. The lattes size has a considerable effect on the localized bandgap, and thus absorption spectrum [22]. As with most microfabrication processes strained silicon was first used in an effort to increase the speed of transistors. It was found that by inducing tensile or compressive stress either electron or hole mobility could be increased by as much as 80% and 37% respectively [23]. The increase in carrier mobility allows for a higher current drive at a given voltage. The reason for the improved mobility is that the modified lattice parameter reduces the probability of a carrier experiencing a collision, increasing the potential for ballistic transport. This increased mobility allowed for improved switching speeds.

Several methods have been developed for inducing strain in materials particularly silicon. The most common and well characterized method is the epitaxilal growth of silicon on an

alloy such as silicon germanium. Germanium is used as it is comparable with silicon processing technology. The silicon growth will occur pseudomorphically, meaning it will line up with the substrate lattice [23]. Because germanium has a slightly larger lattice parameter by approximately 4.17%, the growing silicon will be stretched [22]. The several hundred thousand pounds per square inch of induced strain stretches the silicon lattice by as much as 1.5% in the x-y plane and compresses it in the z direction. This change in lattice parameter provides a sufficient decrease in the bandgap to detect wavelengths as high as 1.5 microns. With only slight modification to a well characterized SOI wafer fabrication processes, such as SmartCut, Strained Silicon on Insulator (SSOI) wafers can be manufactured. The process is done by creating a layer of strained silicon then etching away the substrate used to strain the lattice. The silicon remains strained and can Unibonded to another wafer to create the SOI sandwich [24]. One major issue concerned with this processes of straining silicon is the formation of dislocations between the silicon and alloy substrate. If too many of these dislocations occur the silicon will relax back to an unstrained state. It is also possible for threaded dislocations to propagate to the surface affecting the device layer. These imperfections can severely impact electrical as well as optical performance by increasing scattering. The number of dislocations is a function of the silicon thickness grown and the temperature at which the growth takes place. At low temperatures thicknesses of 700Å can be obtained where at higher temperatures the thickness must be decreased considerably [22]. Once a strained layer is formed thermal budget is critical as the strain can be lost at high temperatures. Another issue is the diffusion of germanium, although the method is not well understood

it is possible for the germanium to diffuse up into the strained silicon region. Diffusion of germanium can also cause scattering and other undesirable effects. One way to avoid this is to strain silicon with one of several other methods that do not require the use of germanium. In IC processing Shallow Trench Isolation (STI) has been used near the channel to induce compressive or tensile stresses depending on what the trench is filled with [22]. Various high stress nitrides and thin film have been used to strain the maternal beneath them. Finally mechanical strain has been attempted, in which a wafer is thinned then physically flexed. Strained Silcon, as well as Si/SiGe superlattices, and Ge island structures have been used to realize near infrared photo detectors on a silicon substrate [4]. These detectors have been shown to have speeds greater then 2 GHz, good responsivity (0.75A/W), and low operational voltages (less then 1V) [4]. Despite the advances made in this technology and methods for straining silicon much development is required before a industry quality infrared SOI photo sensor for use in PIC can be realized.

1.6.3 Silicon light source

Another disadvantage of silicon, that originates from the structure of its bandgap, is the materials inability to efficiently produce light (photons) through inner-band transitions. The reason for this is that silicon is characterized by the properties of an indirect bandgap material. In an indirect bandgap, semiconductor electrons in the minima of the conduction band have a different momentum then holes in the maximum of the valence band [25]. As a result of the offset in k space between these particles, an electron must

first loose momentum in the form of a phonon (lattes vibration) before it can recombine with a hole [26]. In this type of band to band transition momentum is not conserved making the probability of radiative recombination extremely low. The minority carrier lifetime of these transitions is long, with quantum efficiencies around 0.02% for silicon alloys such as silicon carbide [26]. This low quantum efficiency of the silicon crystal structure makes light amplification impossible. The indirect bandgap structure of silicon also has an affect on the absorption spectrum; this is why silicon absorbs light at energies considerably larger then its bandgap. Silicon absorbs radiation by a method known as two photon absorption (TPA), in which two light quanta are simultaneous absorbed [27]. In direct bandgap materials where the k vector of the electron and hole are much closer, momentum can be conserved during recombination [28]. These types of transitions have a short lifetime and high probability of emitting a photon. Direct bandgap materials such as Germanium Nitride have quantum efficiencies as high as 12% [26]. Despite the many advantages of Germanium and other III-V semiconductor as optical materials they are not typically used as bulk substrates in high yield manufacturing because of their poorly characterized process technology, and limited availability.

Because III-V semiconductors are not viable for fabricating cost effective devices, the need to develop a high efficiency coherent light source on silicon is fundamental to the realization of PIC's. The fabrication of such a device would eliminate the need for costly external sources and the highly sensitive coupling methods required to get light into a nanometer sized waveguide device. An efficient silicon laser is considered by many to be

one of the last major barriers physically limiting silicon photonics as a viable technology. Several potential methods exist for generating or amplifying light in silicon, although none have yet been implemented with sufficient performances for practical application.

The first of such methods recently demonstrated by Intel is a silicon laser based on Stimulated Raman scattering (SRS) [29]. The Raman Effect describes the optical behavior that results from the inelastic collision a photon has when it impacts an atom or molecule. The theory states that a photon can impart energy upon colliding with a material in the form of a molecular vibration (phonon). After the collision the scattered photon has a lower energy resulting in an emission line at a longer wavelength. The method of Raman scattering is closely related to TPA in that it is a two photon interaction, upon the absorption of one photon the simultaneous emission of another occurs [27]. Given the correct material, and sufficient propagation distance it is possible for existing vibrations in the lattice to amplify the energy of this secondary wavelength. The first Raman amplifiers used kilometer long stretches of glass fiber as the amplifying medium [29]. Silicon has the advantage of having a Raman Effect that is more then ten thousand times stronger then that of a silica fiber, allowing for the same amplification to occur in silicon devices only centimeters in length. The disadvantage of this type of laser is that it requires a high power external pump source in order to create a sufficient number of scattered photons, making amplification extremely inefficient. The high intensity pump also increases the number of carriers, through the photo electric effect. These carriers can cause scattering that increases the losses in the waveguide. Intel's way

of minimizing these losses is to place P and N doped regions on either side of the waveguide that are biased in such a way to sweep electrons out of the propagation region [29]. Although the Raman laser is possible it is not practical for PIC. An ideal silicon laser would relay on an electrical pumping mechanism. Several areas of research hold potential for achieving efficient electro luminescence in silicon. The use of periodic structures in silicon such as nano-clusters (pillers and holes), nano-wires, and quantum dots have been used to enhance quantum-like effects that alter the band properties of silicon to the point where raditive emissions can occur [16]. Silicon LED's (Light Emitting Diodes) that emit in the near infrared spectrum have been achieved by doping silicon with Erbium (Er), to overcome the indirect bandgap effects in silicon. It is possible to use such an LED as a pump source to achieve lazing at 1.54μm in cavities formed by Distributed Bragg Reflectors (DBR) and a Fabry Perot Etalon [30]. All these methods are still in there preliminary stages of development, yielding low efficiencies, and in many cases requiring super cooling to further lower the bandgap before light emission can occur [31]. For these reasons considerable development is required, particularly in the fabrication of nano-photonic band gap structures (PBG) before a practical silicon light source is developed.

1.6.4 Losses in SOI devices

One factor that has a considerable impact on the performance of photonic components, are the losses that occur during the propagation of light. Devises that rely on Total Internal Reflection (TIR) as a method of optical confinement, such as waveguides, are

particularly vulnerable because of non-idealities in their structure. Silicon waveguides have several loss mechanisms that contribute to this problem. These methods include absorption, scattering from volumetric refractive index inhomogeneity, coupling of guided modes to substrate modes, and interface induced scattering [32]. Additional losses not associated with propagation occur during the coupling of light in and out of the device. Other losses solely caused by waveguide structure, such as bends, can occur as well however this section will deal primarily with losses attributed to material and fabrication non idealities. Waveguide losses are typically quantified in terms of dB/cm, and range from 0.1-0.5 dB/cm for straight waveguides. The boundary for acceptable losses is on the order of 1dB/cm, losses that exceed this result in poor signal to noise ratio when received by a detector [24].

Absorption losses can be classified as inter-band absorption or free carrier absorption. Inter-band absorption is caused when a photon has energy greater then the material band gap transferring its energy to the excitation of an electron. The band edge for silicon is approximately 1.1μm. Inter-band absorption decreases considerably when the wavelength is greater then the band edge. At 1.15μm losses from this type of absorption are around 2.87 dB/cm dropping substantially to 0.0004 dB/cm at a wavelength of 1.523μm [32]. Free carrier absorption is not as insignificant, and can be described by the Drude-Lorenz equation [24]. For carrier concentrations on the order of 10^{18} cm^{-3} in silicon losses of 10.86 dB/cm are reported [24]. Losses due to volume inhomogeneity scattering are caused by voids, impurities or defects in silicon's crystal lattes. These losses are closely

tied to the quality of the material used, and manufacturing process steps such as diffusion, or implantation of dopents, as well various thermal processes that alter the uniformity of the crystal. For SOI wafers it is believed that roughness of the silicon-oxide interface is also a cause of defects in the device layer that can contribute to these losses. If the process steps are carefully chosen and a highly uniform SOI manufacturing process such as SIMOX is used, this loss mechanism is minimal. Losses associated with the coupling of modes into the substrate and radiated modes are primarily dependent on the thickness of the buried oxide, and the intensity of evanescent waves. These losses are minimized if the oxide thickness is greater then 0.4 microns, the waveguide is designed to be single mode (smaller evanescent waves) and the core width larger then 2 μm (lower confinement) [32].

The dominant loss mechanism in waveguides however is surface induced scattering. Unlike other disadvantages of silicon photonics that are based on physical limitations of the material, surface scattering is caused by the highly random phenomena of nanometer sized interface roughness induced during manufacturing. Although all four surfaces on a waveguide have a certain degree of imperfection, sidewalls, because of there crystal plane and the manufacturing steps they undergo, such as plasma etch or reactive ion etch (REI), are the cause of most of these scattering losses. Sidewall roughness can be mathematically modeled as random variations in waveguide width. These variations cause changes in the localized refractive index along the waveguide. The modulation of effective-index at different points within the waveguide act as a pseudograting, which

when excited couples light into the adjacent cladding [33]. A conceptual understanding of why losses occur on a rough core-cladding interface can be best understood through the ray model of a guided mode. When a light ray strikes a rough surface, there is a potential that the reflected ray has an angle greater then the critical angle, meaning TIR will not occur and a portion of the light will be transmitted into the cladding and lost. Theoretical work in characterizing these losses was done by Marcuse [34], later an analytical approach was derived by Payne and Lancey that accurately characterized these losses, and also agreed with experimental loss calculations [35]. These early works determined that sidewall losses are dependent on several factors including the periodicity of the roughness (autocorrelation length), depth of the roughness, index contrast between guiding medium and cladding, as well as waveguide structure such as its width and curvature [36]. It was found that losses increase as a square of the roughness amplitude. This is expected as taller roughness corresponds to larger fluctuations in the interference region and in turn more severe scattering [37]. The autocorrelation length will have a maximum impact on losses, as it approaches one wavelength, similar to the behavior of grating structures [36]. Index difference between the core and cladding has a direct effect on interface reflectivity. Although this reflectivity is ideal for high confinement it causes increased losses from interface scattering proportional to $(\Delta n)^3$. High index contrast is also a major factor attributed to difficulties in fabricating efficient waveguide grating devices on SOI. Filters based on such structures tend to have high loss and suffer from strong grating index modulation that limits spectral width [38]. Input and output coupling losses are caused by the highly reflective facets found on SOI waveguides. Waveguide

dimensions are also a considerable factor in losses caused by sidewall roughness. As the width of the core decreases the losses increase exponentially due to the increased interaction between the waveguideing mode and sidewall imperfections [39]. Calculated losses and measured results show that waveguides with widths of 2μm have losses on the order of 1dB/cm however a more highly confined mode with a waveguide width of 0.5 μm experiences losses of more then 30dB/cm. Once waveguides exceed 4μm in dimension losses attributed to sidewall roughness are negligible [36]. Losses in curved waveguides, typically 1dB per ninety degree bend, are also attributed primarily to interface roughness [39]. The losses in bends will also occur in smooth waveguides independent of material impurities and non-idealities. The reason these losses can occur in even a perfect waveguide is due to the phase difference that arises between the field in the core and cladding around a bend. A detailed description of the bent waveguide structure and the losses they incur will be described in the theory section of this thesis.

Several manufacturing processes have been proven to minimize the amplitude of waveguide roughness, and thus losses related to interface scattering. The most common smoothing technique is achieved by oxidizing the silicon surface, and then etching off the oxidized region [40]. The method by which oxidation smoothing occurs can be described by the Gibbs-Thompson Relation, which states that the chemical potential of a surface is related to its curvature [37]. Surfaces that have positive curvature are more reactive, causing differential reaction rates on rough surfaces that favor peeks. When oxidation occurs on a rough surface peeks will oxidize more quickly then troughs, and when etched

the over all amplitude of roughness will be lowered. Several oxidation methods have been used to accomplish this, however it has been shown that wet chemically grown oxides are less evasive then gas phase oxides that require a large thermal budget and tend to distort the cross section of the waveguide [37]. These changes in cross-sectional dimension can have severe effects on the waveguide's optical properties. The reason for the relatively large change (10nm) in waveguide dimension associated with gas phase oxidation smoothing is related the type and controllability of the reaction that occurs. The formation of SiO2 takes place in either a reaction or diffusion limited regime. Reaction limited oxides consist of the first 20nm of growth and are governed by surface reaction potential. Oxides that are grown thicker then this are considered diffusion limited, and are less efficient, consuming more of the substrate for an equivalent reduction in roughness amplitude. Wet Chemically grown oxides are preferred as they can be controlled more accurately allowing for smoothing to be confined to the reaction limited condition. Methods such as RCA clean have been implemented repeatedly grow and etch such oxides to reducing sidewall losses from 9.2dB/cm to 1.9dB/cm [37]. Other smoothing methods such as CMP (Chemical Mechanical Planarization) use fine grit slurry to polish the top surface of the waveguide. Because the top of the waveguide is not one of the primary loss surfaces this method is not as commonly used as a smoothing mechanism.

1.7 Summary

Despite the problems that micro-optics has encountered and continues to encounter during its development, the technology shows considerable promise as the ability to

fabricate quantum structures improves. The most attractive aspect of micro-optics on the SOI platform is its capacity to be mass fabricated in the same way microprocessors have been. As the technology is compatible with CMOS processing the design of viable micro-optic systems that integrate well with microelectronics are possible. Many passive structures in micro-optics, which rely on TIR, have been successfully fabricated on the SOI platform. These devices include a wide range of splitters, filters, and wavelength multiplexing structures. Structures such as Arrayed Waveguide Grating (AWG), a Wave Division Multiplexing (WDM) device, are already being used in many telecommunication systems. As research in the area continues the performance and viability of micro-optics is consistently improving.

1.8 Thesis Research

The goal of this thesis will be to design, model, fabricate, and test several of these passive micro-optic structures including y-splitters, directional couplers, wavelength splitters, and multimode interference splitters, to prove their viability at RIT. Each device will be based on the single mode rib waveguide structure, designed on an SOI substrate. Prior to the implementation of these devices the mathematical theory describing their operation will be presented along with a comparison of the several analytic methods that are classically used in micro-optics.

The design and simulation of these structures will be accomplished with the use of the OptiWave software package. For each structure a specific design process will be

formulated based on mathematical theory. Devices which rely on coupling will make use of an iterative BPM optimization method written in the OptiWave scripting language. A least squared regression is used to efficiently map simulation data to theory, dramatically reducing the required computation time needed in the design process. Using this optimization method the coupling between adjacent waveguides is characterized for varying waveguide separation and wavelength. A detailed comparison of losses incurred between each class of splitter as well as for changing dimensions and shape for a given splitter will be evaluated. It is found that directional couplers have the lowest losses (≈2%), however are least tolerant of fabrication variation, where as the y-branch has the highest losses (≈10%) and is nearly invariant to deviations in fabrication.

Once an optimized structure for each of these devices is determined, a microfabrication process is developed and refined. Issues regarding the process development, device tolerance, and loss mechanisms are considered and a physical structure realized. Preliminary testing is accomplished with the design of an alignment translation stage, microscope and camera mount. The test setup, along with several input coupling techniques, are used to evaluate device operation and obtain pictures showing the qualitative operation of several structures. Due to poor facet quality and alignment ability, precise loss measurements on the fabricated devices were unable to be obtained however, the improvements required to fix these problems are presented for future work.

Chapter 2: Theoretical Foundation

2.1 The Electromagnetic Wave

The Near Infrared (NI) frequencies used in telecommunications and micro-optics are a subset of a large class electromagnetic radiation that range from extremely low frequencies (ELF) used in underwater communications, to gamma rays produced in subatomic processes such as radioactive decay [41]. Regardless of the energy or frequency all electromagnetic waves have the same fundamental properties, described by Maxwell's equations. These four differential Equations (1)-(4) relate Electric field (E),

Magnetic field (H), charge density (ρ), and current density (J) to each other. For the analysis of waveguide devices ρ and J are considered to be zero [13].

$$\vec{\nabla} \times \varepsilon \vec{E} = \rho, \qquad \textbf{(1)}$$

$$\vec{\nabla} \times \vec{E} = -\frac{d}{dt} \mu \vec{H}, \qquad \textbf{(2)}$$

$$\vec{\nabla} \times \vec{H} = -\frac{d}{dt} \varepsilon \vec{H} + \vec{J}, \qquad \textbf{(3)}$$

and

$$\vec{\nabla} \times \mu \vec{E} = 0. \qquad \textbf{(4)}$$

All electromagnetic waves travel at the speed of light (c) in a vacuum, and consist of an electric component that as it propagates induces an orthogonal magnetic component and vice versa [42]. Micro-optics is concerned with the propagation of such electromagnetic waves through various structures. An important property of an EM wave is the orientation of its field components, referred to as the polarization of the wave. All EM waves can be represented by a superposition of various polarizations. Although several polarizations exist, the only ones of interest are those that lead to the flow of real power [43]. The most common of such modes encountered are the Transverse Electric (TE) and Transverse Magnetic (TM) fields which refer to the condition when either the electric or magnetic field component of the wave is perpendicular to the plane of incidence. The TE wave has e_z=0 and the TM wave h_z=0 where z is the direction of propagation. Although

TE and TM modes are sufficient for a simplistic understanding and will be the main focus of this paper, there also exists hybrid modes represented as HE ($|h_z|>>|e_z|>0$) and EH ($|e_z|>>|h_z|>0$) [43]. The flow of electromagnetic power in a given polarization of a wave is represented as the vector product of the electric and magnetic components, or pointing vector. Another common representation for the pointing vector is given in Equation 5 where ε_m is the permittivity of the medium and μ_m is the permeability of the medium, and E is the electric field. The intensity of light (I) is defined as the magnitude of the time-averaged pointing vector [4].

$$S = E \times H = \sqrt{\frac{\varepsilon_m}{\mu_m}} E^2 . \qquad \textbf{(5)}$$

2.2 The Optical Waveguide

A waveguide is a physical structure that has the ability to direct and confine energy in the electromagnetic spectrum [44]. Waveguides that operate in the optical portion of the spectrum include fiber optics used in telecommunication, as well as micro-fabricated ridge or rectangular waveguides on thin films such as SOI. Both of these waveguide platforms rely on a dielectric guiding medium called the core of the waveguide, surrounded by a lower index material called the cladding. The propagation of an electric field through such as structure can be intuitively understood by the use of the ray optics model described by Snell's Law in Equation (6).

$$n_1 \sin(\theta_1) = n_2 \sin(\theta_2). \qquad \textbf{(6)}$$

Snell's Law relates the incident angle θ_1 of light in a medium with index n_1, impinging on the interface of a material with index n_2, to the resulting angle θ_2 that the light is refracted to when it enters the new medium. A diagram of the physical representation of these variables is given in Figure 1 [43] [24].

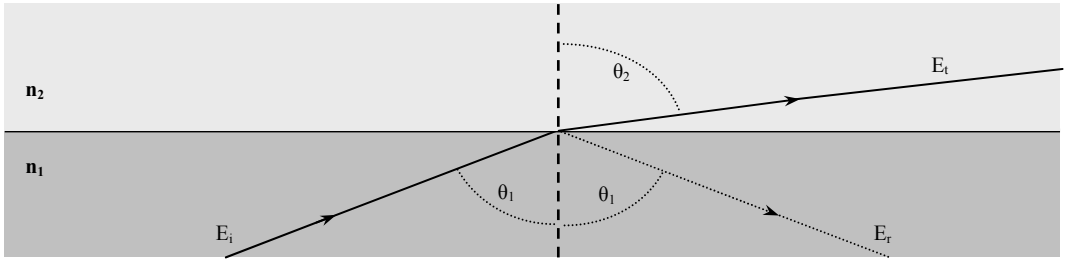

Figure 1. Refraction of light passing between two mediums

If n_1, n_2, and θ_1, are correctly chosen it is possible for θ_2 to become 90°, a condition termed Total Internal Reflection, where the incident light impinging on the interface is reflected back into the starting medium. The point at which angle θ_1 allows for this condition is called the critical angle and is calculated to be $\theta_c = \arcsin(n_2 / n_1)$ [24]. A waveguiding structure works in such a way that each interface reflection occurs at an angle larger then θ_c as a result the light ray will theoretically continue in the core region indefinitely. The simplest structure that can be understood by this method is the slab waveguide. This 2D waveguide consists of a high index material sandwiched between

two low index materials. If light is injected into the edge of this structure within the acceptance angle of the waveguide, it will be confined to the high index region.

Another way of understanding the concept of TIR and the behavior of a reflected wave is through Fresnel's Equations describing the reflection coefficient. The reflection coefficient is a multiplier that relates the amplitude of the incident electric field on a dielectric interface to the amplitude of the reflected field. Fresnel's equation for this coefficient, expressed in terms of the same variables n_1, n_2, θ_1, and θ_2 used in Figure 1 are given for both TE and TM field polarizations in Equations (7) and (8) [24].

$$r_{TE} = \frac{n_1 \cos(\theta_1) - \sqrt{n_2{}^2 - n_1{}^2 \sin^2(\theta_1)}}{n_1 \cos(\theta_1) + \sqrt{n_2{}^2 - n_1{}^2 \sin^2(\theta_1)}}, \qquad \textbf{(7)}$$

and

$$r_{TM} = \frac{n_2{}^2 \cos(\theta_1) - n_1 \sqrt{n_2{}^2 - n_1{}^2 \sin^2(\theta_1)}}{n_2{}^2 \cos(\theta_1) + n_1 \sqrt{n_2{}^2 - n_1{}^2 \sin^2(\theta_1)}}. \qquad \textbf{(8)}$$

In these equations if the incident angle, θ_1, is smaller then θ_c the resulting reflection coefficient will be a real number less then 1, corresponding to a certain portion, T=1-r, of the incident light being transmitted. If this angle is larger then θ_c however then the result within the square root becomes negative, meaning the absolute value of the reflection coefficient is 1, implying that the entire wave is reflected. The complex portion of the

result corresponds to a phase shift in the incident wave, as it reflects off of interface [24]. These equations agree with Snell's law.

Another constraint on guiding an electromagnetic wave is that it cannot propagate at any angle less then θ_c but rather only discreet allowed angles [24]. Each of these discrete solutions is called a mode of propagation. A mode can be thought of as a standing wave perpendicular to the direction of propagation and a traveling wave parallel to the direction of propagation [13]. The concept of a mode comes from the fact that the wave vector has components both perpendicular and parallel to the waveguide. Each time the ray is reflected from the guiding interface the perpendicular component experiences a phase shift as described in Fresnel's Equations. The preservation of the wave across the waveguide can only occur when this phase shift is an integer multiple (m) of 2π. Each multiple, m, represents a guided mode [24]. For the most simplistic symmetric plainer waveguide case the modal condition for the TE mode is represented by the Eigenvalue Equation (9) and (10). The core index is given by n_1, the cladding index by n_2, free space wavelength by λ_o, and core height given by h. This equation can be solved for θ_1, the given propagation angle at a supported mode number m. The higher order the mode, the larger the propagation angle θ_1 will be until the critical angle is reached. A similar equation for the TM mode as well as an analysis of the asymmetric slab waveguide can be found in [24].

$$\tan\left[\frac{k_o n_1 h\cos(\theta_1) - m\pi}{2}\right] = \frac{\sqrt{\sin^2(\theta_1) - (n_2/n_1)^2}}{\cos(\theta_1)}, \qquad \textbf{(9)}$$

and

$$k_o = \frac{2\pi}{\lambda_o}. \qquad \textbf{(10)}$$

There are a finite number of modes that can propagate in a given waveguide, which is determined by the dimensions of the waveguide, as well as the wavelength and polarization of light. Every waveguide transmitting at wavelengths above a certain cut-off frequency can support what is called the fundamental mode, which caries the most energy and is the case where the integer multiple of standing waves is one [46]. In practice waveguides are typically excited by a field with a Gaussian distribution. These distributions as well as any other non-modal field can be represented by a continuum of radiated and guided modes, all of which are orthogonal to each other [46]. Radiated modes will be lost from the waveguide after some finite propagation distance, only the guided modes will theoretically travel down the waveguide indefinitely without loss [4]. Supported modes are designated by their polarization followed by a subscript indicating the number of minima in each dimension, x and y. For example, the fundamental TE mode of a 2D rectangular waveguide would be written TE_{00} indicating a single maxima. It can also be helpful to describe a mode in terms of an effective-index of refraction. The effective-index is an equivalent index (between that of the cladding and core) that would allow for the wave vector to propagate straight down the waveguide without zigzagging back and forth [24]. The higher order the mode of propagation, corresponding to a larger

angle of incidence at the core cladding interface, the closer the effective-index will be to that of the cladding and vice versa. It will be seen that this representation of a waveguide can be used to greatly simplify the problem of determining the field distribution in a waveguide.

Although the ray model description of a wave propagating down a waveguide works well for basic understanding, it lacks the ability to precisely describe the relationship between the electric and magnetic filed components. In order to visualize the exact modal distribution of a field, and explain processes such as optical coupling Maxwell's Equations must be used [24]. The wave equation, an important result derived from Maxwell's Equations are used in solving for these modal distributions. The wave equation, Equation (11), is given where ψ represents either the electric or magnetic field, and ∇^2 is the Laplacian operator (12). Another common form of the wave equation is to represent the permittivity and permeability in terms of wave velocity (υ).

$$\nabla^2\psi = \mu_m\varepsilon_m\frac{\partial^2\psi}{\partial t^2} = \frac{1}{\upsilon^2}\frac{\partial^2\psi}{\partial t^2}, \qquad \textbf{(11)}$$

and

$$\nabla^2 = \frac{\partial^2}{\partial x^2} + \frac{\partial^2}{\partial y^2} + \frac{\partial^2}{\partial z^2}. \qquad \textbf{(12)}$$

The exact field distribution for the first four modes of a slab waveguide found by solving the 1D wave equation are given in Figure 2 [47].

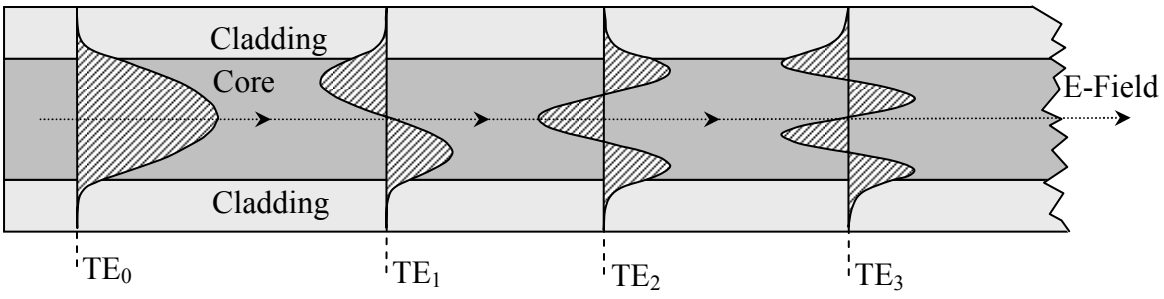

Figure 2. Modal distributions in a slab waveguide

The solution to the wave equation becomes increasingly complex for multidimensional, non-rectangular guiding structures. In fact the exact symbolic solution is impossible except for in the simplest waveguide geometries. In order to solve the ridge waveguide structure used in this thesis several approximate analytic and numeric methods must be employed. These methods will be applied through the use of the Optiwave waveguide simulation software package. The details behind these various methods will be described in a later section of this thesis. For further information on the symbolic solution to the wave equation, several texts [46] [24] [48], on electromagnetic waves should be referred to.

2.3 Single Mode Condition

The most fundamental passive structure in integrated optics is the waveguide. Almost all micro-optic devices from modulators, to directional slitters use waveguides in one way or another [49]. Insuring the single mode condition (SMC) of these structures provides many advantages in the behavior of the guided light as well as compatibility of the device with existing telecommunication systems. The fundamental mode of a waveguide, carries

the majority of optical power and is the most well confined field distribution. The high confinement of the fundamental mode corresponds to a small portion of the field existing outside of the core (low evanescent waves), minimizing losses from sidewall interference scattering. The SMC also reduces losses that occur when coupling light into single mode fiber commonly used in long haul data transmission [50]. For these reasons the majority of waveguide devices in this thesis will be designed to operate in the single mode region. In order to design such devices it is pertinent to understand what conditions constitute the single mode behavior.

The slab waveguide is highly restrictive in that only a small range of waveguide dimensions will allow for a single mode to exist. In a high confinement SOI structure the core must be less then 0.2 microns for the SMC to be met at a wavelength of 1.33 microns. As the dimensions of the core increase, or wavelength decreases the number of modes increase considerably. A SOI waveguide with a core width of five microns has over twenty four modes at the same wavelength [24]. The small dimensions of an SOI single mode slab waveguide and their high sensitivity to surface imperfections at that size, not only make them difficult to fabricate without electron beam lithography or other special techniques but are also difficult to effectively couple light into. A structure called the ridge waveguide has the ability to support single mode propagation over a much larger range of dimensions (on the order of several microns) eliminating many of the fabrication constraints that make achieving the SMC in planer structures so difficult [51]. A cross-section of the ridge waveguide is depicted in Figure 3 [52].

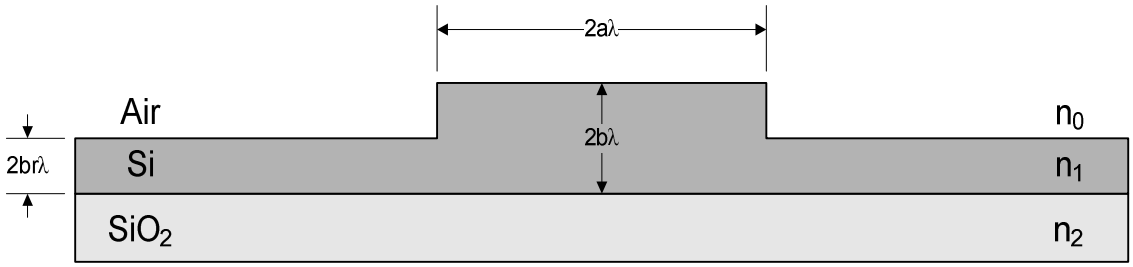

Figure 3. Ridge waveguide structure in silicon on insulator

The SMC is possible in large ridge structures as higher order modes radiate out of the ridge into the underlying silicon region [50]. The analysis of such structures has been accomplished through several methods including FD-BPM and EIM however Soref, Schmidtchen, and Petermann were the first to use a mode matching technique to describe the approximate single mode condition in a simple expression [52]. The equation derived by Soref et al. for the SMC is given in Equation (13) in terms of the variables defined in Figure 3. Variables a and b represent the rib width and height factors respectively, λ the free space wavelength and r the ratio of the thin silicon slab layer to the total rib height, 2bλ. The variable q is defined in Equation (14) in terms of $\gamma_0=\gamma_2=1$ for the HE polarization and $\gamma_0=(n_0/n_1)^2$, $\gamma_2=(n_2/n_1)^2$ for the EH polarization. The indices of each layer are represented by n_0, n_1, and n_2 respectively [52].

$$\frac{a}{b} \le \left(\frac{q+4\pi b}{4\pi b}\right) \frac{1+0.3\sqrt{\left(\frac{q+4\pi b}{q+4\pi r b}\right)^2 - 1}}{\sqrt{\left(\frac{q+4\pi b}{q+4\pi r b}\right)^2 - 1}}, \qquad \textbf{(13)}$$

and

$$q = \frac{\gamma_0}{\sqrt{n_1^2 - n_0^2}} + \frac{\gamma_2}{\sqrt{n_1^2 - n_2^2}}. \qquad \textbf{(14)}$$

Two assumptions are made in the derivation of this equation which must be satisfied in order for the results to be considered valid. The first, is that the cross-sectional area of the waveguide is relatively large where $2b\sqrt{n_1^2 - n_2^2} \geq 1$. The second assumption is that the waveguide ridge is shallow, meaning that r is between 0.5 and 1. The shallow ridge condition ensures that higher order modes in the vertical direction are coupled into the fundamental mode of the slab section [52]. Although the SMC can be met for deep waveguides where r is less then 0.5, the problem becomes increasingly complex, and cannot be described by Equation (13) [52]. Figure 4 depicts a plot of the critical a/b ratio verses ridge height factor (b), for an SOI rib waveguide [52]. Both the HE and EH polarizations are shown, for r values of 0.6 and 0.8. The Mathcad code used produce this diagram is given in Appendix A.

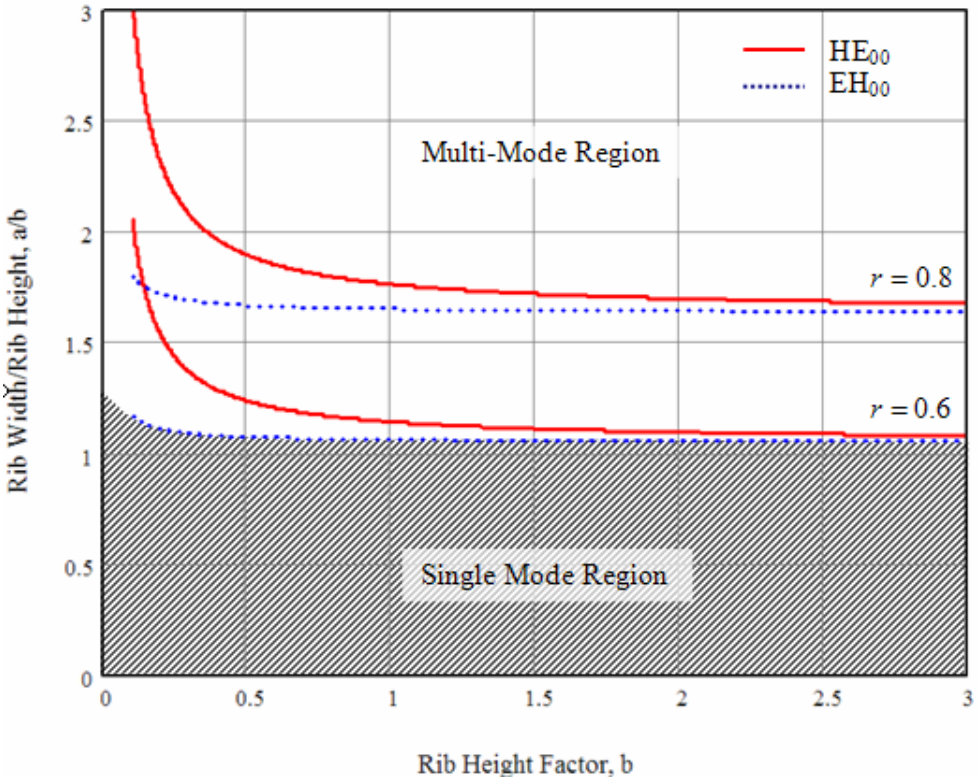

Figure 4. Critical a/b ratio vs. ridge height factor, b for SOI rib waveguide

The region beneath each of these curves represents the combinations of waveguide dimensions that will ensure single mode operation at that given polarization and r factor. It can be seen that for large ridge heights the critical width-height ratio approaches an asymptote and r become the dominant factor that determines which width-height ratios will support a single mode.

2.4 The Waveguide Bend

The waveguide bend is another fundamental structure important to the design of many micro-optic devices. Unlike the straight waveguide that can only propagate a signal in one dimension the bend structure provides the ability to redirect a signal from one point

to another in two dimensions [13]. The bend will be crucial to the operation of various coupling devices designed and implemented in this thesis as these structures need to have waveguides that separate away from each other after a finite distance. Despite the obvious uses and advantages of this structure its major drawbacks are the losses that it can introduce to a propagating signal. These losses arise from the outer edge of the bending waveguide having a larger diameter. Because the distance that light must transverse is a function of location within the medium, the field must propagate faster in the outer cladding then the inner cladding in order to maintain a constant phase relationship across the mode [24]. A situation will eventually occur where the evanescent wave in the outer cladding of the bend would need to exceed the velocity of unguided light in that medium [13]. As it is impossible for this condition to hold true the light will be lost in the form of a radiated mode. A bend can be mathematically described by a straight waveguide with a modified index profile. A larger bending radius implies an increase in the effective-index of the outer cladding. As the bend increases so does the index slope, resulting in more light coupled out of the waveguide [13]. The method of describing a bend in terms of effective indices is referred to as conformal mapping and is easily applied in the Beam Propagation Method (BPM) when simulating such waveguides. An approximation to the losses incurred as light propagates though a waveguide of constant bending radius is given by the equation for the loss coefficient of a bend, $\alpha_{bend} = C_1 e^{-C_2 R}$. In this equation C_1, C_2 are constants define in Equations (15) and (16), and R is the radius of the bend [24].

$$C_1 = \frac{\lambda_0 \cos^2\left(k_{xg}\frac{w}{2}\right)e^{k_{xs}w}}{w^2 k_{xs} n_{effp}\left[\frac{w}{2} + \frac{1}{2k_{xg}}\sin\left(wk_{xg}\right) + \frac{1}{k_{xs}}\cos^2\left(k_{xg}\frac{w}{2}\right)\right]}, \qquad \textbf{(15)}$$

and

$$C_2 = 2k_{xs}\left(\frac{\lambda_0\beta}{2\pi n_{effp}} - 1\right). \qquad \textbf{(16)}$$

In these constants w represents the width of the waveguide (2aλ), β is the propagation constant in the z direction defined as the ratio of angular frequency to phase velocity (w/v_p), k_{xg} is the propagation constant in the x direction, k_{xs} is the decay constant in the x direction, n_{effp} is the effective-index outside the rib (cladding index), and λ_0 is the free space wavelength [24]. From this representation of the loss coefficient it can be seen that losses are directly related to the radius of the curve, smaller curvatures result in exponentially higher losses. Losses are also related to how well confined the mode is, lower evanescent waves result in lower losses in waveguide bends. This dependence on confinement makes the SOI platform desirable due to its high index contrast. However this also means that the rib waveguide is more susceptible to bending losses then a conventional strip or buried waveguide structure because of its lower confinement. Losses can be reduced in rib structures by making the rib etch depth parameter r large [4]. It is also important to note that losses in bends are polarization dependent. The TM polarization will experience more then three times the losses incurred by the TE mode. This discrimination between modes is associated with the higher interaction. The TM

mode has with the sidewalls, increasing the evanescent waves in the cladding. Over all losses from waveguide bends tend to be a few dB per 90 degree of turn depending on the geometry and index contrast of the structure [24] [13] [4]. For a given process losses due to waveguide bends can be most easily reduced by designing structures with sufficiently large bending radii.

2.5 The Coupled-Mode Analysis

When light propagates down a waveguide structure, a small potion of the mode referred to as the evanescent field propagates in the cladding region. The intensity of the evanescent field decays exponentially with increasing distance into cladding, to a point quantified by the penetration depth [24]. If two waveguides that independently support a field distribution are brought close enough to each other so their evanescent fields overlap, the waveguides are referred to as coupled and energy is able to transfer between them [46]. The basic coupling structure of two parallel waveguides is referred to as the waveguide to waveguide coupler or evanescent coupler and forms the foundation for a wide range of micro-optic devices including modulators, Mech-Zender interferometers, wavelength splitters, directional splitters, and ring resonators [24]. A diagram of a rib waveguide to waveguide coupler is given in Figure 5, where *s* is the waveguide separation; *w* is the waveguide width, and L the coupling length [24].

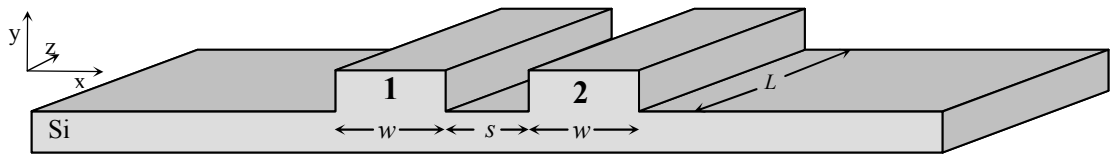

Figure 5. 3D diagram of rib waveguide to waveguide coupler

The behavior of the energy transfer that occurs between these two waveguides is fundamentally described by Maxwell's equations however a simplified understanding can be obtained from the coupled-mode Equations (17) and (18).

$$dA_1/dz = -i\beta A_1(z) - iKA_2(z), \quad \textbf{(17)}$$

and

$$dA_2/dz = -i\beta A_2(z) - iKA_1(z). \quad \textbf{(18)}$$

These differential equations describe the inter-relationship of the field amplitudes (A_1 and A_2) in each waveguide as a function of the propagation distance z where β is the propagation constant of each waveguide and K is a coupling coefficient. The coupling coefficient is a parameter used to quantify the degree of overlap that occurs between the evanescent fields of each waveguide [24]. The larger the coupling coefficient the more quickly energy will transfer between the waveguides. The general form of this parameter is given in Equation (19) in terms of k_{xc}, the x directed propagation constant in the core, k_{xs}, x directed decay constant, s, the separation of the waveguides, and β [24].

$$K = \frac{2k_{xc}^{\ 2}k_{xs}e^{-k_{xs}s}}{\beta w(k_{xs}^{\ 2} + k_{xc}^{\ 2})}. \quad \textbf{(19)}$$

From Equation (19) it can be seen that the coupling coefficient is highly dependent on several factors such as modal confinement, as given by dependence on the propagation constant, as well as the proximity of the waveguides. These factors are critical to the degree of coupling as the amplitude of the evanescent field is directly related to both. Highly confined modes in waveguides that are far apart correspond to low coupling, and vice versa. It is also important to note that K is scaled by the inverse of the propagation constant; implying that coupling is also wavelength dependent [46]. This property of the coupling is what is utilized to design wavelength selective device such as wavelength splitters. Due to the complexity and large dependence on geometry the exact coupling coefficient can only be obtained for a handful of simple waveguides. Numerical methods such as BPM and FDTD are commonly used for more complex structures such as rib and curved waveguides.

The solution to the coupled-mode differential Equation (17) and (18) can be solved for an important case where there is an optical input to only one of the waveguides, corresponding to the initial condition where $A_1(0)=1$ and $A_2(0)=0$. Using these values and solving the differential Equation (17) and (18) for the amplitude in each waveguide yields the result in Equations (20) and (21) which correspond to the field amplitude in each waveguide [46].

$$A_1(z) = \cos(Kz)e^{i\beta z}, \qquad \textbf{(20)}$$

and

$$A_2(z) = -i\sin(Kz)e^{i\beta z}. \qquad \textbf{(21)}$$

It can be seen from these solutions that a propagating mode will transfer back and forth between the two waveguides in a periodic fashion, where the coupling coefficient K has a direct impact on the frequency of the energy transfer. It is also apparent that a phase change will occur each time the mode transfers between waveguides as denoted by the complex component of the field amplitude in waveguide 2 [46]. These devices are commonly used to alter the phase of an optical signal for this reason.

By Defining the complex propagation constant β in terms of its real component β_r and loss coefficient α_{loss} ($\beta = \beta_r - i\alpha_{loss}/2$), the amplitude from of the coupled field in Equations (20) and (21) can be represented in terms of power as given in Equations (22) and (23) [46].

$$P_1(z) = A_1 A_1^{*} = \cos^2(Kz)e^{-\alpha_{loss}z}, \qquad \textbf{(22)}$$

and

$$P_2(z) = A_2 A_2^{*} = \sin^2(Kz)e^{-\alpha_{loss}z}. \qquad \textbf{(23)}$$

With the understanding that these equations provide, it is possible to design a coupling structure that splits light into any desired ratio. A 50-50 splitter or 3dB splitter can be made by letting the length of the coupling region $L=m\pi/4K$, where m is an integer multiple [24].

2.6 Self-Imaging

Self-Imaging is a phenomena that arises in multimode waveguides where an "input field profile is replicated in signal or multiple images at periodic intervals along the propagation direction of the waveguide" [53], [54]. This imagining effect is caused by interference of the many modes supported by such a waveguide [55]. The output field profile at a given length can be approximated by the Equations (24) and (25) which represents accumulation of phase differences between the given modes [56].

$$(\beta_m - \beta_0)L = -\frac{\pi m(m+2)L}{3L_\pi}, \qquad \textit{(24)}$$

and

$$L_\pi = \frac{4nw^2}{3\lambda}. \qquad \textit{(25)}$$

In Equation (24) β_m represents the propagation constant of mode number m (0,1,2, ...), and L_π beat length between the first two modes (m=0, 1). Variables L, and w describe the width and length of the multimode waveguide, respectively, n is the effective-index of refraction of the waveguide and λ the excitation wavelength [56]. The L_π parameter in Equation (25) is what describes the periodic nature of the imaging effect. The diagram in Figure 6 shows the most general form of such multimode interference. An arbitrary input field is given at z=0, total constructive interference will occur at multiples of $6L_\pi$, to create a self image of the input [56]. At half this distance a mirroring of the input field

over the center of the waveguide region occurs as the odd and even modes are out of phase [56]. Further dividing of the input field occurs at fractions of this length. Due to the fact that all modes of this waveguide undergo the same phase change, the mirroring lengths are independent of the location and distribution of the input field [56]. The diagram in Figure 6 shows the mirroring of an arbitrary input in a multimode waveguide.

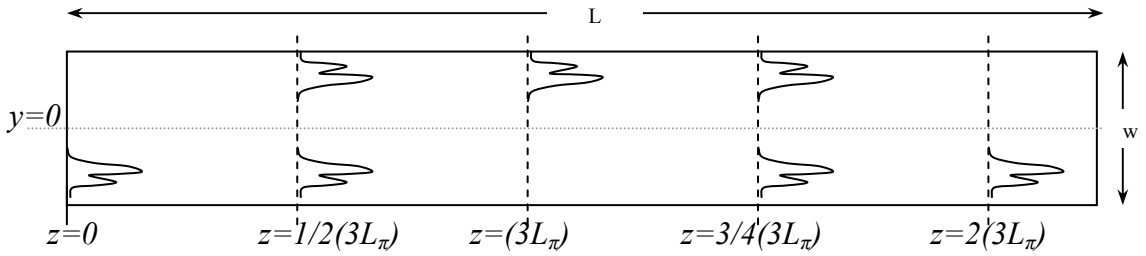

Figure 6. Self-Imaging in a multimode interference structure

The ability for a multimode region to manipulate an input field in this way provides great potential in WDM as well as power splitting applications. In this thesis we will consider a special case of the Multimode Interference (MMI) structure used to split power in which the input field is provided to the center of the multimode region. In this type of structure dividing of the input in to N output signals will occur at a length of $3L_\pi/4N$ [56].

2.7 Summary

The theory presented in this chapter sets the foundation for understanding and designing the photonic devices fabricated and presented in this thesis. The single mode formulation will serve as a starting point to the rib waveguide design. Coupled-mode theory will provide the necessary relationships to model both the 3dB coupler and wavelength

selective directional coupler. The result of coupled-mode theory will be used to map and predict simulation data, to reduce optimization time. The understanding of the waveguide bend will be used to characterize losses in the bending regions of each coupler. Finally, self imaging sets the foundation for the multimode interference splitter.

Chapter 3: Waveguide Analysis Methods

Accurately modeling the field profile and propagation within a waveguide is critical to the design of a successful device. This is particularly important for directional couplers as the coupling distance is closely tied to the propagation consent, β, of each waveguide. It is also important for ensuring matched modes between various structures; a mismatch will result in high losses [57]. Three common methods, Effective-Index Method (EIM), Beam Propagation Method (BPM), and Finite Difference Time Domain method (FDTD), used in solving for these field profiles will be discussed. Each method has its advantages and disadvantages in terms of simplicity and accuracy depending on the structure being

simulated. Understanding these tradeoffs will provide the basis for selecting the optimal method for designing each device in this thesis.

3.1 Effective-Index Method

The Effective-Index Method (EIM) is one of the most well know techniques for determining the mode propagation constant of 3D structures, such as buried, and ridge waveguides [57]. Discovered more then three decades ago this method was first used in integrated optics to describe guided wave prisms, lenses, and gratings [46]. The EIM method continues to be the most simplistic and intuitive method of quantitatively understanding multidimensional waveguides. The power of this method comes from its ability to reduce a complex 2D cross-section to an equivalent 1D planer waveguide. The decomposition of these structures is possible by assuming that the electromagnetic field distribution is linearly polarized, valid for most waveguide structures. The linearization of the problem allows for the full vector wave equation to be separated into a set of semi-vectoral equations that can solve the field distribution of each dimension of the waveguide's cross-section independently [58]. A representation of the decomposition of the scalar wave Equation (26) into its x and y components, Equations (27) and (28) are given where the scalar field distribution ψ is in the form $\psi(x,y) = f(x)G(x,y)$ [57].

$$\frac{\partial^2 \psi}{\partial x^2} + \frac{\partial^2 \psi}{\partial y^2} + \left(k^2 - \beta^2\right)\psi = 0, \qquad \textbf{(26)}$$

$$\frac{\partial^2 F}{\partial x^2} + \left(k_0{}^2 n_{eff}{}^2 - \beta^2\right)F = 0, \qquad \textbf{(27)}$$

and

$$\frac{\partial^2 G}{\partial y^2} + k_0{}^2\left(n^2 - n_{eff}{}^2\right)G = 0. \qquad \textit{(28)}$$

The variable n_{eff}, where this method gets its name, is introduced to relate the independent components of the wave equation. The effective-index method is solved by assuming a direction as the dependent variable, and splitting the waveguide in that direction into a series of planer structures. Each of these sections can be represented as an effective-index by solving either the Eigen Value Equation given earlier for the desired mode, or directly solving the simi-vectorial wave equation for that dimension [24][48]. The effective indices of each section can then be used to model an equivalent plainer structure, which can be solved using the simi-vectorial equation in the other dimension [48]. This equivalent slab structure represents a much simplified problem as compared to solving the full wave equation on the original two dimensional cross-section. The process of the effective-index method and its application to a ridge waveguide structure is shown in Figure 7 [48] [59].

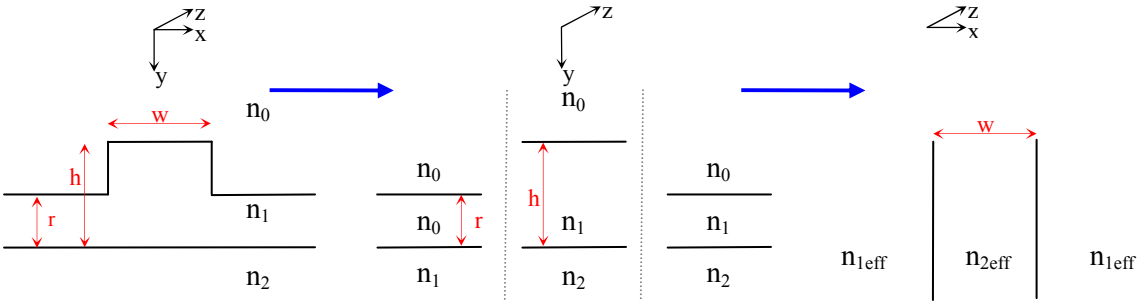

Figure 7. Concept of the effective-index method

It should be noted that the effective indices in an SOI structure tend to be close to the core index of 3.5, and are always being greater then the cladding index. The EIM, being a simplification of the guided wave problem, can break down in certain cases. This method tends to become inaccurate for wavelengths close to cutoff, poorly confined modes, highly complex structures, and large index steps [57]. Because each dimension is made to be linearly independent a different solution can result depending on which dimension is taken as the dependent variable, potentially introducing further inconsistency into the solution.

3.2 Finite Difference Time Domain Method

The Finite Difference Time Domain Method (FD-TDM) is the most straightforward technique for determining the behavior of a propagating electromagnetic wave as it solves the time-dependent Maxwell curl equations directly [13]. The full vector form of these equations, where E and H represent the three dimensional electric and magnetic field respectively are given in Equations (29) and (30) [48].

$$-\mu \frac{\partial H}{\partial t} = \nabla \times E \,, \qquad \textbf{(29)}$$

and

$$\varepsilon_0 \varepsilon_r \frac{\partial E}{\partial t} = \nabla \times H \,. \qquad \textbf{(30)}$$

The solution to these time dependent equations is found by applying a mesh to the desired simulations space, and solving for the field components at each node at given time increments. This method is extremely powerful, and is considered to be the most exact solution, with the only error being the numerical discretization approximation in space and time [57]. The FD-TDM has the ability to accurately model many optical phenomena, such as propagation, scattering, reflection, diffusion, and polarization effects. It can also describe the behavior of wave propagation in anisotropic mediums and dispersion without the assumption of specific field behavior [58]. Because the mesh size can be selected as small as desired FD-TDM calculations can analyze fine submicron and large index contrast structures [58]. Another advantage of this method is that it supports arbitrary time varying input fields, such as Gaussian modulated pulses. Such input fields can be used to determine the response of a system to a wide range of frequencies within a single simulation by using the Fourier transform to normalize the frequency content at the output with that of the modulated input [47]. Because the FD-TDM is computed in the time domain it is ideal for visualizing the propagation of the field through a structure, allowing for a intuitive understanding of device behavior [60].

The trade off of the FD-TDM being extremely accurate is that it is computationally expensive [58]. The memory and computation time required to solve the 3D vector equation is prohibitive even for small simulation areas, making the FD-TDM impractical for design optimization. Waveguide splitters for example require coupling distances on the order of several hundred microns. Even conservative meshing of a simulation space

this size would take several days to a week simulate on a conventional PC (personal computer).

3.3 Beam Propagation Method

The Beam Propagation method is another powerful technique for determining the behavior of a traveling electromagnetic wave. Several BPM algorithms exist however only the Finite Difference Beam Propagation Method (FD-BPM) will be discussed here. FD-BPM is similar to the FD-TDM in that it represents Maxwell's partial differential equations (PDE's) in terms finite differences, giving it the ability to accurately model a wide range of structures [61]. What makes this method unique is that it solves the propagating wave problem entirely in the frequency domain. The advantage of this method is that it allows the field at each point along the waveguide to be solved serially, effectively reducing the dimension of the problem by one [13]. Rather than solving Maxwell's PDE's for 3D structures over an index tensor, or for the 2D problem an index matrix, the BPM solves the problem over an index matrix or vector respectively [13]. The BPM equation also allows for the step size in the direction of propagation to be many times larger than the optical wavelength, reducing the required mesh density without dramatically affecting the results [61]. The simplification of the wave equation using the BPM provides large advantages in computational efficiency, faster computation times, and lower memory requirements, as compared to the FD-TDM [13]. The increased speed of the BPM allows for its effective use in iterative optimization algorithms to design waveguide devices such as directional splitters, making the method highly desirable [13].

The conversion of the classical time domain wave equation into the BPM equation is accomplished through the use of two assumptions. The first is that the electromagnetic field, $\psi(x,y,z)$ can be represented in terms of a slowly varying envelope term $\phi(x,y,z)$, and a fast oscillatory phase term $e^{-jn_{eff}k_o}$ as shown in Equation (31), where n_{eff} is a reference index, typically that of the cladding [48].

$$\psi(x,y,z) = \phi(x,y,z)e^{-jn_{eff}k_o}. \qquad \textbf{(31)}$$

The second assumption is that $\partial^2\phi/\partial z^2 = 0$, that is the second derivative of the slowly varying envelope with respect to direction of propagation, z, can be neglected. This assumption is referred to as the Fresnel or paraxial approximation. Neglecting this term implies that the optical system has an axis on which the majority of light travels. Using these two assumptions the BPM equation can derived, and is given by Equation (32). The Laplacian, $\nabla_\perp{}^2$, is defined for the directions orthogonal to propagation (x, and y) [48].

$$2jn_{eff}k_0\frac{\partial\phi}{\partial z} = \nabla_\perp{}^2\phi + k_0{}^2\left(n^2 - n_{eff}{}^2\right)\phi. \qquad \textbf{(32)}$$

The BPM equation is solved by specifying a desired input field $\phi(x,y,z)$, at an input plane z_0. The field is propagated by iterating ϕ along the z-axis, and using finite differences for the x and y derivatives [62]. The assumptions made in deriving the BPM

equation impose several limitations on the structures that can be accurately simulated. Because the BPM method assumes the paraxial condition, structures which have large angles with respect to the optical axis will break down [61]. The frequency domain representation of this equation limits it to only being able to model weak nonlinearities, and the envelope function assumes that the x-y profile as well as amplitude in the z direction is slowly varying [62]. The other major limitation of BPM is that it is unable to model a large number of reflections, thus devices such as resonators, can not be simulated. In general, the FD-BPM is preferable over the FD-TDM for single pass, axial structures that are slowly varying [61]. Waveguide devices such as couplers, tapered waveguides, Multi mode interference (MMI) splitters, and large radius S-bends can be simulated effectively through the BPM.

3.4 Summary

Each of these three simulation methods have their advantages and disadvantages. It will be determined that for the devices designed in this thesis the BPM is an adequate approach, as it can deal with the complex structures which are limited in the EIM, and is computationally faster then the FDTD method. As all photonic devices designed in this thesis conform to the paraxial condition and do not rely on reflections, BPM will yield accurate results.

Chapter 4: Waveguide Analysis and Design

The design and simulation of several types of micro-optic waveguide devices are addressed in this thesis. These devices will include single/multimode waveguide's, directional splitters including y-splitters, Multi-Mode Interference (MMI) splitters, 3dB splitters, and wavelength splitters. An SOI substrate will be used for all devices as it provides a high index contrast and the potential in the future to serve as an integrated platform for microelectronics and optics. The simulation of these devices is accomplished

with the use of the Optiwave software package which includes the FDTD and BPM algorithms for propagating electromagnetic fields. The simulation algorithm and meshing density used are chosen to allow for the fastest computation time, without compromising the accuracy of results. Unless otherwise stated these simulations are limited to the TE polarization case. The TM mode is neglected as it has considerably higher propagation loss, particularly in waveguide bends. These structures are also concerned primarily with intensity distribution not phase. Each device will be designed to operate at wavelengths ranging from 0.98μm to 1.55μm, as these wavelengths have high transmissivity in silicon, and are common in long haul telecommunications. Specific design parameters of each device are determined using theory as well as with the simulation and iterative optimization techniques. In addition to each design dimension conforming to theory, and being validated by the Optiwave simulation software, these devices, where applicable, will be constrained by the fabrication limitations of the RIT microfabrication facilities. These variables will allow the majority of the devices simulated to be fabricated and tested.

4.1 Single Mode Rib Waveguide

The design of the straight single mode rib waveguide is considered first as it is the fundamental building block for all devices considered in this thesis. A simple understanding of the dimensions a rib wave waveguide must have to meet the singlemode condition is given by Soref et al and is depicted graphically in Figure 4 [52]. In

determining the optimal values for parameters a, b, and r, fabrication limitations, as well as physical performance, must be considered.

The minimum width of the waveguide is physically constrained by the smallest lateral dimension that can be fabricated. This is determined by the resolution of the lithography tool. The Cannon FPA 5000 il stepper used at RIT can reliably print patterns with 1μm feature sizes. The smaller the minimum dimension, the higher the integration density can be obtained. There are however several practical advantages to letting the waveguide width be larger than the fabrication limit. The first advantage is that losses from sidewall roughness decrease exponentially as the width increases, losses can be neglected entirely for sizes larger than a few microns. The other primary advantage of making the width large is that it aids in reducing coupling losses from the input. For coupling methods such as butt coupling from a fiber the beam diameter is limited by the core, typically 5 to 100 microns depending on the type of fiber, number of modes, and wavelength of operation [63] [64]. When using a lens to focus light into a waveguide, the spot size is diffraction limited as given by the equation for the first minimum of the Airy function, $d_{diff}=2.44\lambda f/d_0$, where f is the focal length of the lens, and d the diameter of the laser beam being focused. The diffraction limited diameter is typically between 5-10μm for NIR wavelengths. The closer the waveguide cross-section area can match that of the coupled beam, the lower the losses will be. The upper constraint on waveguide width is limited by insuring the single mode condition.

The total height of the waveguide (2bλ) is determined by the thickness of the thin silicon layer on the SOI wafer. The thickness of thin silicon layer can be chosen to be nanometers up to several microns depending on the SOI wafer fabrication process used. The parameter 'b' must also satisfy the condition, $2b\sqrt{n_1^2 - n_2^2} \geq 1$. Other factors such as minimizing size mismatch between the beam and waveguide are impotent when picking the ridge height. The ratio between total rib height to the height of the slab region, r must be chosen such that it meets the shallow waveguide condition ($r \geq 0.5$) insuring single mode operation in the lateral direction. Picking r to be large has the advantage of increasing the mode confinement, which can reduce bending losses [4].

Based on these design constraints the rib width (2aλ) was chosen to be 2μm (a=1.02 @ λ=0.98μm), the rib height to be 2μm as well (b=1.02 @ λ=0.98μm), and the ridge height factor of 0.6. These dimensions are sufficiently large that they can be realized with the tools available at RIT's Semiconductor and microelectronics fabrication lab. Based on the plot of the single mode condition, variation in these dimensions anticipated during fabrication will not push the waveguide into multimode operation, making the design more robust. The parameters satisfy $2b\sqrt{n_1^2 - n_2^2} = 2*1.02\sqrt{3.45^2 - 1.44^2} = 6.39 \geq 1$. Locating the point on the graph in Figure 4 corresponding to these dimensions (a/b=1, b=1.02, r = 0.6), confirms that this rib waveguide design will operate in the single mode region for both hybrid EH and HE polarizations. A diagram of the single mode rib waveguide structure designed is given in Figure 8.

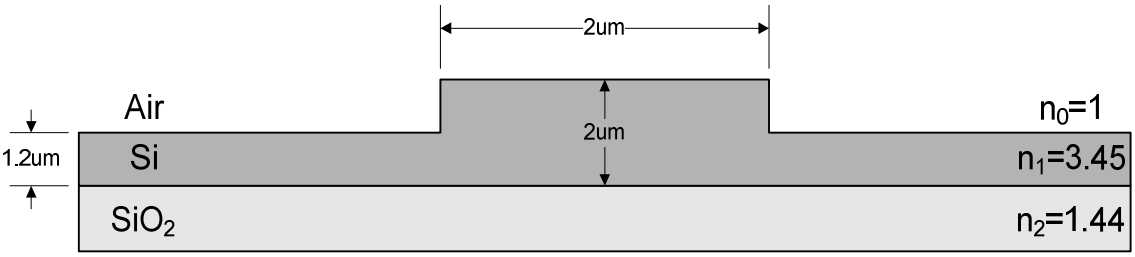

Figure 8. Single mode rib waveguide

In order to confirm the single mode behavior of the waveguide and obtain a detailed view of the field distribution the structure is simulated with the Optiwave Mode Solver. The normalized amplitude distributions for both the first and second modes of this structure at a wavelength of 0.98μm are seen in Figure 9. The wavelength of 0.98μm is used as it is the shortest wavelength of operation and will ensure singlemode operation for larger wavelengths.

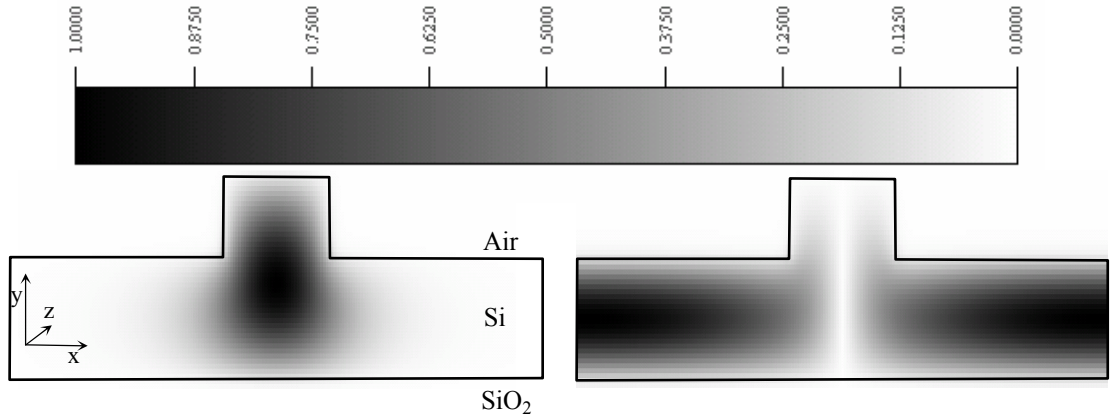

Figure 9. Intensity distribution (λ=0.98μm) for single mode (left) and second order mode (right) of a single mode waveguide

As observed the fundamental mode, on the left side of Figure 9 is confined within the ridge portion of the structure; however the second mode, seen on the right, exists only in

the slab region. Because the second mode, as well as higher order modes of this finite rib structure are not well confined they will radiate into the substrate. The lossy propagation of all modes other than the fundamental mode ensures that this rib structure will operate in the single mode region. Another way to confirm the single mode behavior of this structure is to excite the input of the waveguide with a Gaussian beam and observe the Field distribution at several points along the direction of propagation (z-axis). Because the Gaussian beam is composed of a many modes much of the beam will dissipate after a finite propagation distance, only the fundamental mode that is supported by the waveguide will travel indefinitely. Using the BPM the normalized amplitude distribution at various points along the straight single mode waveguide was determined and are shown in Figure 8. After approximately 300μm the majority of high order modes have dissipated and the single mode distribution seen in Figure 10 (lower middle) emerges confirming that only the single mode distribution designed fore will propagate.

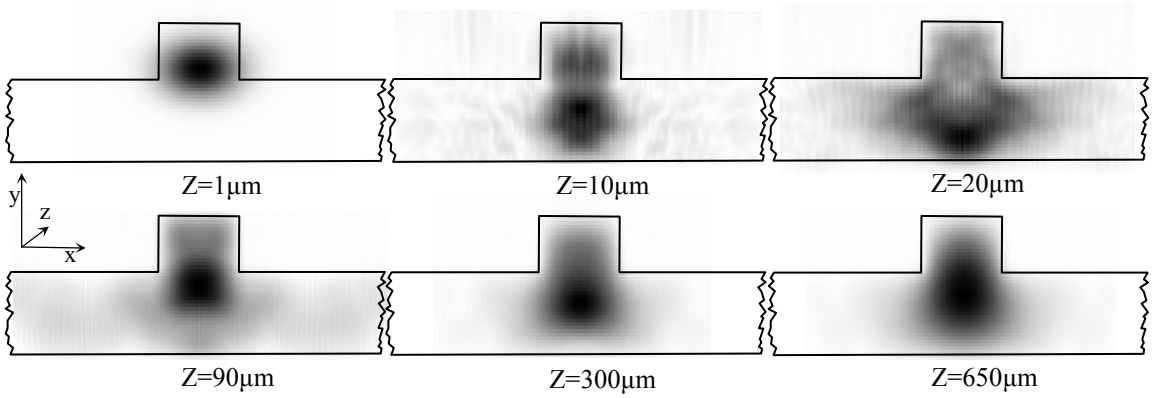

Figure 10. Amplitude distribution at various points along the single mode waveguide, when excited with a Gaussian field (λ=1.31μm), and propagated using the BPM

4.2 Multi-mode mode rib waveguide

The design process of the multi-mode rib waveguide is identical to that used for the single mode structure. Figure 4, is used to determine the approximate dimensions required then the OptiWave mode solver is used to confirm the results. It is important that the design of this structure, as well as others used in this thesis, follow the same fabrication process steps. By making each structure conform to the same fabrication technique all structures can be implemented on a single wafer at the same time. Applying this constraint means that all structures must have the same vertical dimensions such as rib height factor b and relative etch depth r. Making b = 0.75, and r =0.6 as used for the single mode waveguide, leaves only the rib width factor a, as a design variable for the multimode waveguide. Increasing the width of the waveguide to 4μm considerably increases the a/b ratio, and thus pushes the structure into the multimode region. In fact the larger the width of the rib is made, holding other dimensions constant; the more modes will be supported by the structure. The amplitude distribution of the first three modes (λ=1.55μm) of this multi-mode structure (w=4μm) can be seen in Figure 11. Because the waveguide exhibits multimode behavior for longest wavelength of interest it is also ensured to have multiple modes at shorter wavelengths.

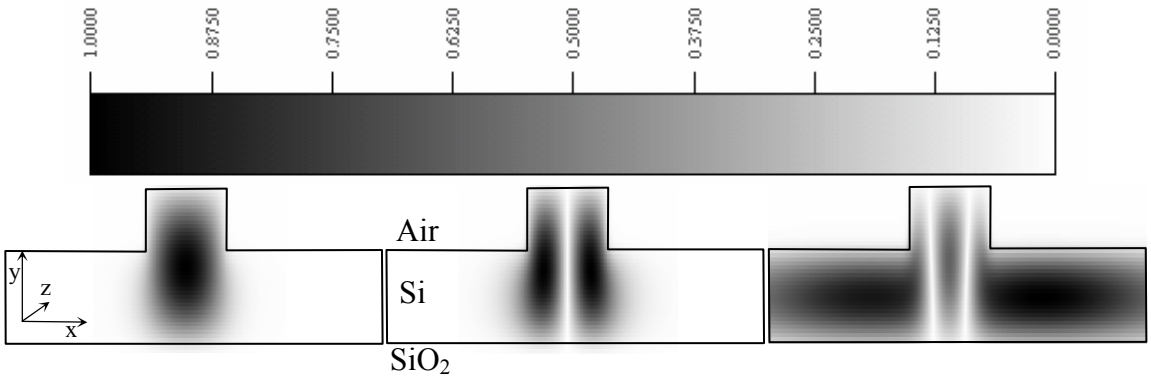

Figure 11. Amplitude distribution (λ=1.55μm) of fundamental (left), second order (middle) and third order (right) modes of multimode waveguide

It can be seen in Figure 11 that the rib structure will support two modes at this wavelength, the third mode seen on the far right of Figure 11, is not confined, as it exists only in the thin silicon layer, as such it will not propagate indefinitely.

4.3 Y-Splitter

The singlemode y-branch is a device based on the single mode waveguide and two; either curved or angled SM waveguides. The primary purpose of the y-branch is in split an optical signal. This is an important passive structure as it serves as a building block for more complex devices, such as certain types of optical switches and modulators [65]. Two types of such splitters will be examined in this thesis, the s-bend, and linear y-branches. These types refer to the waveguide transition that is used to connect the structures single input to its two outputs. A diagram of each of these structures in the x-z plane is shown in Figure 12. These diagrams show the ideal operation of these structures with an input power of 1, which is equally split with no losses.

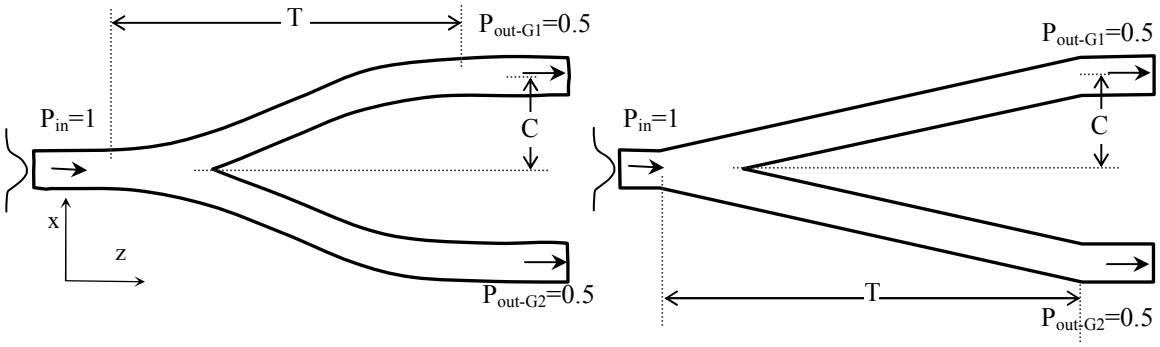

Figure 12. Ideal Curved y-branch (left), linear y-branch (right)

For each type, three y-branches having different dimensions will be designed, and simulated using the Optiwave BPM algorithm. The BPM is used since these devices are near paraxial in the direction of propagation and do not have many reflections. Each simulation is done at a wavelength of 1.55μm and meshing of 10pts/μm in the y direction, 30pts/μm in the x direction, and a propagation step in the z direction of 0.1μm. These simulation parameters will ensure relatively accurate results. It is important to note that losses determined through simulation are highly dependent on the step size and meshing used. If a mesh is too large, losses will be considerably larger than for the ideal simulation. The mesh in this case is chosen to provide a compromise between the inaccuracy of the simulated output and computation time which exponentially increases with mesh density.

The first design has a branch separation of 2C=10μm at the output which spreads out from the single input over a distance of T=1200μm. The 10μm separation distance was

chosen as it is the minimum distance that will allow for the output ports to be resolved on the fabricated device, as governed by the diffraction limited condition, and available measurement equipment. The transition length will allow for low loss bends, and angles that are less then 2° [65]. The single mode rib profile is used for the waveguide design. A diagram of the simulation of the s-bend type of this device is shown in Figure 13.

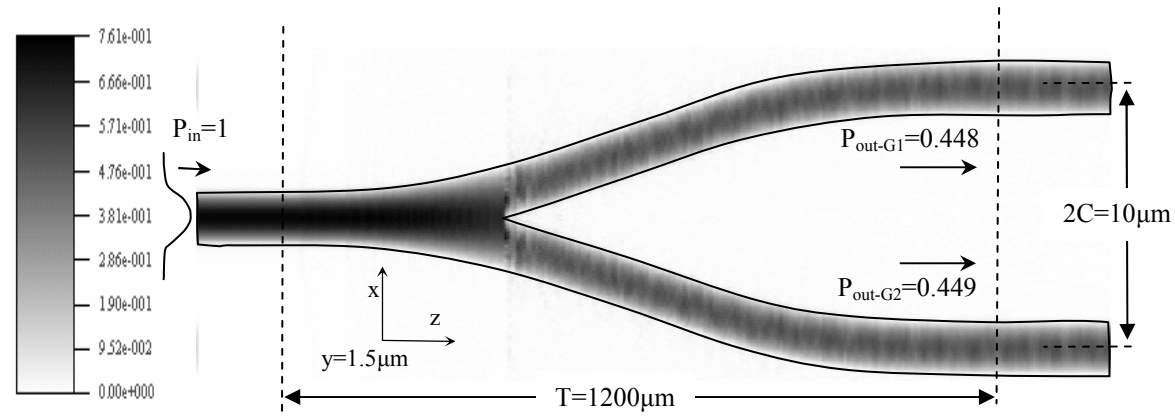

Figure 13. Amplitude distribution in Y-Branch, C=5µm, T=1200µm

The simulation in Figure 13 represents a slice in the x-z plane (top view) of the amplitude profile within the rib structure at y=1.5µm where the origin is located at the surface of the cladding oxide. Although the input field is Gaussian, when testing the fabricated device, a matched mode is used for each simulation in order to eliminate losses incurred by higher order modes, and to more clearly observe the losses caused by the waveguide bend. The use of a modal input is a reasonable assumption for the field as it represents the steady state distribution after the higher modes of a Gaussian beam have radiated into the cladding. It can be seen in Figure 13 that the normalized input power is effectively split

in half, however 10.3% of the input is lost due to radiation in the bending structure. The radiation of these losses can be clearly seen in Figure 11 depicting a slice in the z plane near the bending region (z=400μm).

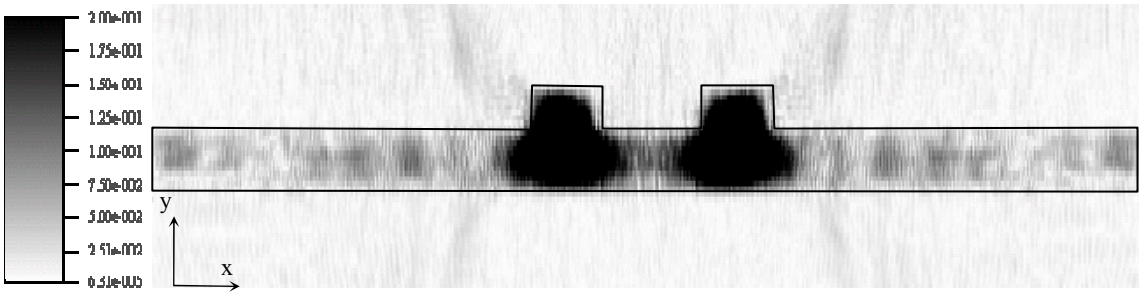

Figure 14. Amplitude distribution in slice of S-bend at z=400μm

In this plot the amplitude is clamped at 0.2 so low level radiated power can be seen. It is apparent that the maximum radiated modes occur in the outer cladding region, as is expected from the theory of a waveguide bend. A similar y-branch structure where linear transition segments are used in place of the s-bends is simulated as shown in Figure 15

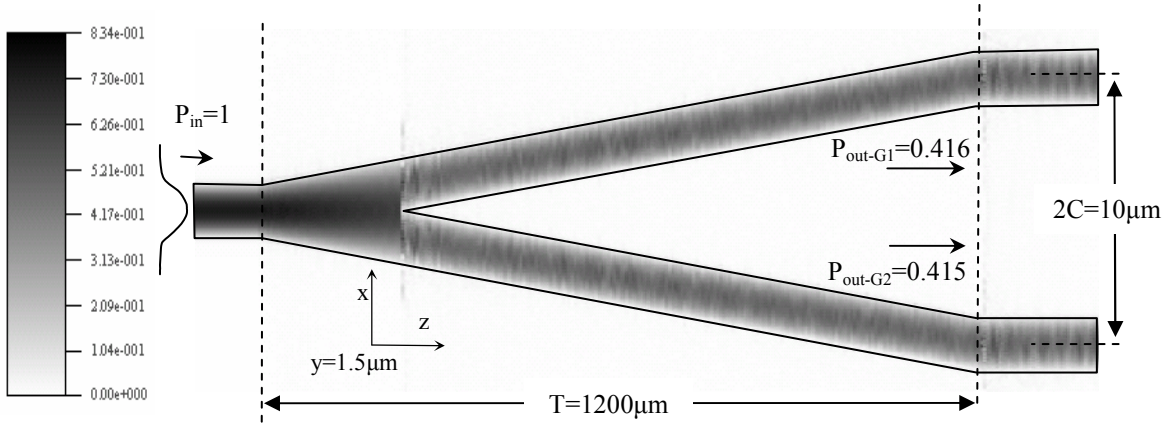

Figure 15. Amplitude distribution in linear y-branch, C=5μm, and T=1200μm

Although the primary dimensions are identical the losses incurred by the linear structure are slightly higher, amounting to approximately 16.9% of the input power. The increase in losses is attributed primarily to the more abrupt change of the linear waveguide structure as compared to the smooth transitions of an s-curve.

The second branch design reduces the transition region to T=600µm, and leaves the separation distance as 2C=10µm. A diagram of the s-bend type of this y-branch is given in Figure 16.

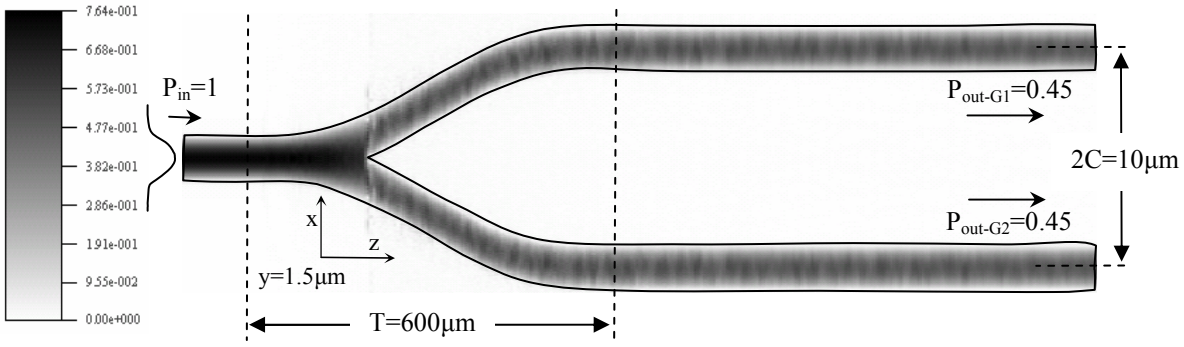

Figure 16. Amplitude distribution in Y-Branch, S-bend with C=5µm and T=600µm

Compared to the s-bend where T=1200µm this device has nearly the same loss at 10%. Although the radius of the bend is less in this device, which would have the effect of increasing losses, the bend also occurs over a shorter distance. The impact of these two effects counteract each other, contributing little change to the net loss. The linear form of this design is given in Figure 17.

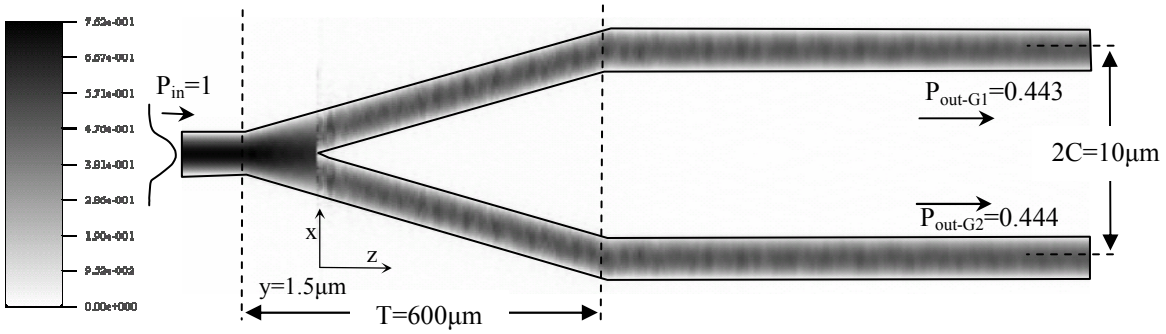

Figure 17. Amplitude distribution in Y-Branch, linear bend with C=5µm and T=600µm

As expected the linear structure exhibits higher losses (11.3%) as compared to an equivalent curved structure. The loss however is still much less then the long linear structure (T=1200µm) previously modeled, implying that a factional reduction in length has a dominant impact on reducing losses compared to the same fractional reduction in waveguide angle. The effect is more extreme in the linear case as losses are eventually distributed over the separation distance where as in an s-curve losses are concentrated in the bend regions.

The final design to be simulated and implemented is a y-branch with 2C=20µm, and T=1200µm. A diagram of the s-bend form of this structure is given in Figure 18.

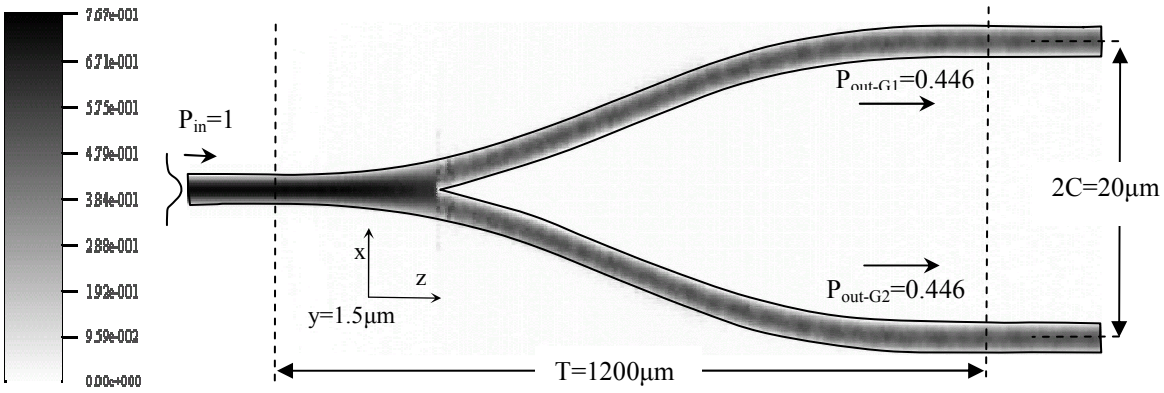

Figure 18. Amplitude distribution in Y-Branch, S-bend with C=10µm and T=1200µm

The losses in this structure amount to 10.8% of the input power, slightly larger then the first structure designed with the same transition length and half the separation width. This increase in losses is expected as the propagation length is not changing and the radius of the bends is decreasing due to the larger separation. The linear type of this design is given in Figure 19, and as expected the losses are higher (16.8%). These losses are not much different then the structure with only a 10µm separation as losses in the linear structure with waveguide angles less the 2% are primarily attributed to propagation distance in the angled region.

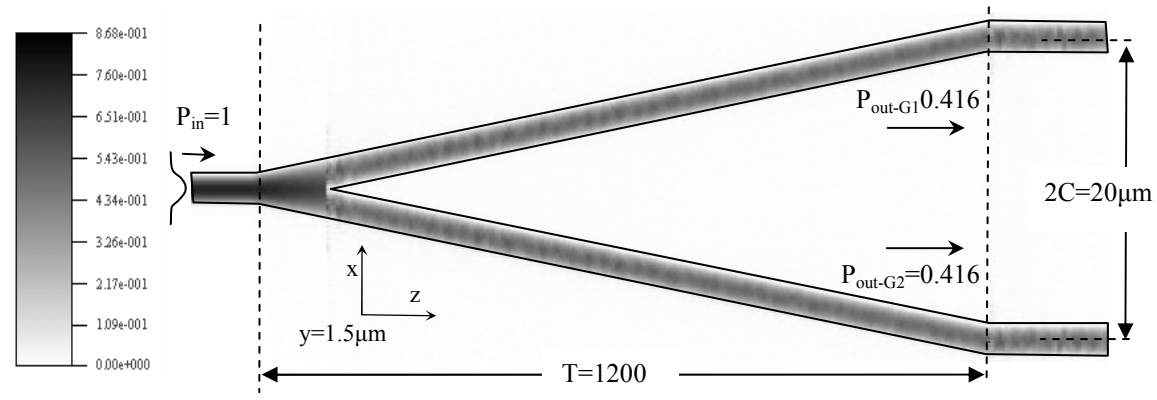

Figure 19. Amplitude distribution in Y-Branch, linear bend with C=10µm and T=1200µm

In summary, the results of these simulations show that regardless of the transition length and waveguide separation; the s-bend curve will consistently exhibit lower losses then the linear transition. It was observed that increasing the length of the bending region does not always decrease losses, because at these shallow bends the propagation length in the bending area has a larger effect on losses then bending angle. A table summarizing these simulation results is given in Table 1.

Table 1. Summary of Y-splitter loss data

Linear/S-curve	Transition length (T)	Separation (2*C)	P_{out-G1}	P_{out-G2}	% loss
S-curve	1200µm	10µm	0.448	0.449	10.3%
Linear	1200µm	10µm	0.416	0.415	16.9%
S-curve	600µm	10µm	0.45	0.45	10.0%
Linear	600µm	10µm	0.443	0.444	11.3%
S-curve	1200µm	20µm	0.446	0.446	10.8%
Linear	1200µm	20µm	0.416	0.416	16.8%

In general, the largest losses occur for large separation distances, large transition lengths, and the use of the linear waveguide. The lowest losses occur in short transition distances, small separation distances and with the use of the S-bend transition. These basic splitters provide a foundation for initial testing of the device wafer and provide a valuable

understanding of the losses incurred in waveguide bends. This data will prove valuable to reduce losses of the other devices designed which also require waveguide separation regions.

4.4 3dB-Coupler

The 3db-Coupler, also called the 50-50 splitter, performs the same functionality as y-splitter, it divides the power of an optical signal into two equal parts. This device is composed of two parallel waveguides in close proximity for a distance referred to as the coupling length (L_{3dB}), after which point they separate in opposite directions to the output ports. The separation of the waveguides has the purpose of dramatically reducing power transfer between the waveguides after the signal has been split. All 3dB structures studied in this thesis will uses the s-bend transition to separate the waveguides as it provides lower losses compared to the linear transition. A diagram of the 3dB coupler in its ideal operation can be shown in Figure 20.

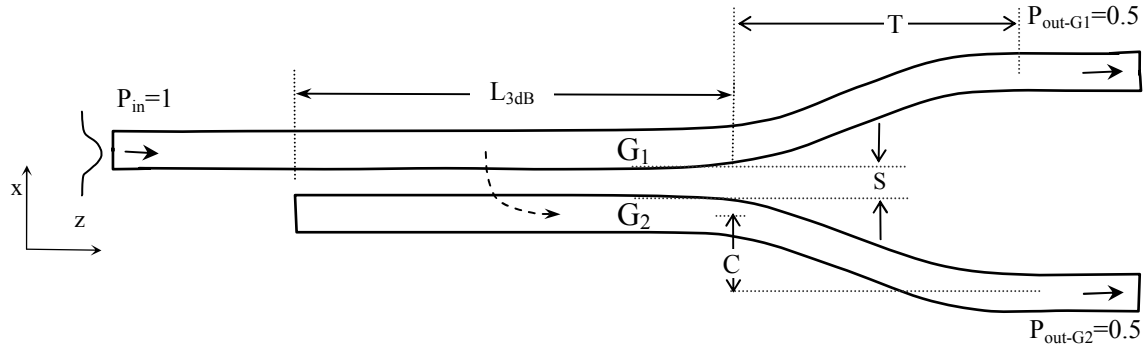

Figure 20. A schematic of a singlemode 3dB coupler

The primary difference between this device and the y-branch device is that it relies on evanescent coupling rather than a direct change in the waveguide structure to divide the signal. The advantage of this method is that it allows for uniformity in the direction of propagation, considerably reducing losses by minimizing the number of reflections and the amount of sidewall interaction that a mode encounters. The coupling method is also powerful because it can be easily implemented to split a signal at arbitrary power ratios. This type of coupler however, has several negative design implications as well. The nature of the coupling structure requires it to be at least several hundred microns in length, a considerable disadvantage when attempting to integrate large optical systems onto a single die. These structures also have poor tolerance to fabrication variation, because the coupling continent K is closely tied to device geometry. Even small variations that occur during fabrication can dramatically change coupling behavior. The wavelength dependence of K further limits the performance of a given coupling structure. Unlike the y-splitter which will split any mode supported by the waveguide equally, the 3dB coupler will only work effectively at the wavelength for which it is designed.

Several 3dB couplers will be designed in this thesis, operating at wavelengths of 1.55μm, 1.49μm, 1.31μm, and 0.98μm. The previously designed singlemode rib waveguide profile will be used for these couplers to maintain design consistency. At each of these wavelengths three different variants of the coupler will be studied to observe the effects of changing waveguide separation at the output, and curve bending radius. These variations, once fabricated, will also provide a wide range of test structures. The design

and simulation of the 3dB coupler will be accomplished with the use of BPM as the structure satisfies the small angle approximation.

For each of these splitters the waveguide separation in the coupling region will be chosen to be greater than 1.5μm to ensure compliance with the minimum feature size of 1μm and to leave room for tolerance. This separation will also be sufficient to keep the required device length under a few hundred microns. As the output waveguide separation and bend transition length are also fixed for a given structure the coupling length is left as the only design parameter to be optimized. A looping algorithm written with the Opti-BPM scripting language is implemented to iteratively change the length of the coupling region and determine the output power in each branch as a function of coupling length. A sample of a script used to generate and characterize a 3dB splitter can be found in Appendix B. The execution of this script will provide a plot of the output power in each waveguide verses iteration number. From this data an optimal coupling length is determined by where the normalized power curves for each output port intersect. Other optimization methods, such as the bisection algorithm, converge on a solution more quickly. An in-depth consideration of this algorithm is discussed in [66]. A considerable portion of the time required to simulate these structures was invested into overcoming several bugs discovered in the Optwave software package, particularly with respect to differences in how the scripting language is interpreted by the GUI and simulator. Each problem encountered was discussed with an Optiwave service representative (Steve Dodes) and e-mail correspondences can be found in appendix D.

Although iterative algorithms are powerful for solving complex design problems they involve considerably more computation time as multiple simulations must be executed. For this reason it is unpractical to apply the same high mesh and small step used for a single simulation. The optimization script will be run using a large mesh (x-mesh=10pt/μm, y-mesh=10pt/μm, and step=1μm) to increase the simulation speed. Once an approximate value for L is determined a higher resolution mesh and step (x-mesh=30pt/μm, y-mesh=10pt/μm, step=0.1μm) was used to improve the accuracy of the results. The y-branch structure was also simulated with these same higher meshing parameters, in order to make the structures easy to compare.

The first 3dB coupler variation has a s-bend separation of C=4.3μm, a bend transition region of T=410μm, and a coupling region separation of S=1.5μm. This leads to an output port separation of 12.1μm as measured from the centers of each output waveguide (4.3μm (bend separation)*2+2μm (waveguide width)+1.5μm (separation in coupling region)). These dimensions were chosen to be similar to the small y-branch structure previously analyzed to provide a basis for loss comparison between splitting structures. Using the looping script, the starting z coordinate of waveguide G_2 is incrementally decreased until the last iteration when it is equal to 0, and in line with the input of waveguide G_1. The field intensity in this structure for this last iteration of the optimization loop can be seen in the upper portion of Figure 21. The diagrams show the results for a model input field of 1.55μm to waveguide G_1.

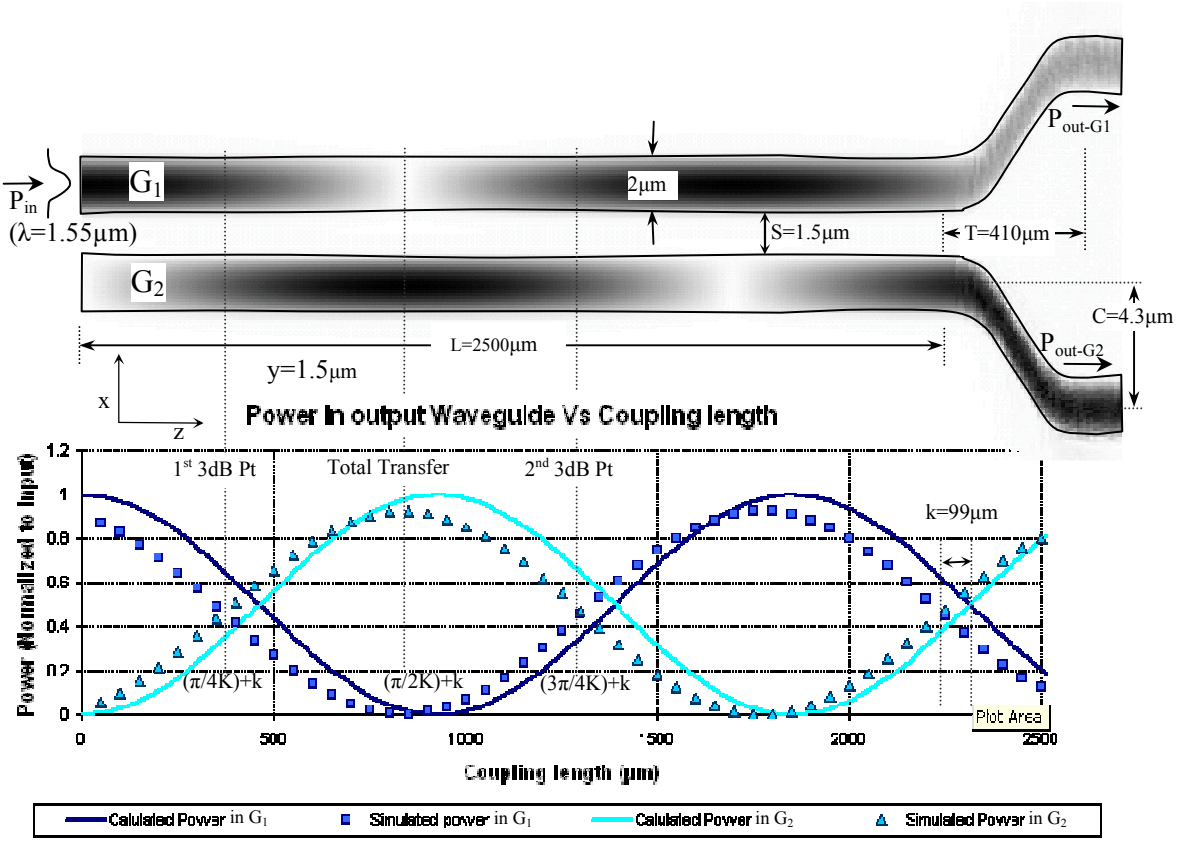

Figure 21. Optimization algorithm results for 3dB coupler with C=4.3μm, T=410μm, and S=1.5μm, operating at a wavelength of 1.55μm

From the intensity distribution it is apparent that the coupling length is sufficient to allow light to transfer back and forth between the waveguides several times. The curve in Figure 21 the coupler depicts the output intensity at the output ports of G_1 and G_2, for each iteration of the optimization loop. The points represent the simulated power in the output waveguides for a given coupling length. The lines represent a plot of the solution to the coupled mode equations in the form $I=sin^2(Kz)$. The coupling rate K, is given by the period of the sinusoid determined through simulation, as such the periods of the simulated and calculated curves will always match. The discrepancy between these

curves is caused by the fact that the equation used to describe coupled-mode theory does not account for nonlinearities introduced by the bending region of the coupler. The lower amplitude of the simulated output in particular is due to the losses incurred in the bending region. It is important to note that the specific difference in amplitude observed in this case is not an accurate measure of bending losses due to the low mesh used for the iterative simulation. The phase offset between theoretical and simulated values denoted by lower case k in Figure 21, is a result of the small amount of non-linear coupling that occurs in the bending region. As the waveguides separate, coupling does not abruptly stop but rather slowly diminishes as K decreases. Because the bending region is constant between iterations, only waveguide length changes, coupling in this region manifests itself as a phase offset. The physical interpretation of this parameter is the length a linear waveguide with the same coupling coefficient K would need to be to equal the amount of coupling experienced in the S-bend transition. In this case the bending region of 410μm is equivalent to an additional k=99μm of linear coupling length (L). The phase offset can be accurately determined by $(K/4)-L_{3dB}$. For large curve transitions a considerable amount of coupling can occur in the bending region. The energy transfer that occurs in this region is not modeled by the solution of the coupled mode equations for two linear waveguides. In order to take into account these nonlinearities the ideal equation can be modified into the form $I=Asin^2(Kz+Kkz)$ where A is the amplitude and k is the phase offset. The power of the BPM is its ability to accurately model these nonlinearities, and provide the information necessary to extract important parameters such as A, and k. The practical

implication of the phase shift k for the 3dB coupler is that the 3dB coupling length is slightly shorter then the length needed if the bend did not exist.

For this structure the coupling coefficient, which is determined directly from the period of energy transfer between the two waveguides by π/period is given as K=1678. The 3dB length, L_{3dB}, of this device is 369.3µm. It is seen that this length is shorter by 99µm then the theoretical value of 468µm calculated by π/4K. This is as expected from the energy transfer encountered in the bending region. Using the coupling length extracted from the iterative simulation and a higher mesh the design of the 3dB coupler is shown in Figure 22.

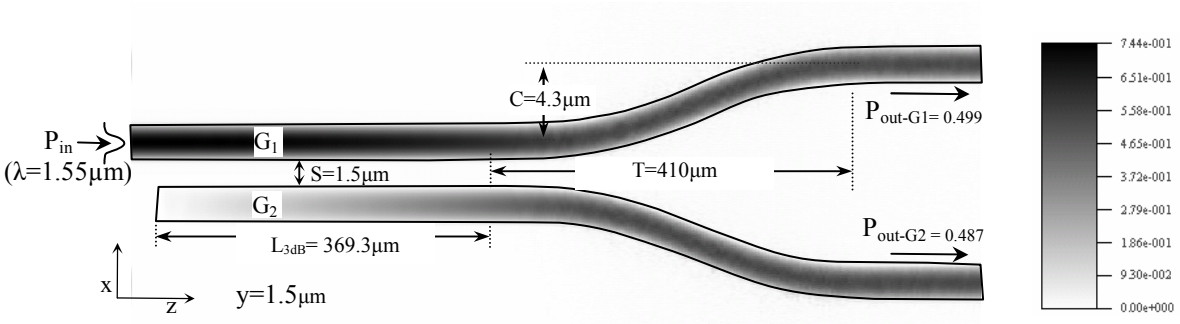

Figure 22. High mesh simulation of 3dB coupler with C=4.3µm, T=410µm, and λ=1.55µm input wavelength

The losses in this simulation amount to 1.4% more then a factor of ten less that what was observed in the y-branch of similar bending radius in the transition region. As coupling has nearly perfect efficiency in simulation, these small losses can be attributed primarily to the waveguide bends. The theoretical reduction of loss makes this device a highly desirable design alternative. However, unlike the y-branch, this structure is asymmetric

making it inherently sensitive to coupling, and meshing parameters. As a result a prefect splitting ratio is difficult to achieve with the simple iterative optimization algorithm. For this analysis results accurate to the hundredths place are sufficient as inaccuracies in fabrication will eventually dominate. The design procedure used above is repeated for the same structure, to determine the coupling coefficient, optimum coupling length, output power, offset k, and losses at the other desired wavelengths. Table 2 summarizes these results.

Table 2. Characteristics of 3dB coupler, C=4.3µm, T=410µm

λ (µm)	K	L_{3dB} (µm)	Offset (k)	P_{out-G1}	P_{out-G2}	Total Loss (%)
1.55	1678.584	369.3	98.593	0.499	0.487	1.4
1.49	1590.327	397.5	96.360	0.501	0.484	1.5
1.31	1339.235	486.6	99.853	0.497	0.487	1.6
0.98	929.555	741.1	103.819	0.498	0.490	1.2

These results clearly depict the dependence that the coupling coefficient has on the wavelength. As wavelength decreases, so does K, as such the required coupling length must increase for a sufficient amount of energy transfer to occur. It is this property of coupling that will form the basis for the wavelength splitter examined later. The variation in the offset k which occurs with wavelength is a more complex phenomena, with its roots buried in the many nonlinearities the coupled-mode. The coupling coefficient has a nonlinear dependence on both wavelength and waveguide separation described earlier. As a result, the effective coupling length of the bending region, at coupling coefficient K, changes slightly with wavelength, and as will be seen later waveguide separation. Other sources of this small variation can be attributed to error in the extraction of the offset

parameter. The exact characterization of this offset will not be addressed, as the deviations that occur have little effect on the design of the structures evaluated in this thesis. Rather these parameters will be stated as a device characteristic to observe more dominant effects, such as will be seen with changes to the structure of the bending region.

The next 3dB coupler to be designed will have S=2.5μm, T= 6000μm, and C=6μm. These dimensions lead to a separation at the output ports of 2C+S+2μm=16.5μm. The large curve transition of this device was chosen primarily to test the limits of fabrication. The maximum die size that can be fabricated is limited by the stepper and mask printing tool to 19mmx19mm. The large curve will take advantage of a considerable portion the size in the z direction. The primary advantage of this increased device size is that it reduces the potential of resolution limited processes related to lithography. In general the larger a device the more ideally it will perform. The increased size will also make the structure easier to cut, cleave and test once it has been fabricated. The 2.5μm waveguide separation in the coupling region was chosen to provide room for tolerance as well, and can achieve the same amount of energy transfer provided that the coupling length is sufficiently increased. As the overall device length is increase to maximize die usage, the required increase in coupling length needed because of a larger waveguide separation will not be an of issue. A diagram of this structure simulated at the last iteration of the optimization loop with input wavelength of 1.55μm is given in Figure 23.

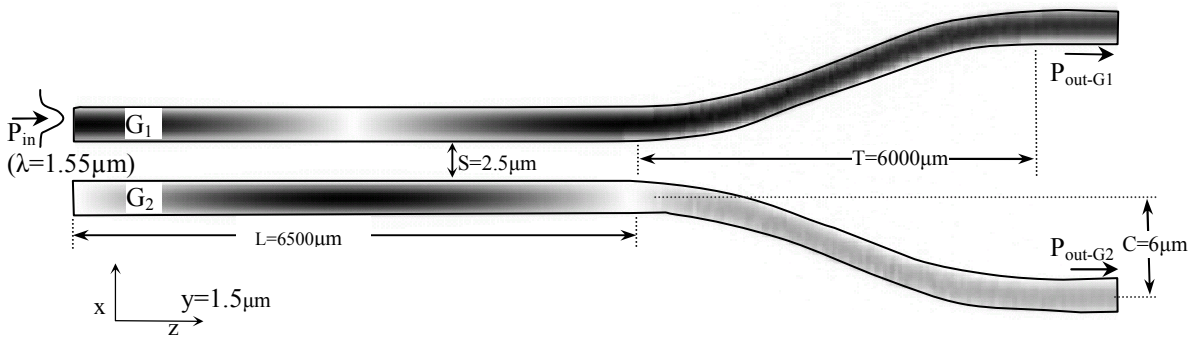

Figure 23. Output from last iteration of optimization algorithm for 3dB coupler with C=6μm, T=1200μm, and input wavelength of 1.55μm

From this simulation it is clear that the 1μm increase in separation between the two waveguides dramatically decreases the coupling rate. The plot describing the power output in each branch verses coupling length for this 1.55μm input is given in Figure 24.

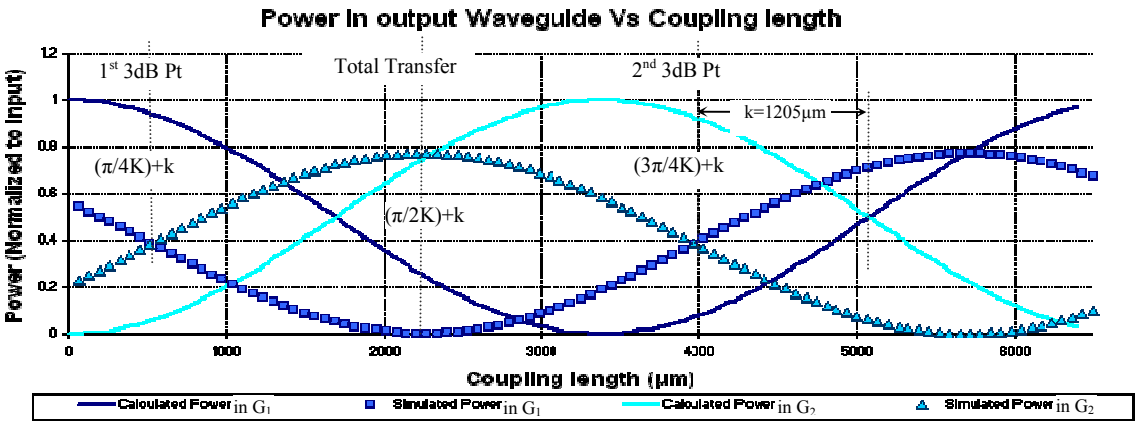

Figure 24. Output power vs coupling length for 3dB coupler C=6μm, T=1200μm, and input wavelength of 1.55μm

The coupling period, extracted from simulation is L_{per}=6898μm, which corresponds to a coupling constant K=455. This device has several other differences resulting from the increased dimensions. The decreased amplitude of the simulated output power as compared to the ideal coupler is a result of losses incurred in the longer bending region.

The phase offset between these curves has increased because of the longer curve transition. As the waveguides separate over a longer distance there is a substantially higher amount of energy transfer that takes place in the bending region leading to an increase of k to 1205µm. From a structure with these parameters the 3dB point occurs with a linear coupling region L_{3dB}=519.3µm. A simulation of this splitter is computed with higher meshing parameters and is shown in Figure 25. It can again be seen that losses are slightly higher at 5.6%, due to the longer curving region.

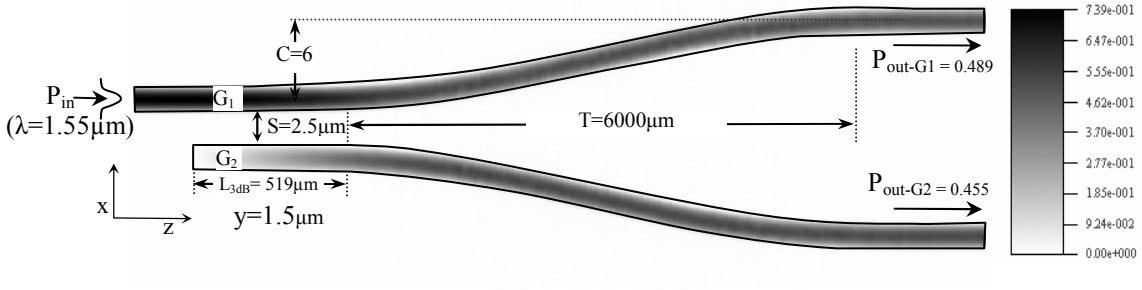

Figure 25. High mesh simulation of 3dB coupler with C=6µm, T=1200µm and 1.55µm input wavelength

A summary of the results for the operation of this coupler at the other wavelengths of interest is given in Table 3. Similar trends in L and K are observed as well as the consistently larger losses. As the coupling interaction within the bending region of this structure is considerably larger the dependence of offset k, on wavelength is more predominant.

Table 3. Characteristics of 3dB coupler, C=6µm T=6000µm

λ (µm)	K	L_{3dB} (µm)	Offset (k)	P_{out-G1}	P_{out-G2}	Total Loss (%)
1.55	455.412	519.3	1205.289	0.489	0.455	5.6
1.49	427.747	632.5	1203.627	0.49	0.45	6
1.31	351.101	1049.1	1187.860	0.496	0.45	5.4
0.98	233.297	2200.9	1165.615	0.448	0.499	5.3

The final structure to be designed will have an identical curve transition region and waveguide separation to the previous device however its output ports will be separated by at least 2C+S+2µm=30µm. The increased output port separation is chosen to provide higher tolerance to output field measurement techniques. Being able to discern the output field of each waveguide with a given measurement device is critical. By making the separation much larger then the diffraction limit (found to be ≈10µm) it is easier to resolve and measure the output power of the fabricated device. A diagram of this structure at the last iteration of the optimization loop at a wavelength of 1.55µm is given in Figure 26.

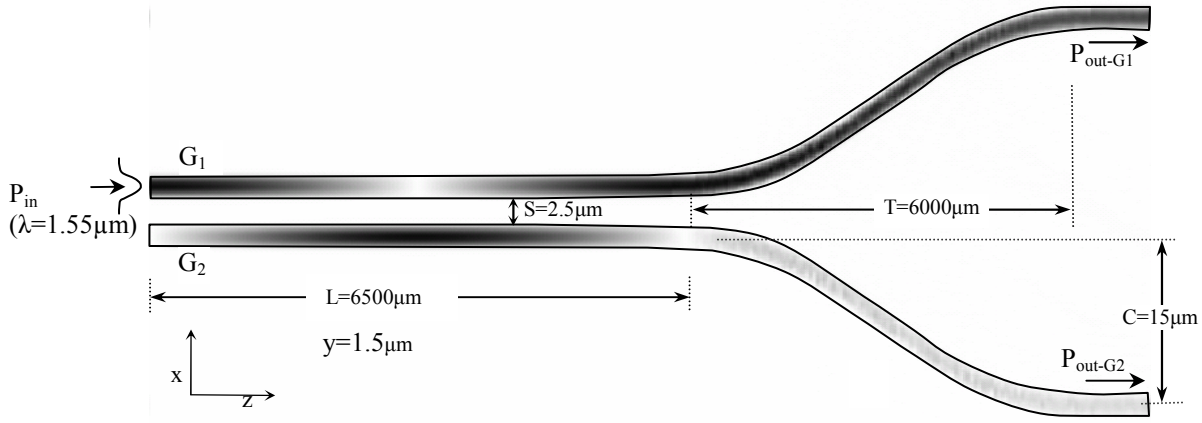

Figure 26. Output from last iteration of optimization algorithm for 3dB coupler with C=15µm, T=6000µm, S=2.5µm, and λ=1.55µm

The plot of output power vs. linear coupling length for the structure described in Figure 26 is given in Figure 27.

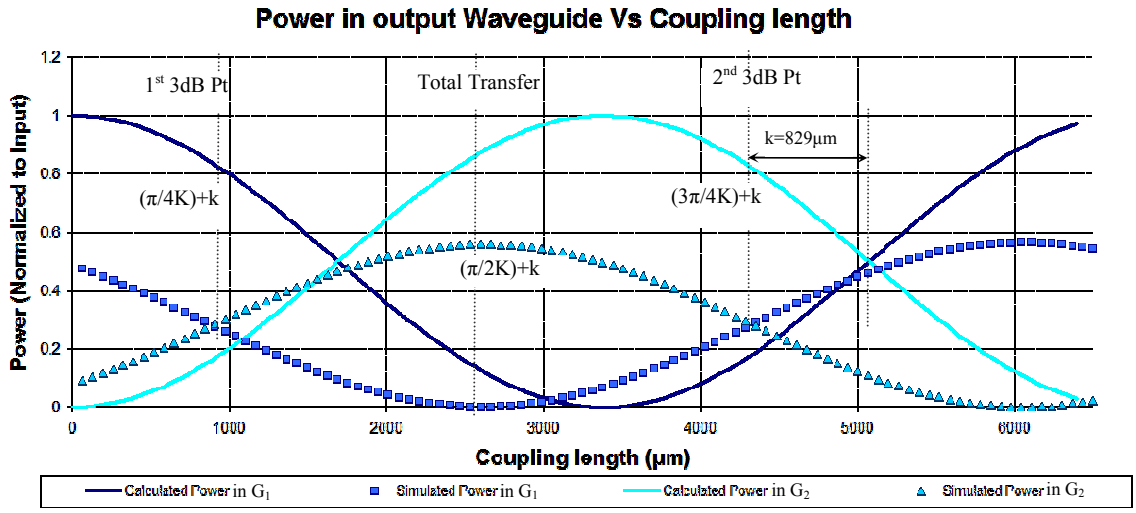

Figure 27. Output power vs coupling length for 3dB coupler with C=15µm, T=6000µm, and λ=1.55µm

The coupling period of (L_{per}=6897µm) and thus coupling coefficient (K=455) for this structure is nearly identical to the previous device as S=2.5µm. The increased separation of the output ports however allows for K to drop off more quickly within the bending region. This reduction in coupling has the effect of reducing the offset parameter k to 829µm of effective length. The 3dB length L_{3dB} for this structure thus must increase to 894.7µm to account for lower coupling in the bending region. Applying this new value for L and increasing the mesh parameters used the structure in Figure 28 is designed.

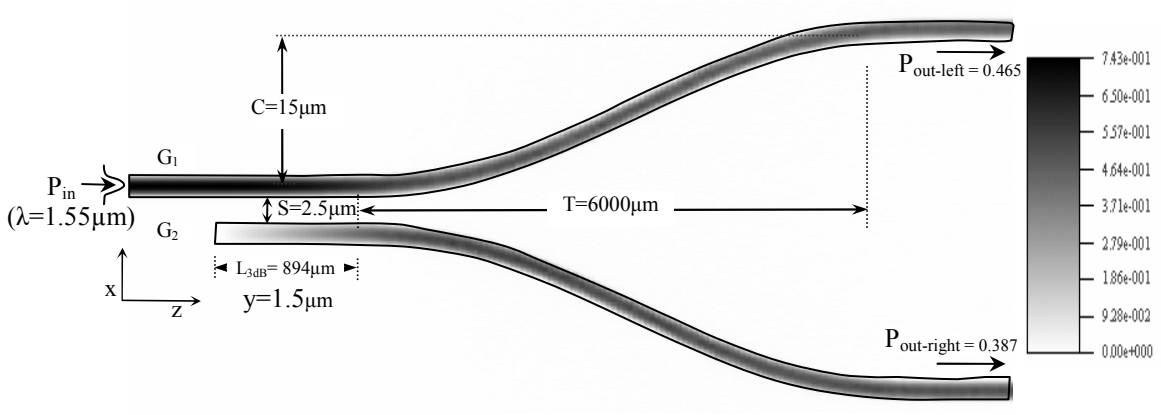

Figure 28. High mesh simulation of 3dB coupler with C=15µm, T=6000µm, and λ=1.55µm

It is apparent in this device that bending losses are considerably larger, at 14%, as a result of both the increased output port separation to 34.5µm and T=6000µm. The behavior of this device at other wavelengths is depicted in Table 4. The data shows similar trends in L_{3dB} and K as a function of the wavelength.

Table 4. Characteristics of 3dB coupler, C=15µm, T=6000µm

λ (µm)	K	L_{3dB} (µm)	Offset (k)	P_{out-G1}	P_{out-G2}	Total Loss (%)
1.55	455.441	894.7	829.777	0.465	0.387	14.8
1.49	427.746	985.7	850.433	0.465	0.401	13.4
1.31	351.716	1395	838.048	0.474	0.416	11
0.98	233.006	2543.2	827.520	0.477	0.421	10.2

In summary, the behavior of all these devices is well characterized. An overview of the acquired data is given in Figure 29 representing L_{3dB} as a function of wavelength in each structure. The parameter K for a particular structure is given by the slope of the corresponding curve at a point. The phase offset k that occurs as a result of the coupling in the bending region can be interpreted as a vertical offset in L upwards for a given

degrease in bend radius. It is clear that the wavelength dependence of K and k are not linear.

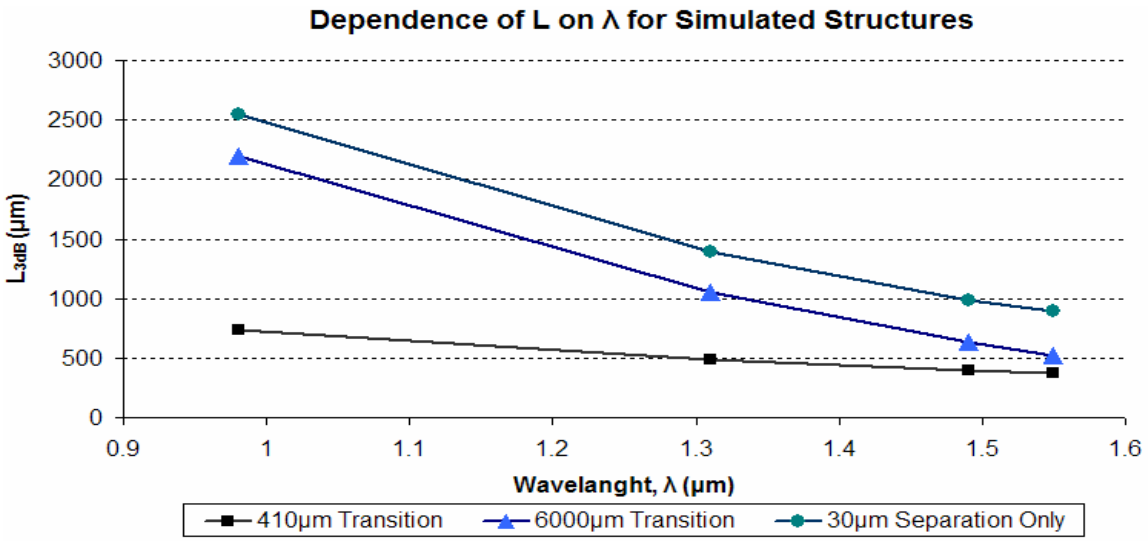

Figure 29. Plot of wavelength vs. coupling length for each structure

4.5 Wavelength Splitter

In the design of the 3dB splitter it became apparent that the coupling coefficient is dependent on wavelength. This property of a coupled-mode will be taken advantage of to design a structure with the ability to split an optical signal composed of two wavelengths (λ_1 and λ_2) into its components. This class of couplers are referred to as wavelength-division-multiplexers (WDM) couplers. Specific theory behind such as structure is considered in [67]. This device, referred to as a wavelength splitter, has a structure nearly identical to that of the 3dB coupler, a linear coupling region connected to two output ports by s-bends. When a signal is applied to the input of this type of coupler light will transfer back and forth several times between the adjacent waveguides in the coupling

region. Because the period of oscillation and thus coupling rate are slightly different at each wavelength of the input signal, a lag will arise between them. For every consecutive coupling period the offset between energy associated with each wavelength will increase by an integer multiple. Given the correct design a point can occur where the spatial offset in coupling between λ_1 and λ_2, is half the wavelength of λ_2, and thus each wavelength is isolated to a given branch of the coupler. By carefully choosing the waveguides to separate near this point, coupling will reduce, and each wavelength of the non-coherent input will be distributed to its respective output port. The diagram in Figure 30 depicts this type of coupler and how two arbitrary wavelengths may be split. The curves overlaid on the structure represent the location of power within the device for each wavelength.

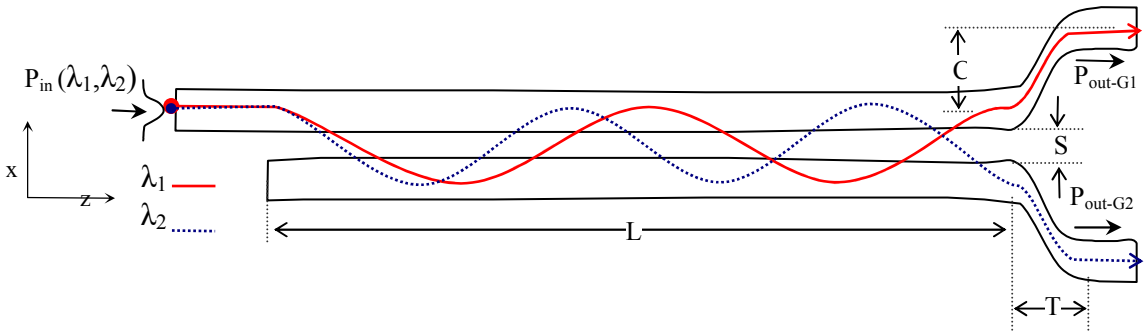

Figure 30. Operation of Ideal wavelength splitting structure

The coupling approach of separating the wavelengths of two coherent optical signal has the advantage of low loss; however requires a long coupling region. In most cases the wavelength splitter requires several coupling periods before the each wavelength can be isolated and as a result is generally much longer then the 3dB splitter, several millimeters. The number of coupling periods required is directly dependent on the difference between

the wavelengths to be split, as well as device geometry. For a given structure where $|L_{per-\lambda 1}-L_{per-\lambda 2}|<<L_{per-\lambda 1}$ more coupling periods are in generally required as $\lambda_1-\lambda_2$ decreases.

The design of the wavelength splitter will be accomplished with the use of the BPM. The process used to determine the best design for these structures will be slightly different from that of the 3dB splitter in order to better optimize device dimensions as well as reduce simulation time. By letting both coupling length and waveguide separation to be left as design variables both can be better controlled to stay within the limitations of fabrication. If the waveguide separation is too large it is feasible that the required coupling length will exceed specifications. It is important to choose the maximum waveguide separation, providing the largest room for tolerance, yet still limiting device length to a reasonable size (4mm<L<7mm). The trade off between these parameters is carefully considered for each device. A second change in design methodology is implemented to reduce the simulation time. The large coupling region required for the wavelength splitter and need to optimize a two dimensional problem makes a full iterative algorithm computationally impractical. In order to facilitate the design process a least squared regression is used to extract parameters K, and k from only a few variations of coupling length, rather than iterating over the entire device length as was done in the design of the 3dB splitter. Least squares is an optimization technique through which a best fit function, in this case a sinusoid with parameters A, K, and k as previously defined, is matched to a given set of data points by minimizing the sum of the squares of the ordinate differences also referred to as residuals [68]. The parameter s to be

minimized is shown by Equation (33) where y_i represents the amplitude of the output field simulated by the BPM for a given coupling length. The corresponding amplitude approximated by the sinusoidal fitting function is $f(z_i) \approx A\cos(Kz-Kk)$.

$$s = \sum_{i=1}^{n} (y_i - f(z_i))^2 \ . \qquad \textbf{(33)}$$

An iterative approach of varying the sinusoidal parameters is used, with the minimization of s acting as a measure of how well the parameters match the data set. In order to ensure a convergence to the global minima of s initial conditions for the sinusoidal parameters are chosen such that they are graphically close to a plot of the given simulation data points. This optimization is implemented in a Microsoft excel spreadsheet, where the data points from simulation are extracted and manipulated. The solve function in excel is used to minimize the parameters A, K, and k based on the imported data set for a given separation. This spreadsheet can be found on the documentation CD, which also contains simulation files, pictures, and results not presented in this thesis here. Once these parameters are found for different waveguide separations and wavelengths it is possible to reproduce the device behavior for any arbitrary coupling length, similar to the way the 3dB coupler results were used to reproduce its theoretical results. With this data it becomes a much simpler task to determine the optimal coupling length and waveguide separation at which wavelength splitting will occur.

There will be three structural variations of the wavelength splitter designed in this thesis, one with T=500μm and C=6μm, another with T=6000μm and C=6μm, and a final

variation with T=6000μm and larger output separation of C=15μm. These dimensions were chosen to maintain consistency with the 3dB splitter, as well as to provide a range of testable structures. At each of these dimensions the device will be designed to split the following combinations of input wavelengths, 1550nm-1310nm, 1490nm-1310nm, and 1550nm-980nm. These wavelengths are chosen to cover the range of widely used telecommunication frequencies where integrated λ splitters have potential application.

The use of the low mesh (x=10div/μm, y=10div/μm, and z-step=1μm) BPM, is used to simulate each of these structures, and obtain the power from each output branch for several variations of L and S. A script used to extract the output power for variations of L and S is given in Appendix C. Using the curve fitting technique described above the required design parameters K, and k are extracted. Ten to twenty points of simulation data over a coupling distance of a period or more were used so that the regression method could converge to within a sum of error, s, of less then 0.001. Typical convergence to this level of accuracy required no more then 100 iterations in excel. Table 5, Table 6, and Table 7 represent the acquired data for each of the three structures respectively.

Table 5. Coupling data for wavelength splitter T=500µm, C=6µm

Guide Separation (µm)	λ=1.55µm		λ=1.49µm		λ=1.31µm		λ=0.98µm	
	K	k (µm)	K	k (µm)	K	k (µm)	K	k (µm)
2	872.76	122.47	824.21	123.50	685.46	124.10	464.96	124.68
1.9	994.32	122.22	939.40	125.30	783.39	123.20	534.03	124.91
1.8	1133.89	120.38	1070.97	124.02	895.99	121.67	613.17	124.69
1.7	1291.24	119.24	1221.24	122.84	1023.95	120.20	704.37	124.30
1.6	1471.73	118.50	1393.97	119.78	1170.42	119.46	808.88	125.49
1.5	1676.56	118.77	1590.34	118.04	1338.90	118.25	929.07	124.38
1.4	1912.16	118.28	1814.37	117.44	1531.89	117.79	1067.07	123.60
1.3	2181.85	117.97	2070.58	116.59	1752.51	117.54	1225.85	122.09
1.2	2488.41	117.73	2362.95	116.30	2005.56	117.07	1410.13	120.71
1.1	2839.93	117.41	2698.85	116.12	2295.32	116.54	1621.47	119.87
1	3239.97	116.81	3083.59	116.17	2629.41	116.05	1865.03	118.94

Table 6. Coupling data for wavelength splitter T=6000µm, C=6µm

Guide Separation (µm)	λ=1.55µm		λ=1.49µm		λ=1.31µm		λ=0.98µm	
	K	k (µm)	K	k (µm)	K	k (µm)	K	k (µm)
2	874.04	1187.54	824.38	1185.86	684.28	1176.55	468.34	1131.98
1.9	994.25	1189.46	939.77	1183.68	783.18	1180.26	534.44	1156.64
1.8	1137.26	1178.29	1070.98	1184.84	895.78	1176.49	613.26	1157.39
1.7	1292.42	1183.94	1222.06	1178.88	1023.80	1170.96	704.16	1157.83
1.6	1472.54	1182.68	1394.08	1179.16	1170.91	1168.40	809.31	1153.54
1.5	1678.62	1180.83	1590.25	1174.89	1339.30	1166.71	929.55	1151.55
1.4	1909.47	1185.98	1814.46	1170.76	1531.89	1164.99	1067.93	1151.23
1.3	2182.86	1176.68	2070.76	1168.47	1752.62	1163.17	1227.24	1148.34
1.2	2488.48	1175.01	2363.69	1167.57	2005.68	1161.15	1410.49	1145.22
1.1	2838.77	1171.98	2699.06	1166.83	2296.05	1158.45	1621.73	1142.39
1	3240.92	1167.92	3083.42	1164.50	2629.39	1155.98	1865.31	1140.36

Table 7. Coupling data for wavelength splitter T=6000µm, C=15µm

Guide Separation (µm)	λ=1.55µm		λ=1.49µm		λ=1.31µm		λ=0.98µm	
	K	k (µm)	K	k (µm)	K	k (µm)	K	k (µm)
2	873.69	872.60	824.10	845.95	685.22	854.55	465.14	817.82
1.9	995.85	862.29	939.42	843.71	783.51	850.77	534.04	829.60
1.8	1133.85	863.37	1071.73	853.46	895.84	850.66	613.40	831.62
1.7	1292.99	866.05	1222.46	860.43	1024.00	849.81	704.43	826.80
1.6	1473.00	863.29	1394.07	863.30	1171.41	848.35	809.23	828.79
1.5	1678.38	862.21	1590.17	865.47	1339.74	846.76	929.62	839.39
1.4	1913.95	862.25	1814.47	864.79	1531.92	845.49	1067.86	839.96
1.3	2183.25	856.82	2070.62	858.74	1752.75	842.19	1227.37	837.16
1.2	2488.74	850.69	2363.73	855.53	2005.93	843.05	1410.47	833.85
1.1	2844.77	844.53	2699.35	851.28	2296.18	841.61	1621.42	830.24
1	3238.82	843.46	3083.23	853.71	2629.72	839.34	1865.23	828.08

Several patterns in K and k emerge as a result of the change in structure and wavelength. These patterns reinforce coupled-mode theory as well as observations made from 3dB coupler data. For a given structure, K will consistently decreases with increasing waveguide separation or decreasing wavelength. Between given structures only the dimensions of the bending region change, as such the coupling per unit length in the linear region, K, remains constant between structures for a specified wavelength and waveguide separation. There is a slight variation however that can be attributed to discretization error in BPM as well as convergence error in the leased squared regression. In contrast, k remains nearly constant with changing waveguide separation and wavelength, changing primarily with the dimensions of the bending region. For the first structure where the curve length and output port separation are both small, a minimum amount of coupling will occur, in the region resulting in k=120μm. An increase of the curve transition to 6000μm will dramatically increase this coupling as is seen by k=1175μm. In the final structure waveguide separation is increased to ~30μm, leading to a decrease in coupling that can occur in the bending region, represented by k=830μm. In addition it can be seen that this parameter k, does indeed change slightly with S and λ, as a result of the highly nonlinear nature of coupling.

Using the data from Table 5, to Table 7, K can be characterized as a function of the design parameter, S. The plot in Figure 31 depicts this relationship at each of the four wavelengths of interest. The dots represent the simulation results and the line an

exponential fit, to that data. The equation for the exponential fit is used to extrapolate K over a continuous range of waveguide separations.

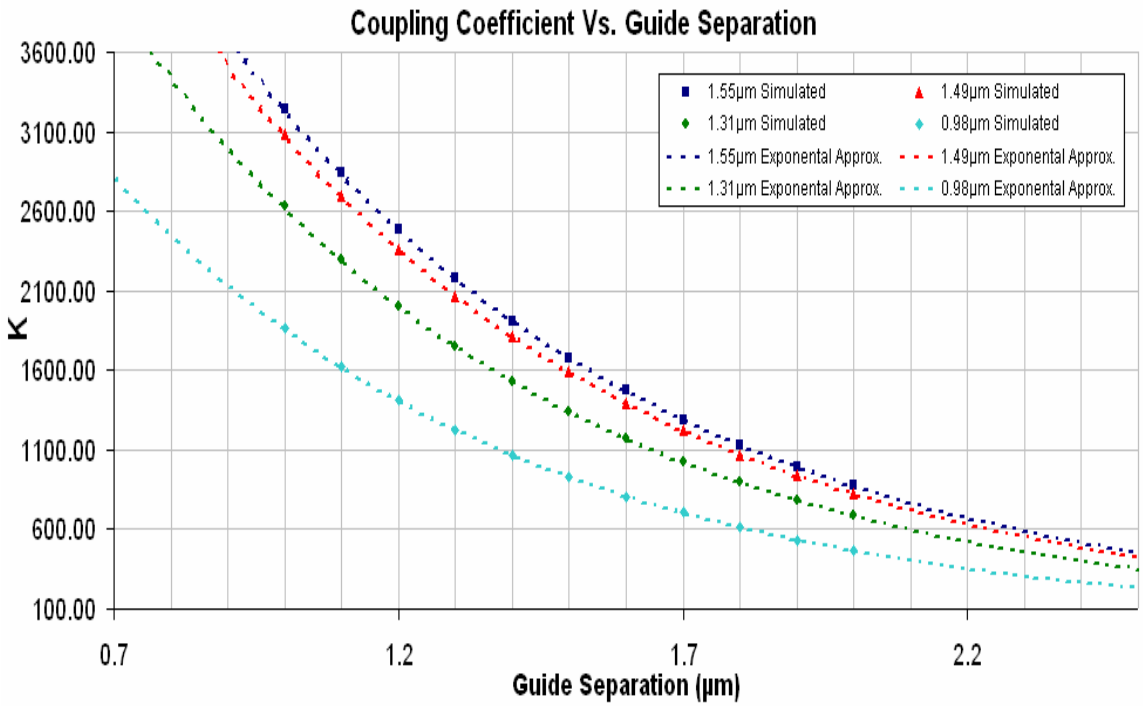

Figure 31. Waveguide separation vs. coupling coefficient, for C=6µm, T=500µm

The exponential decrease in coupling that is observed as the waveguides are separated is a result of the decaying behavior of the evanescent field into the cladding. With this data design becomes a matter of choosing a waveguide separation with a corresponding coupling coefficient which can provide splitting of the two desired wavelengths within 3 to 5 millimeters. Using mathematics software such as MathCAD, it is easy to arbitrarily change design parameters such as waveguide separation on the fly, and plot the corresponding cosine wave from which the required coupling length can be visually

extracted. To achieve similar results using the BPM would take several hours of computation time.

In the first design where T=500µm, C=6µm, with input wavelengths of 1.55µm and 1.31µm an optimal waveguide separation of S=1.5µm is used. This value of separation conforms to fabrication limitations and yields a splitting length of L=4569µm. The resulting output power characteristic over the first 8000µm of coupling length of G_1 is given in Figure 32. The splitting point is easily determined by where a π phase shift occurs between each cosine, as indicated by the dashed line.

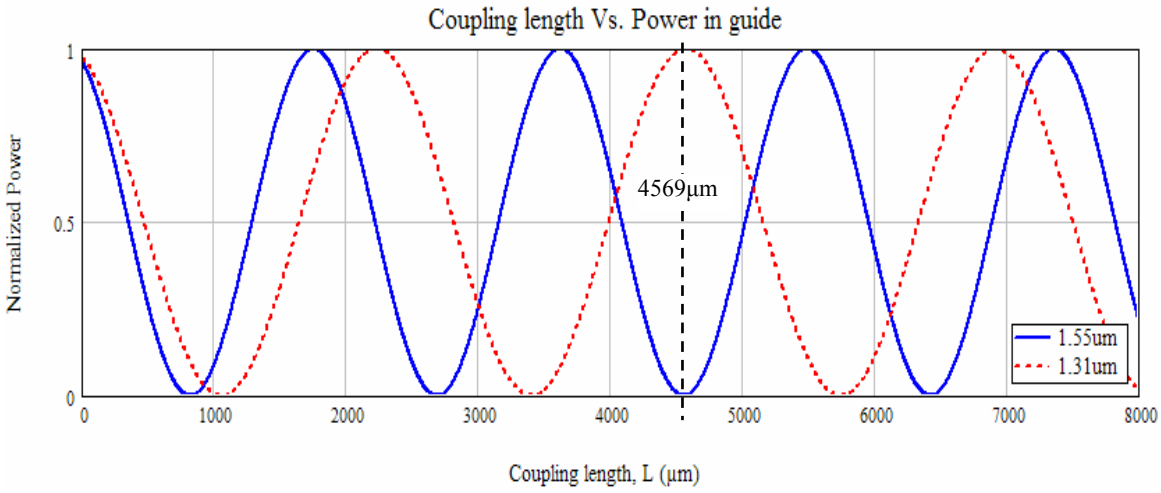

Figure 32. Output characteristic, C=6µm, T=500µm for λ=1.55µm and 1.31µm

Once the appropriate coupling length is determined for the given structure, the optibpm simulator is used to reproduce designed device behavior with a higher mesh (x=30pt/µm, y=10pt/µm, z=0.1µm step). Doing this for the structure considered above yields the intensity distribution shown in Figure 33.

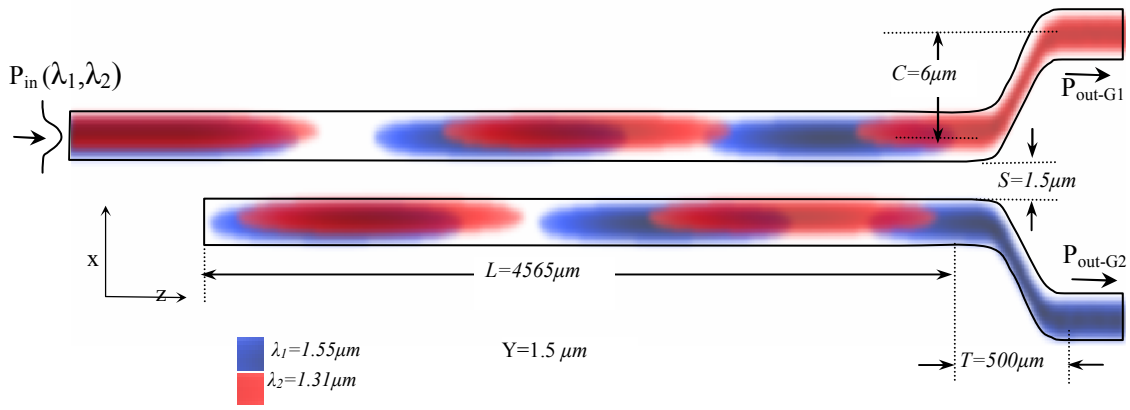

Figure 33. Intensity distribution in wavelength splitter T=500μm, C=6μm

Each wavelength in Figure 33 is represented by a different color, making the splitting behavior evident. The same design procedure can be repeated for each structure of interest, by adjusting the phase parameter k, for the given output curve. Table 8 gives the design parameters (S and L) as well as simulated and calculated output power for each structure considered. The calculated column represents the output intensity as measured from the MathCad plot, as such does not take into account propagation or bending losses ($P_{out\text{-}G1,\lambda1}+P_{out\text{-}G2,\lambda1}=1$, $P_{out\text{-}G1,\lambda2}+P_{out\text{-}G2,\lambda2}=1$). The calculated data shows that each of these designs will not perfectly split the two wavelengths. These inaccuracies are rooted in the fact that the phase offset between two given wavelengths increases by discreet amounts after each coupling length, and will not necessarily coincide with a fraction of π. Another major source of this intrinsic error is due to the visual method used in obtaining the separation length. The simulated data is obtained from the high resolution BPM. Power values for each wavelength in this case will not sum to 1 as a result of losses. The loss

incurred at each wavelength is also included. Similar trends in bending losses to the 3dB coupler are observed, with larger bends corresponding to higher losses.

Table 8. Design parameters, and output power for wavelength splitters

				Calulated				Simulated					
Structure Parameter	λ_1:λ_2 (nm)	S (μm)	L (μm)	$P_{out-G1,\lambda1}$	$P_{out-G1,\lambda2}$	$P_{out-G2,\lambda1}$	$P_{out-G2,\lambda2}$	$P_{out-G1,\lambda1}$	$P_{out-G1,\lambda2}$	$P_{out-G2,\lambda1}$	$P_{out-G2,\lambda2}$	Loss λ_1	% Loss λ_2
T=500μm C=6μm	1550:1310	1.5	4569	2.86E-05	1.00E+00	1.00E+00	5.52E-05	6.44E-03	9.82E-01	9.61E-01	2.20E-03	3.29	1.60
	1490:1310	1.1	3995	9.91E-03	1.00E+00	9.90E-01	1.57E-04	5.61E-03	9.80E-01	9.72E-01	3.17E-03	2.26	1.65
	1550:980	1.4	5690	1.20E-02	9.95E-01	9.88E-01	4.72E-03	3.28E-02	9.70E-01	9.35E-01	4.91E-03	3.18	2.55
T=6000μm C=6μm	1550:1310	1.5	3523	1.76E-03	1.00E+00	9.98E-01	5.09E-06	1.58E-02	9.41E-01	8.82E-01	3.70E-03	10.21	5.51
	1490:1310	1.1	2933	4.91E-03	9.99E-01	9.95E-01	9.36E-04	7.35E-03	9.40E-01	9.22E-01	3.68E-03	7.10	5.60
	1550:980	1.1	2713	1.09E-03	9.99E-01	9.99E-01	9.47E-04	3.75E-03	9.39E-01	9.20E-01	4.11E-03	7.60	5.71
T=6000μm C=15μm	1550:1310	1.5	3838	1.33E-03	1.00E+00	9.99E-01	4.66E-05	9.86E-03	8.90E-01	8.45E-01	2.74E-03	14.55	10.71
	1490:1310	1.1	3247	4.50E-03	9.99E-01	9.96E-01	1.34E-03	3.34E-03	8.88E-01	8.58E-01	4.91E-03	13.91	10.68
	1550:980	1.4	4962	1.70E-02	9.92E-01	9.83E-01	7.64E-03	4.08E-02	8.94E-01	8.14E-01	4.90E-03	14.49	10.07

In summary it is seen that this method yields an accurate and efficient way of computing the required design parameters for a given type of wavelength splitter. The error in splitting is minimal, and the regression method can map to the simulated data to sinusoidal theory with errors of well under 1%, which can decrease depending on how many data points are used to map to. The greatest power of the method is that it can be expanded for coupling regions with arbitrary lengths, without considerably changing the computation time. It is also possible to accurately extract these parameters for very few simulated values of output power in each waveguide (3 or 4 points) as long as the approximant period, amplitude and phase are known. Because data is being collected over a range of separations, once the parameter for the first case are found they can be used as the initial values for the next case, which only differs slightly insuring convergence. The regression method is effective because coupling behavior can be always represented by a sinusoid with a given frequency, amplitude, and phase shift.

4.6 MMI 3dB splitter

The final structure considered will be a 3dB splitter based on MMI. As described in the background section a field propagating in a multimode waveguide will interfere to create mirrored signal and multiple images of itself at various propagation lengths [69]. A correctly designed structure can split such an input signal with this method. A diagram of an MMI structure in a power splitting configuration is given in Figure 34. Like other power splitters it consists of a single input and two outputs. Connecting the input and outputs however is the multimode interface region designed in such a way that light interferes in the regions to create two images at its opposite end. At these image points are depicted the two output waveguides into which the light will couple.

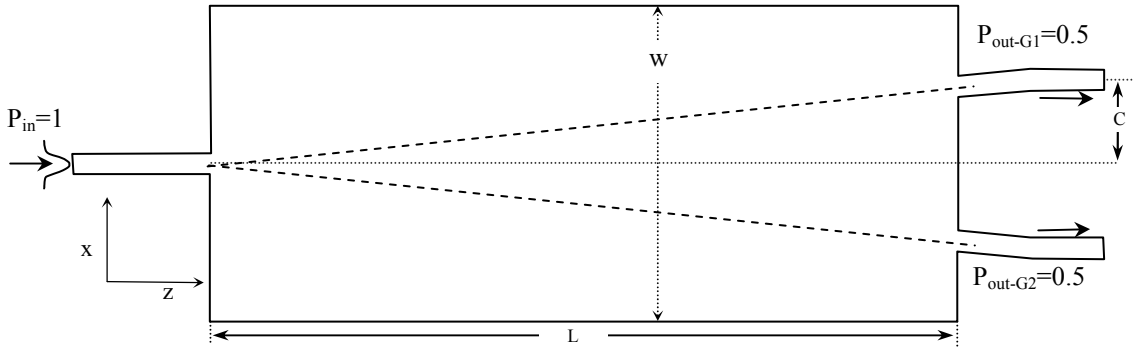

Figure 34. Ideal MMI Power splitting configuration

The use of the MMI to split an optical signal has several advantages such as relatively small dimensions (200 to 500μm), large fabrication tolerance as compared to the directional coupler (+/-0.5μm for 1dB change in output), low loss (0.7dB), and high bandwidth (100nm) [69][70][53][56]. Although not discussed here, wavelength dependent MMI structures can be designed for multiplexing applications. The Arrayed

Waveguide Grating (AWG) is one such device that relies on MMI, or a star coupler to split light into various wavelength channels.

With the use of the BPM two rib waveguide MMI structures that operate at λ=1.55μm will be designed to conform to the rib SOI platform. These structures will have w=20μm, and 30μm respectively, with output waveguide location, and L determined through the design process. These different values of w were chosen so that two different output waveguide separations can be obtained for testing purposes. In order to attain an approximate MMI length as a starting point for simulation the equation $L=3L_{\pi}/4N$ given by self imaging theory is used, where the beat length $L_{\pi}=(4nw^2)/(3\lambda)$. For the first structure where w=20μm, L_{π} is calculated to be 1176.77μm given a wavelength of 1.55μm, and effective-index (n=3.42) approximated by the effective-index of the single mode waveguide. Based on this value of L_{π}, L is calculated to be 441.29μm. In order to obtain the precise x-z location of the imaged fields the BPM is use. A slightly larger L (600μm) is used to observe the field profile around the splitting points as seen in Figure 35. It is found that splitting occurs at L=489.26, with variation from the calculated value attributed to differences in the modal index, in the single mode case, as well as simplifications made to the imaged equations. The vertical offset location is +/- 5.31μm.

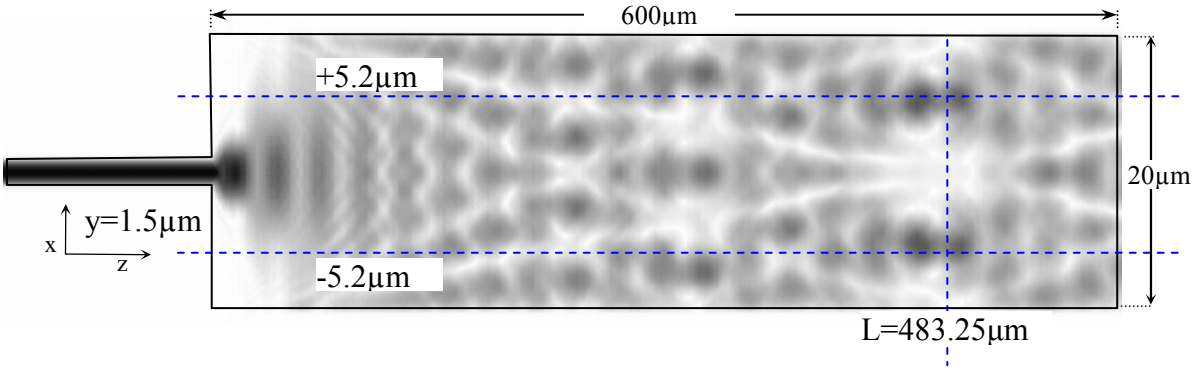

Figure 35. Field distribution in multimode region w=20µm, λ=1.55µm

The output ports are defined by inserting single mode waveguides that coincide with the coordinates of the output image points determined from Figure 35. A diagram of the final device design is shown in Figure 36. The symmetric nature of the device like the y-splitter will ensure near equal light intensities in each output waveguide however the efficiency of the structure is dependent on how accurately the output waveguides are placed. In this case where a visual analysis of the simulation results is used for optimization, an output power of approximately 0.41 is found in each waveguide, yielding losses of 18%.

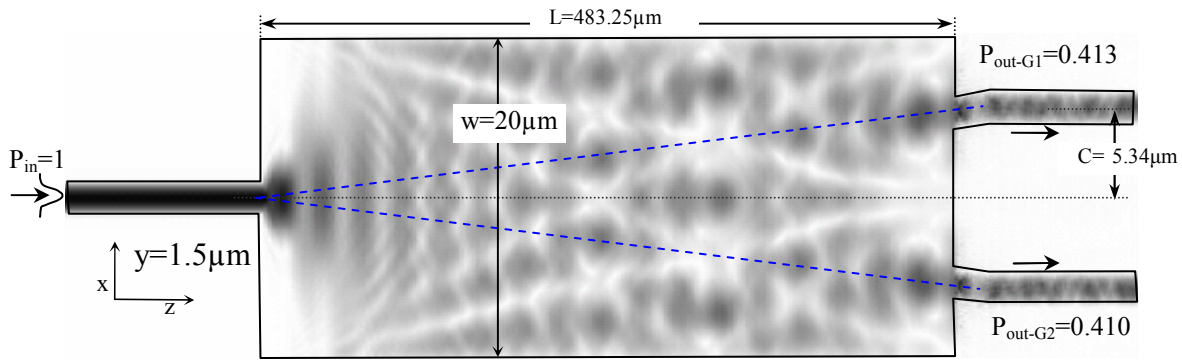

Figure 36. Field distribution in MMI design w=20µm, λ=1.55µm

The above design procedure is repeated for the structure with MMI width of 30μm. For this structure the optimal dimensions of L=1026μm and S=8.4μm, were determined. The structure has with output power in 0.3328 in each G_1 and G_2, or losses of 33%. These higher losses as compared to the smaller structure are attributed to error introduced in the manual optimization process.

In summary the MMI structure has the advantage of being able to achieve highly symmetric splitting. The nature of the structure, like the y-splitter, insures an equal optical intensity in the output of each branch. Unlike the y-splitter however the MMI structure is wavelength dependent, and the quality of the splitting extremely sensitive to and device tolerance. The sensitivity to design method used made losses in the MMI splitter much larger then either the directional coupler, or y-splitter. Improvements to the design in the future could include a taper near the region where the output ports connect to the multimode region. A larger width at this point would reduce the sensitivity of design to the placement of the output port.

4.7 Summary

In this section the design processes for several passive micro-optic structures are developed, the devices are optimized and simulation results provided. The loss comparison between structures reveled that directional couplers are the most versatile and efficient couplers. However, they are sensitive to variation in dimensions and their

operation is wavelength dependent. It is this wavelength dependence that is used to develop the wavelength selective splitter. This process is accomplished through an iterative simulation with a least squared regression used to extract critical design parameters. A y-branch is also considered which provides more reliable spitting however, has more then 10 times the losses of the directional coupler. The final structure considered is the MMI, which is found to have higher losses then the y-branch, but less then the coupling structure.

Chapter 5: Fabrication of Waveguide Devices

The fabrication of devices designed in this thesis is accomplished at the Rochester Institute of Technology (RIT) Semiconductor and Microsystems Fabrication Lab

(SMFL). This chapter will describe the more than ten process steps from mask making to silicon etching required to realize these waveguide devices. Additional emphasis will be placed on the problems encountered throughout the fabrication process, their impact on device operation, and ways in which these problems can be solved in the future. It should be noted that the structures incorporated into this layout are a revision of the design that was not fully optimized. During the fabrication period additional work was done to further improve device design (primarily increasing the meshing density), these changes could not be incorporated in to the fabricated device as the masks had already been made by the time the improvements were determined. It was decided that the optimal designs would be presented in this thesis as they are a considerable improvement, over the fabricated structures. As such the optimal structures given in the design section of this thesis may differ in dimensions from the fabricated structures by +/-0.1μm for waveguide separation and or +/- 100μm of coupling length. Other then these slight changes in coupling parameters ever aspect of the devices remain the same such as type and size of bending region as well. The changes present no alteration in fabrication process or fundamental change in device behavior.

5.1 Design layout and mask making

The first step, prior fabrication, is to design a layout for the signal lithography mask required. The mask used in this process defines the shape and location of each guiding rib structure in the x-z plane of the die. In order to ensure that the layout of each structure conforms to the design constraints determined through simulation, each individual

structure is exported from Optiwave to the standard Graphical data systems (GDSII) layout format [71]. Each GDS file is then imported into a VLSI layout software tool (IC was used). Within this tool each structure or cell is positioned, and a label applied for easy identification after fabrication. The entire size of the layout is made to be 18.5x18.5mm, to stay within fabrication limits (20x20mm) of the MEBES III mask making tool and to provide sufficient spatial tolerance around the outer edge of each die. A diagram of the full layout is given in Figure 37, with critical dimensions labeled in red.

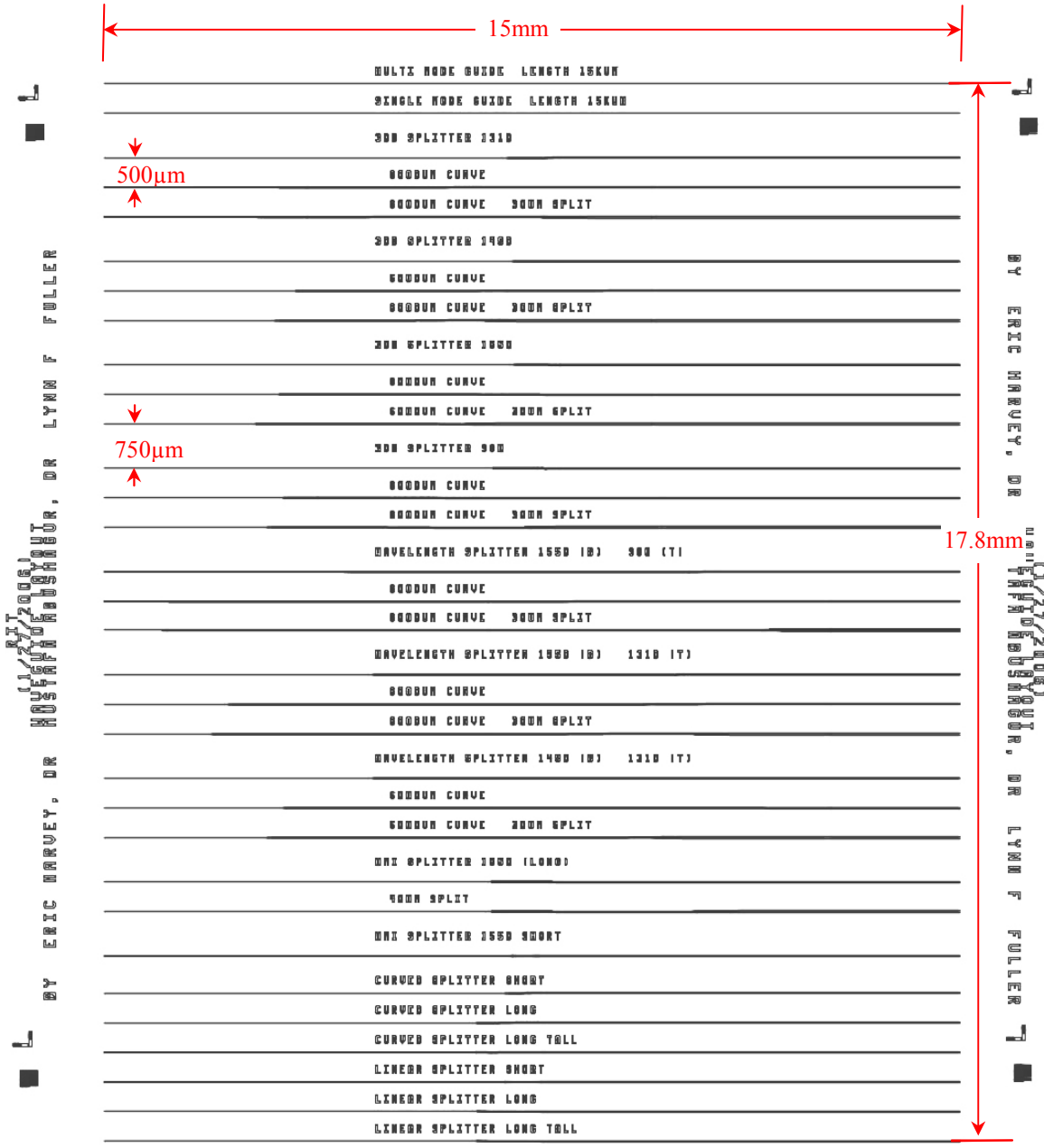

Figure 37. Mask layout of waveguide die

Unlike the individual designs, each of the structures in the overall layout is made to be 15mm long by appending leading and trailing waveguides to the input and output ports.

This is done to ensure that all input and output ports are at the same respective z-coordinate regardless of the original design length. By having the structures inline all devices can be tested on the same edge of the die rather then having to prepare separate interface facets for each structure. The functional implications of extending each device are minimal; the primary impact being increased losses. A separation between devices of at least 500μm is chosen as it ensures negligible interaction of an excited waveguide's evanescent field with the adjacent structure.

Once the layout in Figure 37 is generated it is again exported to a GDS II file from which the MEBES III can directly print the mask. The mask type is designed to be clear field meaning that the chrome on the mask plate is removed by the MEBES everywhere other then where a rib structure and identifying text is located. This design is chosen based on the nature of the positive photo resist that will be used. Positive resist becomes chemically soluble only where exposed to light in the stepper. The MEBES is also set to use a low fracture resolution 0.3μm at 5x, in order to ensure that the curved structure which exists in many of the devices is accurately depicted on the mask. The 5x mask with 0.3μm resolution can print a pattern with 0.06μm resolution. A picture of the fabricated mask is given in Figure 38.

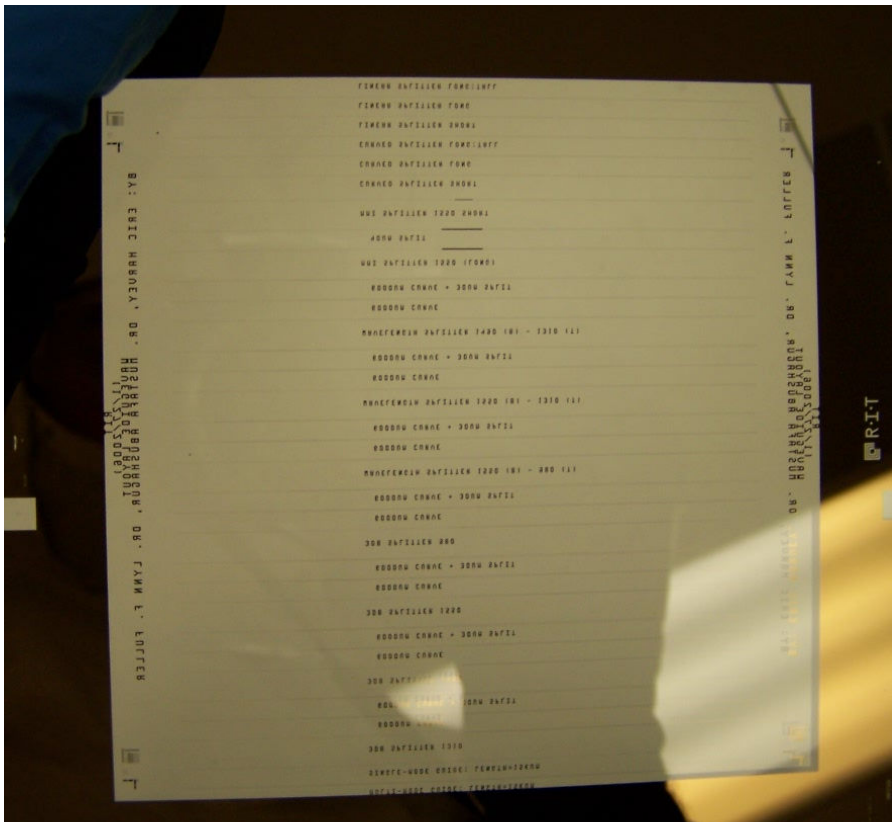

Figure 38. Fabricated Mask

5.2 Processing

The following process steps were designed to realize the mask layout as a rib waveguide structure on an SOI substrate. These steps are designed to address several key issues encountered by using reactive ions etch as the method of forming the rib. These issues include applying a blocking hard mask to prevent the silicon from etching in unwanted regions, reducing back reflections from the hard mask, and removing the hard mask after etch. The following will describe the steps used to fabricate these waveguide devices.

5.2.1 Wafer Preparation

The starting SOI substrate for this process is an Ultrasil 150mm (6in) diameter wafer with 1.09µm+/-5% BOX (buried oxide layer) and a 2.2µm +/- 0.5µm device layer at 1-0-0 lattice orientation. A labeled diagram of the wafer cross section is given in Figure 39.

Figure 39. Starting wafer substrate

There are two primary methods, SIMOX and Smart Cut^{tm} through which the SOI platform is made. SIMOX or Separation by Implantation of Oxygen uses oxygen ion beam implantation and high temperature annealing to allow the oxygen ions to interact with the host SI to create a BOX layer [72] [73]. The SIMOX process has high uniformity. However the BOX thickness is limited by the implant voltage. A 200kev field would result in approximately 400nm of oxide formation. The other primary method through which a SOI substrates are formed is Smart Cut, a technique that uses implantation of hydrogen and annealing along with direct wafer bonding. The method provides a high uniformity device layer, and a better oxide layer through thermal oxidation. [73]. Additional wafer bonding methods are also used in SOI fabrication, such as Epitaxial layer transfer (ELTRAN) and Bond and back etch (BESOI) [73]. The particular method used for the Ultrasil wafer is a form of BE using fusion bonding [74].

In this method a thermally oxidized wafer or a handle wafer (in this case 675μm thick) is fused to pure silicon, or donor wafer. The donor wafer is then carefully cleaved or thinned to achieve the required device layer thickness [75]. Fusion bonding refers to the method by which two highly polished wafers will adhere to each other at room temperature simply by being pushed together. This processing method is advantageous because it can achieve a relatively thick device and oxide layers needed in optoelectronics and MEMS applications. This wafer was chosen primarily for the thickness of its device layer, which is critical to the operation of the waveguide coupler. The implications of tolerance in the device layer and its impact on coupler performance will be examined at the end of this section. The BOX layer is slightly thinner then desired, due to limited by availability.

5.2.2 Aluminum deposition

The first process step is the deposition of 0.1μm of aluminum. This thin layer of aluminum will serve as a hard mask to protect silicon in areas where the rib structure is to be formed. A protecting layer is necessary as photo resist etches at a similar rate as photo resist, in a reactive ion etcher. Typical resist films are approximately 9000Å thick; because the target etch depth for this process is 8000 Å, little to no resist would remain after the etch, leaving little room for tolerance. Another reason why resist is a poor masking material is because of its low melting point, which can allow it to soften when near the RF (radio frequency) plasma formed by the RIE (reactive ion etch) tool. It is possible for soft resist to deform or even flow during the silicon etch distorting the

underlying structure. Aluminum was chosen for its sufficiently high melting point and resistance to the RIE plasma. Because aluminum is so resistant to the silicon etch 0.1μm is more then adequate to protect the underlying device layer. The thickness of the layer is chosen to be as thin as possible to reduce over etching caused by anisotropic hot phosphoric etch used to remove the aluminum layer. To deposit the aluminum the CVC601 sputtering tool, as seen in Figure 40 is used.

Figure 40. CVC601

DC sputtering is accomplished by flowing Argon through a vacuum chamber containing a target (material which is to be sputtered) and the substrate (surface to be coated in this case the wafer). By applying a large voltage to the target material the argon will ionize. The Ar^+ ions will be attracted to the target. As they collide atoms of the target will break off, coating the nearby substrate. A high vacuum inside the chamber is imperative to minimize the number of collisions the target atoms incur with air molecules [76].

For this specific coating the CVC tool is pumped down to a pressure of $1.4*10^{-5}$ Torr, taking approximately 1.5hr. Prior to sputtering a radiant heating of the wafer is preformed, to help improve how well the aluminum atoms will adhere to the silicon as well as reduce surface stress in the aluminum layer. The sputtering itself was done with a flow of 5.1mTorr of argon, sputter power of 2000watts, and sputter time of 200sec as determined from past sputter rates. The specific target used during sputtering has 1% silicon, as it is important to adherence particularly in transistor fabrication, and is used in this case since a pure aluminum target was not available. The measured deposition thickness with the Tancor P2 Proflometer is 0.1162µm. A diagram showing the expected cross section of the wafer after the completion of aluminum deposition is given in Figure 41.

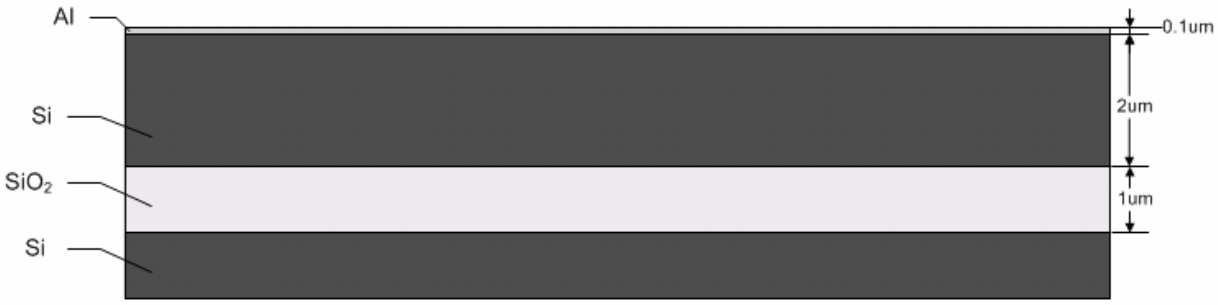

Figure 41. Wafer cross section after Aluminum deposition

5.2.3 Bottom Anti Reflection Coating (BARC) Deposition

The aluminum deposited in the previous step produces a mirror like finish on the wafer. Prior to performing any lithography on this surface an Anti reflection coating (ARC)

must be applied to eliminate effects such as reflective notching and standing waves in the resist [77]. The BARC in particular will help to improve side wall roughness of the waveguide, and ensure a uniform rib profile. The BARC used is the XLT-20 with refractive index of 1.74 which works with an i-line stepper (365nm) [78]. The BARC is spun on at 4000RPM for 60sec, to obtain a thickenss of 2100Å. The CEE Spinner used is given in Figure 42.

Figure 42. CEE spin coater

There is a two stage post bake, the first is for 60s at 100°C, and the second is for 60s at 168°C. This particular BARC is designed to be dissolved along with the resist after develop eliminating the need for any extra processing steps. A diagram of the cross section after this process step is given in Figure 43.

Figure 43. Wafer cross section after spin on of BARK

5.2.4 Resist Coating

After the surface has been prepared for lithography, a photo resist is applied. This photosensitive material changes properties when exposed to light, much like photographic paper. Resist is the martial which captures the pattern from the mask during lithography. The specific resist used is Arch OIR 620, and is applied using the automated SSI coat and develop track seen in Figure 44.

Figure 44. SSI track

The NOHMDS recipe is used on this track, as vapor prime is not necessary when using an underlying BARC which resist can adhere well to. The OIR 620 resist is spun on at 4150RPM for 30s yielding a thickness of 9200Å with 5% uniformity [79]. A post bake at 140°C and 60s is done to harden the resist. The exact recipe is given in [79]. A diagram depicting the cross section of the wafer following this step is given in Figure 45.

Figure 45. Wafer cross section after spin on of photo resist

5.2.5 Lithography

The Lithography step, arguably the most important, has the purpose of transferring the layout from the mask on to the wafer. This is accomplished by shining light through the mask; where no chrome exists light will pass through changing the chemical properties of the underlying resist. The pattering of the wafer for this process is accomplished with an i-line cannon stepper (FPA 2000-i1), with resolution of 0.5μm, NA = 0.52, and depth of focus = 0.8μm. A picture of the cannon stepper is given in Figure 46.

Figure 46. Cannon FPA 2000-il

In order to correctly transfer the pattern from the mask onto the wafer, the die size, spacing between adjacent die, and number of shots, or replications of the mask pattern to be made on the wafer must be set. These parameters are defined by variables in three key files associated with stepper job (shot file, process file, and layout file). The die size is given by setting the position of blades that effectively limit the area of the mask that is illuminated. The variables B_L, B_r, B_u , and B_d represent the respective positions of the left, right, up, and down blades in a Cartesian Coordinate System with the center of the mask laying at the origin. Based on the 18.5x18.5mm dimensions of the design, the corresponding blade positions are set B_L=-9.25mm B_r=9.25mm B_u=9.25mm B_d=-9.25mm. The spacing between die is given by the relationship of the step size to the die size. The step variables $Step_x$ and $Step_y$ define the distance from a given point on one die

to the same point on an adjacent die in the respective direction. In this case both $Step_x$ and $Step_y$ are set to 19mm, providing 500µm or space between each die on all sides. This was chosen to ensure sufficient room for wafer dicing later on in the process. Based on these dimensions the Cannon stepper determines automatically the maximum number shots on the wafer is 7x7. A diagram depicting these key layout parameters as well as position of each die on the wafer is given in Figure 47.

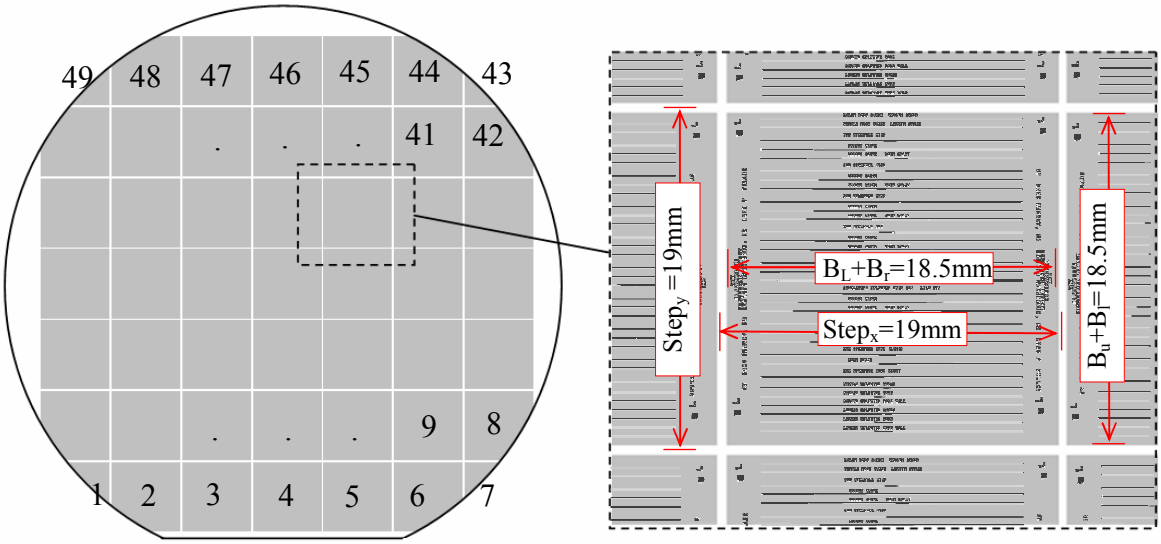

Figure 47. Die layout on wafer

Once the correct layout is defined within the stepper process files, an optimal exposure and focus must be determined. This is accomplished by performing a focus exposure matrix, a specific execution of a stepper job in which the focus is varied between each row, and exposure between each column. The focus exposure matrix is preformed on a test wafer just prior to the patterning of the device waver to minimize sources of variation. The optimal values for the device wafer of 0.1µm focus, and 252mj/cm^2 of exposure were chosen by examining the focus exposure matrix to find the die with the

most accurate lines and spaces obtained with a given develop recipe, as compared to the designed dimensions. A diagram depicting the cross section of the wafer in the region of a single mode waveguide during lithography is shown in Figure 48.

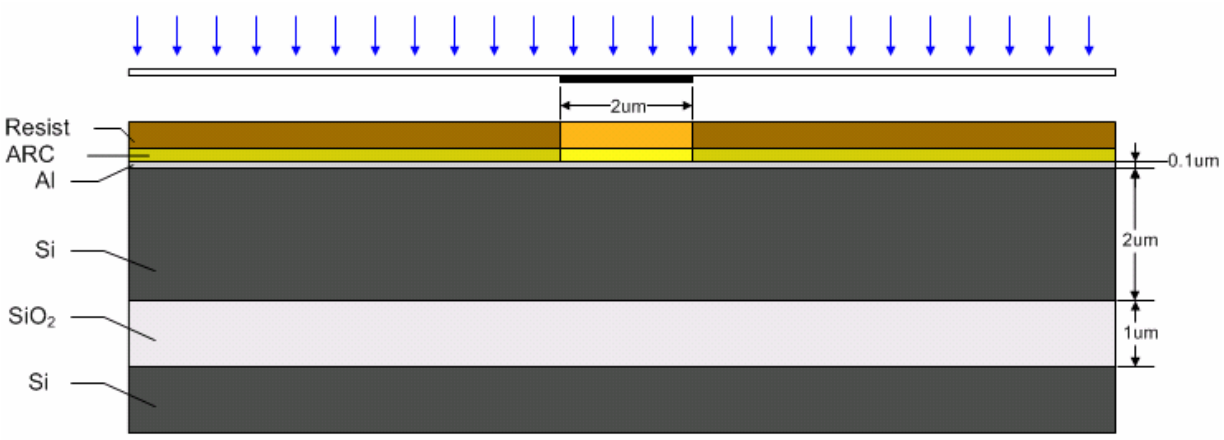

Figure 48. Wafer cross section during lithography step

5.2.6 Develop resist

After the pattering of the wafer, the resist which was exposed to light, can be chemically removed using a photo developer. The develop process is accomplished by running the DEVELIP recipe, on the SSI track seen in Figure 44. The particular recipe involves spraying developer (CD-26) on the spinning wafer for two minutes followed by a two minute post bake at 120°C, the exact recipe is found in [80]. The cross section of the wafer after the developing process is seen in Figure 49. The ARC will be removed along with the resist as it is soluble to developer.

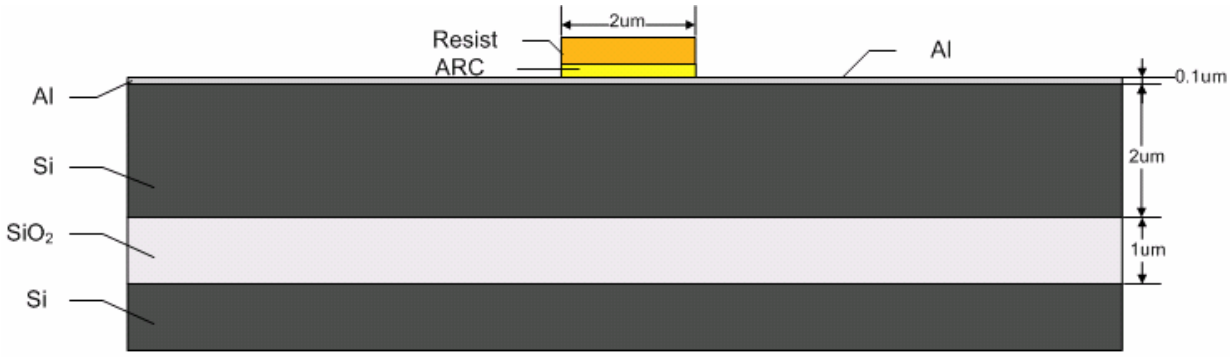

Figure 49. Wafer cross section after develop step

5.2.7 Aluminum etch

The next step is to remove the protective aluminum layer not covered by photo resist, so that the underlying silicon is exposed for etching of the rib structure. The Al is removed using phosphoric acid at 50°C. An etch time of 22 seconds is used as it was determined to be the minimum time required to clear the aluminum. It is critical that the etch time is as short as possible to minimize over etching, which can effect waveguide dimensions. During the etching the wafer is slowly agitated to improve uniformity by remove air bubbles that may exist between the waveguide patterns. A picture of the aluminum etch bench used is seen in Figure 50.

Figure 50. Aluminum Etch bench

Immediately following the aluminum etch, the wafer is submerged in deionized (DI) water to prevent further etching. A Spin Rinse Dry (SRD) is preformed to ensure the removal of acid and other particles from the surface of the wafer. The SRD tool washes the wafer with warm DI water for several minutes, and then dries it with nitrogen. The diagram in Figure 51 shows the cross section of the wafer, after the aluminum etch.

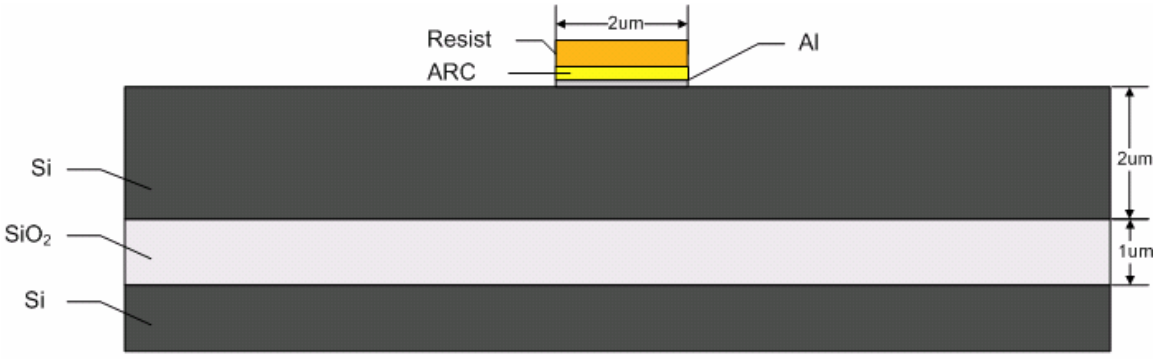

Figure 51. Cross section of wafer after Aluminum etch

5.2.8 Plasma etch of resist

To ensure the resist remaining on top of the waveguides does not soften and flow onto unwanted portions of the wafer during the SI etch it is removed by means of a oxygen ash. The hard ash recipe on the Branson L3200 Asher is used, as seen in Figure 52. The hard ash is fixed length plasma etch used to remove undeveloped or hardened resist. The oxygen plasma will etch any organic layer, including the ARC, leaving behind only the masking Al layer.

Figure 52. Branson L3200 Asher

A diagram of the wafer cross section after the resist and ARC has been removed can be seen in Figure 53.

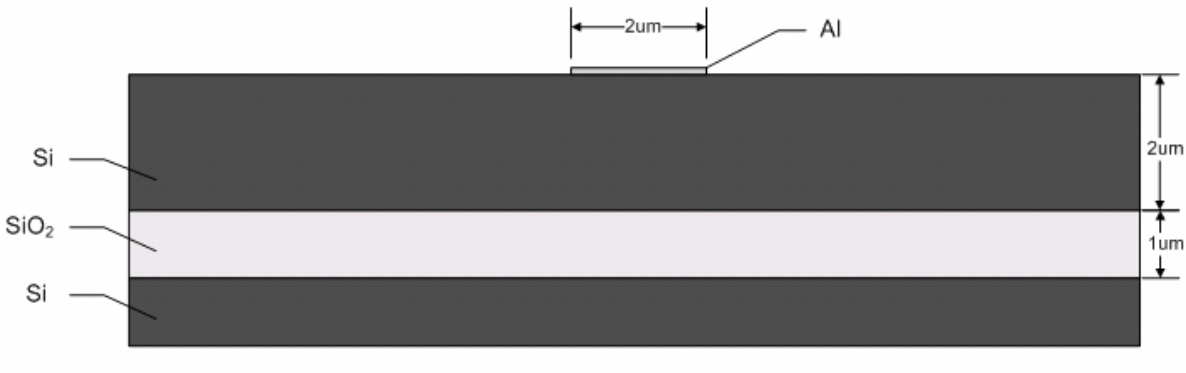

Figure 53. Wafer cross section after removal of resist and BARC

5.2.9 Silicon etch

The rib waveguide structure is formed by etching away 0.8μm of silicon from areas not protected by the Al hard mask. The Drytek Quad RIE tool is used because it can etch SI with high anisotropy (vertical side walls), which is desirable for the rib waveguide. The REI tool consists of a vacuum chamber in which gasses are flowed. A large RF electric field applied to the chamber ionizes the gas molecules by striping them of electrons, resulting in plasma. As the wafer is DC isolated, and the walls of the chamber are grounded electrons will build up on the on wafer allowing it to develop a large negative voltage. The positive ions of the plasma will be attracted to the surface of the wafer. As the plasma collides with the surface of the wafer it will react chemically and physically to etch the material. It is the high electric field that forms between the wafer and the etching plasma that allows the RIE to be etch primarily downwards [81]. A major drawback to RIE tool is the rough sidewalls it produces, a large source of losses in waveguide structures. A picture of the Drytek Quad used in this process is given in Figure 54.

Figure 54. Drytek quad RIE tool

The specific etch recipe flows 30 sccm of CHF3, 30sccm SF6 in chamber 2. The applied RF power is 200W, and the chamber pressure is maintained at 40mTorr. Using several test wafers this process was characterized, and a measured etch rate of approximately 1028Å/min is obtained. It is observed however that there is a wide range of etch rates dependent on location on the wafer measured. The center of the wafer experiences a shallow etch depth and the edges of the wafer, a deep etch depth. Based on measurements a etch time of 7.5min is chosen for the device wafer, with a measured mean etch depth of 0.77μm at a point midway between the center and edge of the wafer. A diagram of the expected wafer cross section after the silicon etch is given in Figure 55.

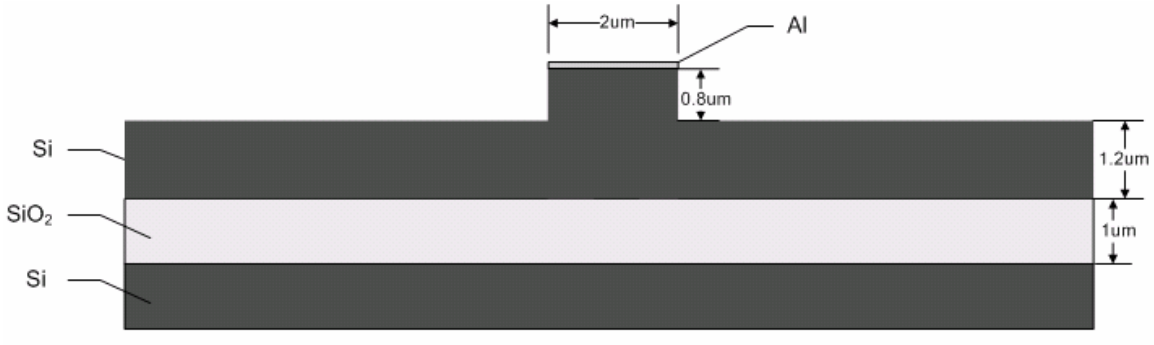

Figure 55. Wafer cross section after Silicon etch

5.2.10 Second aluminum etch

To obtain the final wafer topography, the protecting aluminum layer is removed. It is necessary to remove the aluminum layer because being conductive; it would represent a complex index to a guided wave disturbing confinement. Aluminum removal is accomplished with a 5min Hot phosphoric etch. A longer etch time is used to ensure the entire aluminum layer is removed. Over etching, and/or undercutting, is not a concern in this process step as phosphoric acid can not etch silicon. A similar post etch procedure is followed, including a soak in DI water and SRD. A diagram of the final wafer cross section is given in Figure 56.

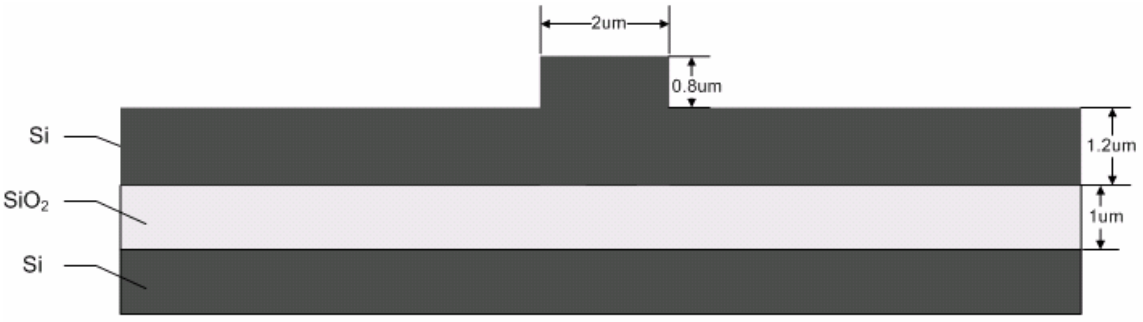

Figure 56. Final wafer cross section

A picture of the bottom left corner of the die at 10x magnification after the last fabrication step is given in Figure 57. It can be noticed that some areas such as inside the lettering P, and D the aluminum etch did not clear entirely, preventing the silicon from etching in that area. This is due to enclosed shape of the letter which traps air bubbles. This defect did not occur on the guiding structures themselves.

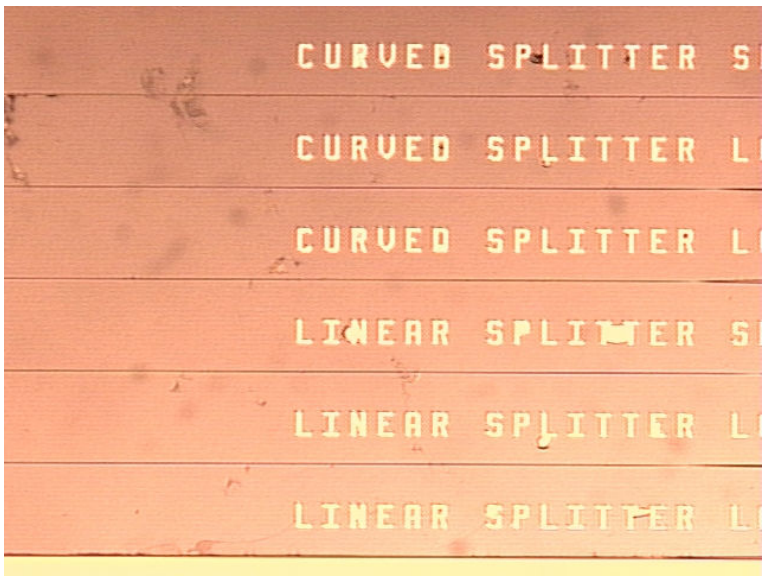

Figure 57. Picture of bottom left corner of die (10x)

Because these structures are long compared to their width, it is difficult to visualize them once fabricated. In order to view the entire structure several (8 or more) pictures along their length are taken at 100x magnification, and Photoshop is used to stitch them together. Once compiled the picture can be squeezed in the z direction, similar to the way Optiwave represents long structures. Pictures of three devices (a y-splitter, 3dB coupler, and MMI splitter) from the final device wafer, photographed in this way are given in Figure 58, Figure 59, and Figure 60 respectively.

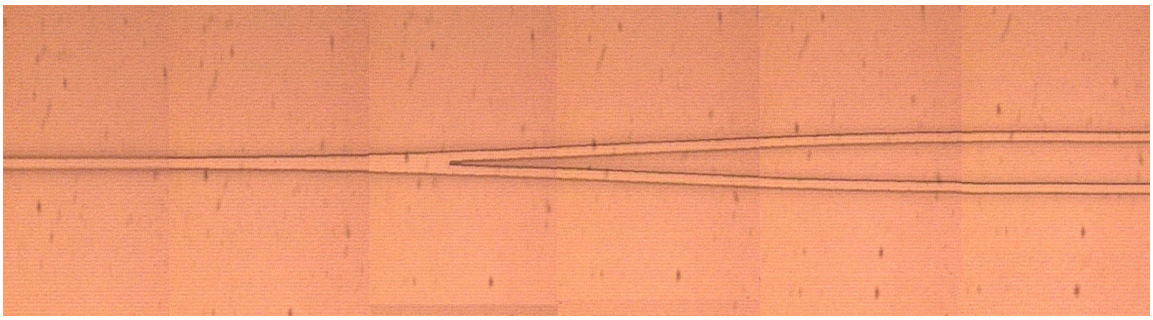

Figure 58. Fabricated y-splitter

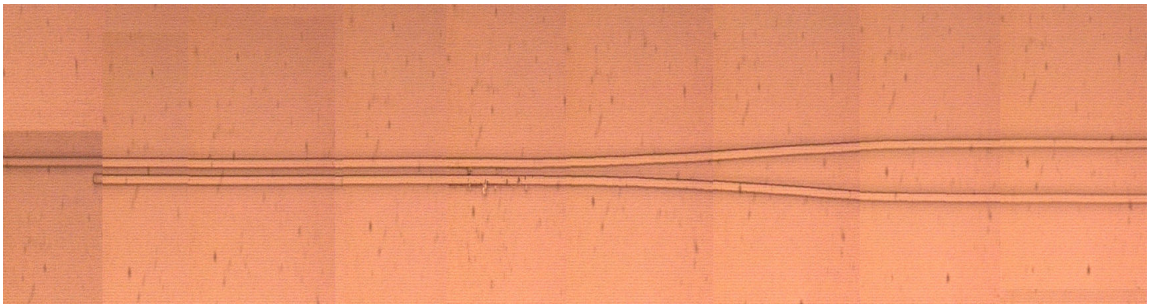

Figure 59. Fabricated 3dB coupler

Figure 60. Fabricated MMI splitter

The majority of the marks that exist in these images, specifically the ones that repeat between images each sub image, are due to particles on the microscope lens, and do not exist on the wafer itself.

5.3 Device measurements

After the rib structure is fabricated several measurements are made to determine how well these structures conform to design specifications. Planer dimensions, specifically the width and separation of waveguides, are measured using a microscope attached to a computer with analysis software. The software is calibrated to the microscope objective, allowing physical dimensions to be applied to the image. Using this process an image of the single mode waveguide is obtained, and enhanced by increasing its contrast. A plot of the pixel values along a line perpendicular to the waveguide is given in Figure 61. The edges of the waveguide correspond to a largest pixel contrast and are seen as high inflection points in the curve.

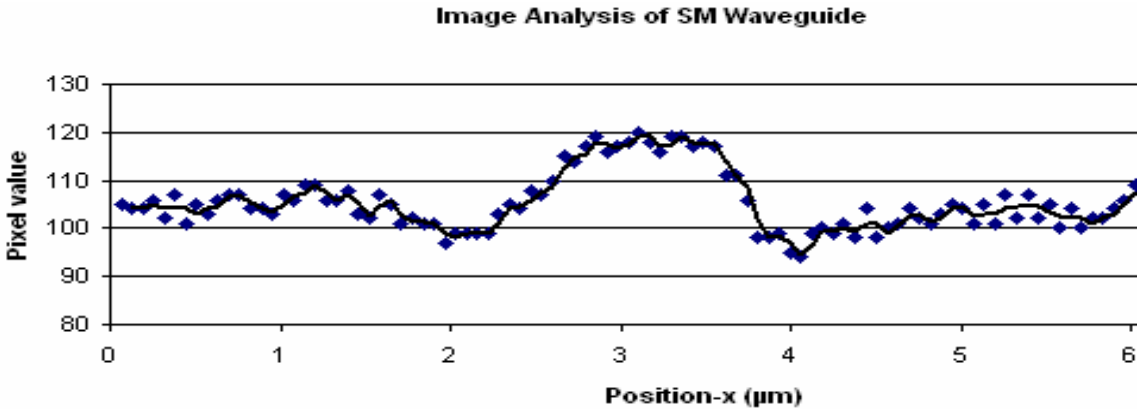

Figure 61. Pixel values across a picture of the waveguide

From this data the width of the waveguide becomes apparent. By taking measurements of the single mode waveguide on several die an average width of 1.577µm is obtained with an expected value of 2µm. Similar measurements of waveguide separation in the 3dB coupler yielded an average of 2.8µm, when 2.5µm is expected. The discrepancies between values are attributed to over etching of the aluminum that results in a uniform

reduction in line width, and increased in spacing of ≈0.15µm per edge. The cause of this mismatch is confirmed by taking a measurement of the line width after the photo resist is developed. This measurement showed that the width of the resist region was within 0.1µm of the desired dimension of 2µm. It was only after the aluminum etch, and removal of photo resist that the discrepancy in dimensions was observed on the aluminum mask layer. The impact of this inconsistency will be considered later in this section.

The measurement of vertical dimensions, primarily the rib height, is accomplished with the Tencor P2 profileometer as seen in Figure 62. This tool operates by dragging a fine tip over the surface of the wafer; the displacement of the tip is recorded, giving accurate measure of wafer topography.

Figure 62. Tencor P2 profileometer

Step height measurements of the MMI device were made on several die ranging from the center to the outer edge of the wafer. The data points obtained are plotted in Figure 63, and labeled based on there location. The measured rib heights ranged from 0.67µm at the center to 1.19µm at the edge of the wafer, with the nominal value of 0.79µm in-between. The range of these values is expected, and given the correct die, will match closely to the designed rib height of 0.8µm.

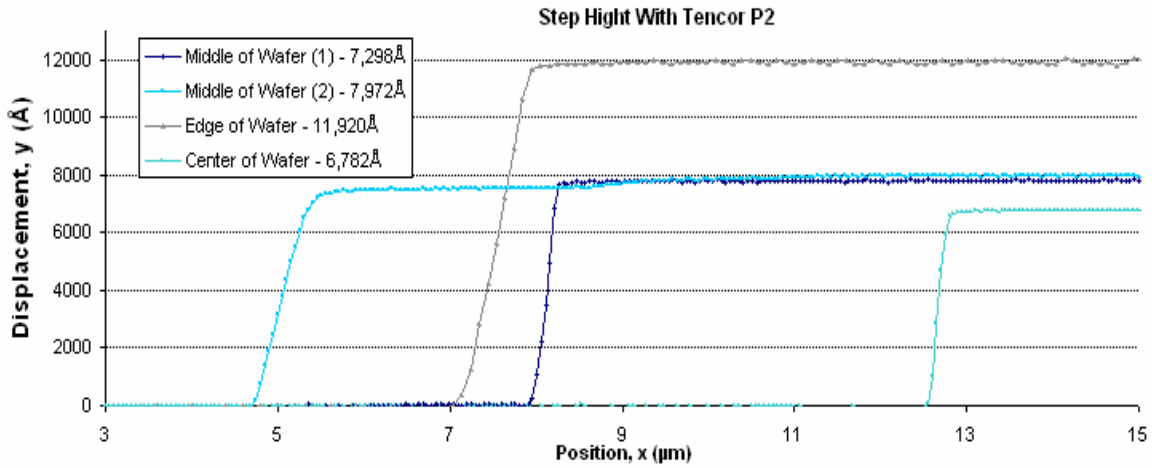

Figure 63. Step height data from Tencore P2

5.4 Process Problems encountered

During development of the fabrication steps used in this process, several problems were encountered which impacted the quality of the resulting rib structure. The majority of these issues were addressed, and resolved prior to processing the device wafer. The cause and solution to these problems will be discussed. In addition there are several issues and

possible improvements which have been identified and should be employed in any future revisions of this design. The means of implementing these design improvements will be described as well.

During the first round of test wafers several problems emerged that severely distorted the waveguide shape, and in many cases waveguides that were in close proximity, such as in couplers, merged together. Although many factors contributed to these waveguide imperfections, the root cause was determined to be silicon particles on the wafer. These small pieces of silicon turned out to be residue from the 1% Si Al that was sputtered on as a hard mask. The 1% Si Al is advantageous in transistor fabrication as it improves the bonding between poly and the aluminum interconnects, however it turned out to be a source of many problems for waveguide fabrication. When the hot phosphoric acid was used to remove the aluminum hard mask, it left behind these small pieces of silicon, and in some cases the aluminum near by which could not etch. Testing revealed that repeated plasma processes, such as reworking wafers by removing photo resist after a failed lithography attempt, considerable increased the amount of silicon residue left on the wafer. It is suspected that heat encountered during plasma processes such as ashing further fuse the silicon partials to the wafer and surrounding aluminum reducing the potential that the partial can be removed during the aluminum etch. Another problem that added to the defects crated by these partials resulted from photo resist that was left on the wafers, during the silicon etch. It is suspected that a sufficient amount of heat produced during the RIE warms the softened the resist enough to allow it to flow off of the rib

region onto the near by silicon partials. The flowing of the resist was further exaggerated by problems where the reflected power in the Drytek was much higher then expected. The high reflected power would cause even further heating increasing the potential of the resist layer deforming. The displacement of resist in conjunction with the left over aluminum that adhered to the silicon residue, caused the distortion of the Si etch. The result was that the RIE did not remove the areas beneath these Si particles, leaving behind large areas of Si near the waveguides. In cases where the waveguides were close together and a particle fell between the waveguides, the waveguides merged. Pictures of the severe impact that the Si residue had on waveguide shape can be seen below. Figure 64 right shows a 20x magnification of lettering after the final Al etch. It can be seen that there are small areas where the aluminum was not removed. It should be noted that these test wafers under went extended aluminum etch times (10-15min) with no noticeable impact on the aluminum remaining on the wafer. Figure 64 left shows a 100x magnification of the initial section of a 3dB coupler after it was processed. It is clear that these deformities would severely hinder, if not entirely prevent, the operation of the waveguide structure. Losses would be extremely high due to the non-uniformity and the particles may add further volumetric losses in the waveguide. In addition, aluminum on the guiding structure would introduce a conducting region, and thus a complex index on top of the waveguide, disrupting wave confinement.

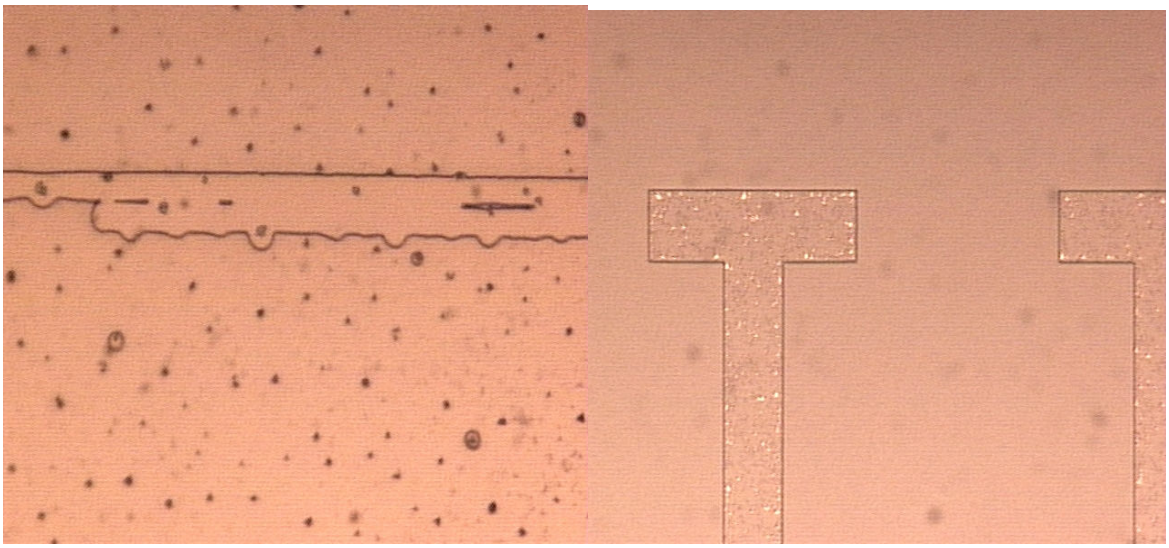

Figure 64. Deformed Waveguide (Left), Remaining aluminum on lettering (Right)

The obvious solution to improving the waveguide uniformity is to avoid using aluminum with the 1% Si all together. This solution is the most optimal however it could not be implemented since the time the problem of the Si residue was revealed, the device wafer had already been coated with aluminum, and there was no way to remove it. In order to rectify wafer several small modifications were made to the process. First the resist layer was removed after the Al etch, eliminating the ability of it flowing into unwanted regions. By the time of the lithography stage, the process had also been well defined through testing, eliminating the need to rework the wafer, and avoiding the use of plasma etch. By not having the ash the wafer the potential of silicon partials reaming on the wafer was reduced. Before the silicon etch of the device wafer, the high reflected power that was noticed during tests was fixed, further reducing the number of Si particles adhering to the surface of the wafer. Testing also revealed that some of these particles could be removed if the surface was physically cleaned; this prompted the use of the SRD in the process

flow after each aluminum etch. Finally, it is believed that the inherent cleanness and smoothness of the surface on the device wafer as compared to the test wavers, greatly improved uniformity. With all these slight modifications the device wafer was processed with no visible distortions or left over silicon residue, providing the high quality waveguides seen in Figure 58, Figure 59, and Figure 60.

In future processing a pure Al should be used in place of the 1% silicon in aluminum. Although a pure Al target was not available at RIT, Al can be deposited by evaporation. After the processing of the device wafer this was attempted to confirm the source of the specks left on the wafer. As expected the evaporated Al, left no residue and provided a perfect underlying waveguide layer. If it is required that sputtering be used a protective sacrificial oxide should be placed prior to the Al. When the oxide layer is removed following the aluminum etch, any remaining silicon would be removed as well.

The last problem which arose during fabrication was the shrinking of the masking Al layer during the hot phosphoric etch. The over etching of 0.15μm to 0.25μm which occurs at each edge dramatically effects waveguide width and thus guiding properties of the structure. A diagram showing how over etching effects waveguide formation during the aluminum and silicon etch steps is seen in Figure 65. The picture on the left shows how aluminum will etch underneath the protective resist and the picture on the right the impact this has on the dimensions of the final rib structure.

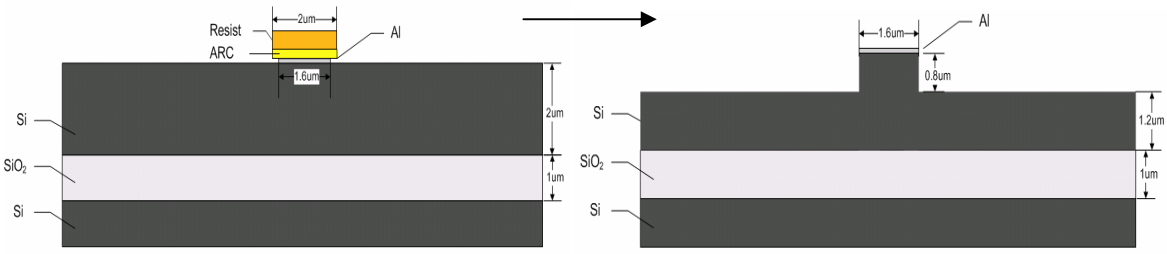

Figure 65. Diagram of aluminum over etching

There are two solutions to this problem which should be considered in the next revision of the fabrication process. The first option would be to compensate for the over etch by designing all structures to be larger then desired. The second option would be to use a dry aluminum etch that could be done on the Lam4600, to increase the anisotropy of the etch. A more anisotropic etch would reduce the amount of over etching, and help to maintain the final waveguide dimensions. The use of a dry etch is the preferred solution as it would allow the design to be independent of the process. Increasing waveguide width on the mask is also more difficult because it requires modifications to the layout within the OptiWave BPM software before being exported to GDS II.

5.5 Impact of fabrication tolerance on device performance

Each dimension of the SOI rib waveguide has an associated tolerance or range of deviation from its designed value. These discrepancies can have a large impact on the anticipated performance of a given device, particularly couplers which are designed for a specific modal confinement. There are four primary dimensions which can vary in the waveguide structure, the waveguide width due to aluminum under-etch (2µm to 1.5µm), rib etch depth due RIE uniformity (0.65µm to 1.2µm), device layer uniformity given by

the wafer (2.2 µm +/- 0.5µm), and the BOX uniformity given by wafer (1.09µm +/- 0.05µm). A diagram to scale, representing these possible variations in the fabricated structure is given in Figure 66. The dark and light gray regions represent the designed structure, and each of the four colors represents the range for a given dimension.

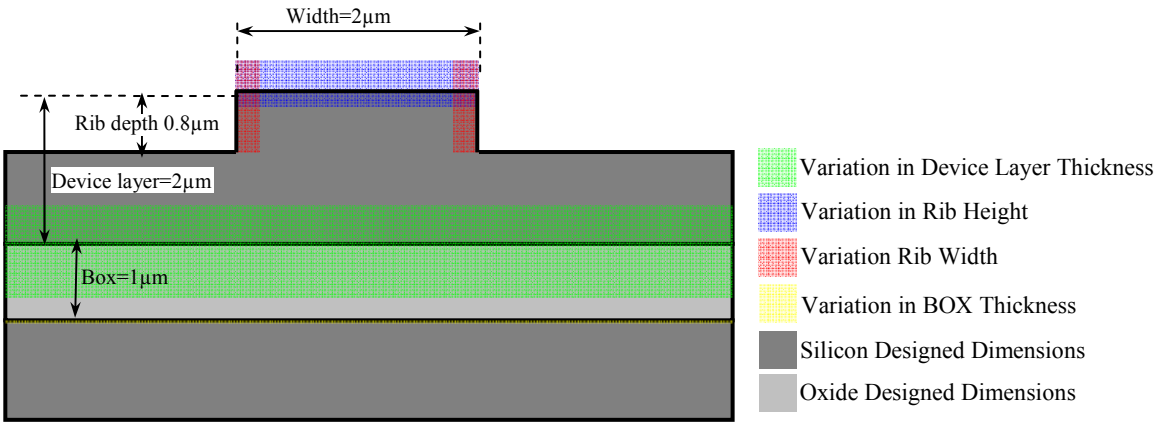

Figure 66. Variation in dimensions of single mode waveguide

Of these variations the waveguide width and depth are process dependent, while variation in the BOX and Si device layer are inherent in the wafer. In the evaluation of the effects of these variations on device performance the BOX tolerance is neglected due to its minimal variation. The first major difference that will occur as a result a change in rib profile is the field distribution supported by the waveguide. Given the conditions for a single mode propagation studied earlier it is observed in certain cases (rib depth 1.2µm and shallow device layer 1.7µm) that it is possible for device variation to push the single mode waveguide into multimode operation. Using Optiwave it was confirmed that three modes can propagate given that correct extremes in tolerance take place. To minimize the

potential of such unwanted behavior it is critical that device die around the edge of the wafer be avoided.

The other major effect that device variation has on the properties of a propagating mode is how well it is guided. The deeper the waveguide is etched, the wider the waveguide width, and thinner the device layer, the more confined the light will be. In structures that rely heavily on the evanescent coupling such as the wavelength splitter, this variation can prevent correct device operation. To determine the impact of device tolerance on mode confinement the coupling between two rib waveguides separated by a distance of 1.5μm is determined through simulation. The coupling length is measured for each extreme of a given dimension. A table representing these results is given in Table 9.

Table 9. Variation in coupling coefficient with device tolerance

	K at Design dimension	K at Max dimension	K at Min dimension
Rib Height	1678.201204	148.6933289	2944.323012
Rib Width	1678.201204	1678.201204	2296.485858
Si Device Layer	1678.201204	38693.37685	537.0813067

The first column represents the nominal value of K given a structure with the designed dimensions. The preceding columns show the new value of K after a given dimension changes to one of the tolerance extremes. The huge chance in K, particularly for variations in rib height and device layer thickness, would alter the effective coupling length by factors of ten. Even in the case of rib width a several hundred micrometer change would occur. In waveguide splitters or 3dB couplers an alteration in coupling

length by only fractions of the design length would greatly decrease performance. Due to the extreme sensitivity of these structures to variation in fabrication, even to uncontrollable properties of the substrate, the intended operation of these devices is extremely difficult to achieve. Choosing the correct die on the processed wafer can help to minimize variation and increase the chance of characterizing a working device. Future options for improving device uniformity at RIT involve a better characterizing the Drytek etch process, or other method of etching. Implementing a dry aluminum etch would also help to minimize variation associated with waveguide width. Further improvements can be achieved by using a higher quality substrate possibly based on an Epitaxial formed silicon layer to improve device layer uniformity.

5.6 Summary

This section showed the design of an effective fabrication process which is implemented to realize the waveguide structures simulated earlier. The many problems encountered during the fabrication process are discussed and the ways in which they could be fixed are considered. It is found that aluminum with 1% silicon can be detrimental to waveguide uniformity, and should be avoided. The uniformity in waveguide width can be improved by using plasma to etch the aluminum rather then phosphoric acid. During the evaluation of the device tolerance it is found that even slight variation in rib height, rib width, and device layer thickness can not only push a single mode waveguide into multimode operation but also dramatically effect design parameters such as the coupling

coefficient. Future implementations of the rib waveguide coupler should be designed to minimize device variation and increase uniformity.

Chapter 6: Experimental Measurements

One of the most difficult aspects of realizing a waveguide device is experimentally observing and testing its operation. The problems associated with focusing, and aligning light with submicron resolution, into the end facet of the waveguide can be complex. A precise methodology is required in order to minimize incretion losses, and confirm device operation. This section of the thesis will discuss the techniques used to test these waveguide devices, and the practical problems that were encountered. The observed behavior and the results that could be obtained are stated.

6.1 Facet preparation

Before testing can begin an interface facet, an edge perpendicular to the waveguide which exposes its cross-section, must be created. Such a cut is necessary as it provides a point through which the waveguide can be excited by laser light, and/or the output measured. There are two primary methods considered in this thesis through which the interface facet can be created; this is by, cleaving, and sawing. Cleaving involves scribing the wafer with a diamond tip and breaking it along its 1-1-1 crystal plane. For the device wafer which has its surface on the 1-0-0 crystal plane an angle of 54.74° will occur between the surface of the break and the wafer. The advantage is that, if properly done, it can produce a near perfect facet with low roughness. A minor disadvantage of the cleaving method is the angle it introduces to the edge facet. As the angle between the surface normal and the light ray increase, reflection off the interface increases, as defined by Fresnel's equation. In this case the angle of the cleave will introduce an additional 7% loss to the 30% loss that would occur at normal incidence of a light ray on a silicon-air interface. These losses would total to 37% per facet. Sawing of the edge facet can avoid this angle, as well as the difficulty of manually scribing and cleaving the wafer in the correct spot (this must be accurate within millimeters). A disadvantage however, is the roughness that sawing can produce on the wafers edge. Pictures of the sawed edge at 10x, as well as successful and unsuccessful cleave wafer edges, are given in Figure 67.

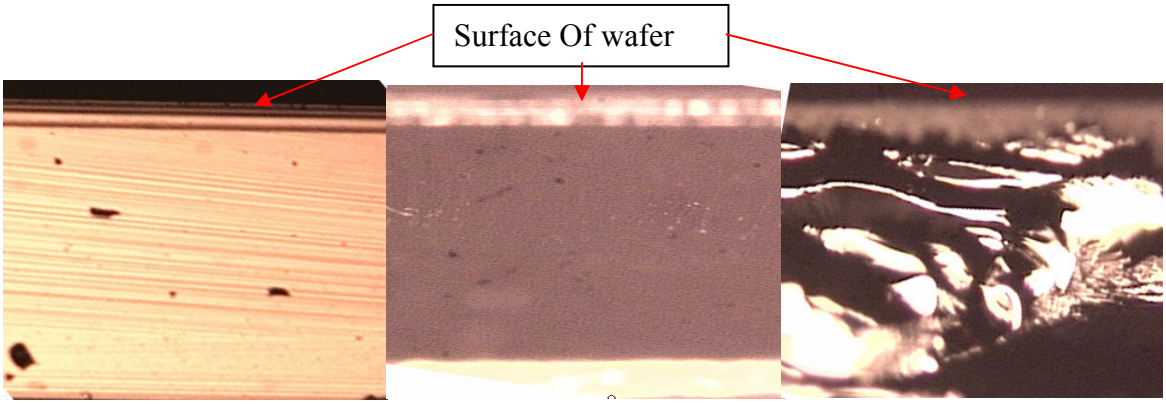

Figure 67. Wafer edge sawed (left) good cleave (center) and poor cleave (right)

For the sawed facet notice the lines where the blade cut, these surface imperfections are what cause scattering and thus losses. In the cleaved pictures the center represents a clean break; the almost solid black color indicates the high degree of uniformity in the edge. The picture on the far right shows the poor cleave, where the break did not occur on the lattes plane at all. It can be seen that there is a large degree of topography variation.

Both of these facet methods were tested, it was determined the cleaving method was not sufficiently reliable; a single mistake could result in the loss of a large portion of testable devices. Cleaving had a high probability (70%) of not breaking on the lattes plane correctly, which would produce a poor interface. The wafer saw however, would be able to dice the wafer with 100µm resolution into individual die (19mmx19mm), making handling and testing much easier. The wafer saw used is the Karl Suse, KS775, a picture of which is given in Figure 68.

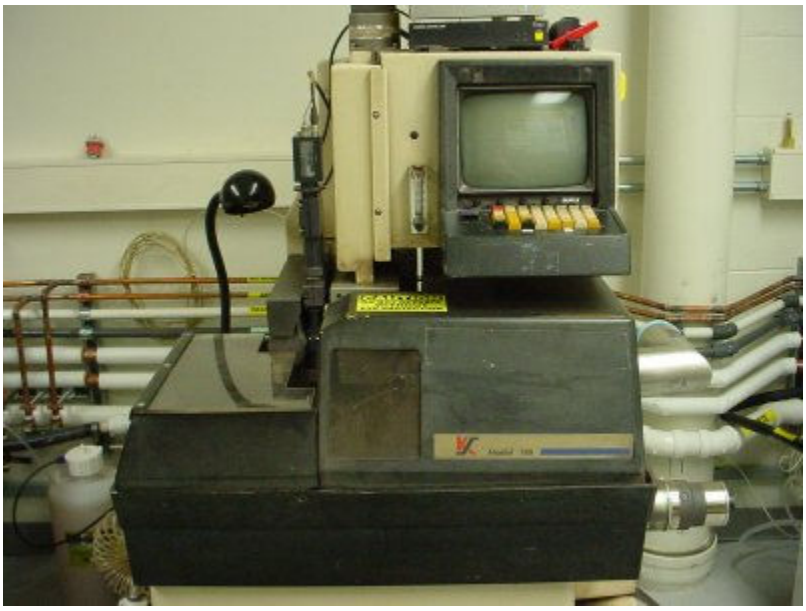

Figure 68. Ks775 wafer saw

Prior to dicing, a layer of photo resist (standard coat recipe) is deposited on the completed wafer, this will serve the purpose of protecting the wafers surface from silicon dust generated by the saw, as well as air particulate, as the sawing step will be preformed outside the clean room. To dice the wafer an x-z step recipe is used, with three sets of seven cuts. One set is done in the x direction and two in the z direction, with each cut within in a set separated by 19mm. The separation between cuts and number of cuts per set are chosen based on the number of die in a given direction and separation between die. For the set of cuts in the x direction the blade is chosen to be in the street between the die, with the purpose separating adjacent die. In the z direction however one set of cuts is placed at the beginning of the waveguide on each die and the second at the end of the waveguide. By cutting through the waveguide on each end of the device, the waveguide cross section is exposed as desired. A picture of the device wafer after dicing can be seen

in Figure 69, with several die removed. The blue material beneath the wafer is a special adhesive used to hold the die together after they have been cut. The saw which cuts from the top of the wafer is designed to go only as deep as the bottom of the wafer, leaving this tape intact.

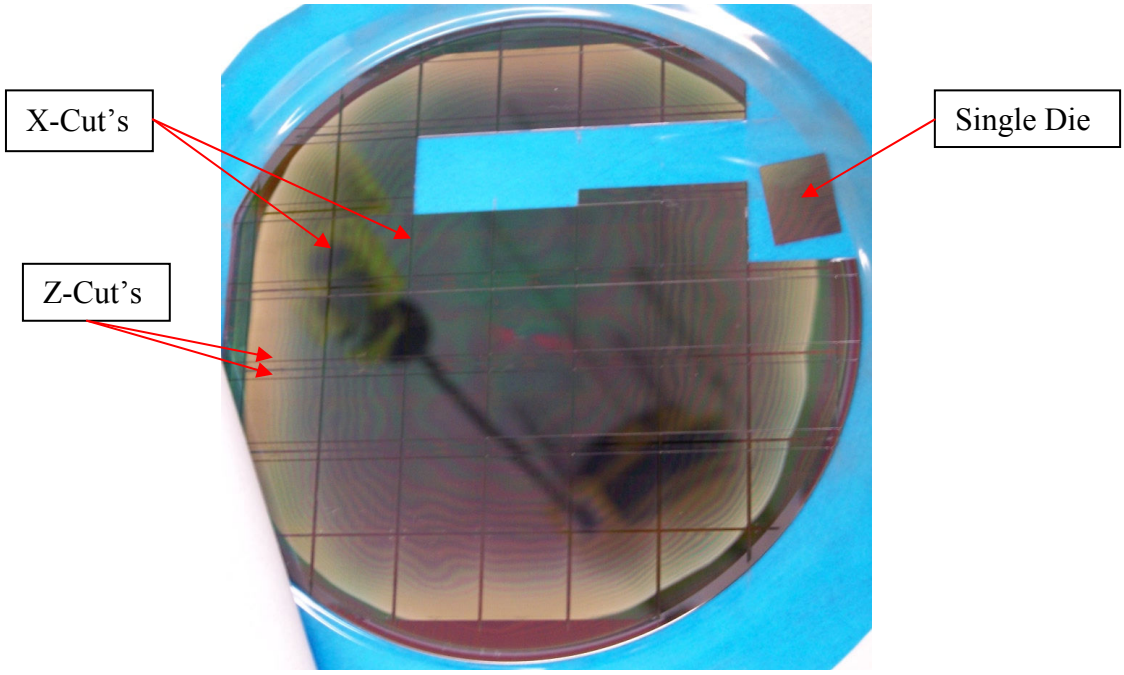

Figure 69. Device wafer after dicing

As each of these die is now separated it is possible to test them individually. The advantage of this is that modifications can be made to a given die to see its impact on device operation without impacting the entire wafer, as would be required with cleaving. One such improvement that was attempted is the polishing of the waveguide facets. By smoothing the imperfections created by the saw blade it is theoretically possible to reduce scattering, and improve coupling into the waveguide. The polishing of these edges was

accomplished with a jury-rigged Ultra TRC fiber polisher. The polisher itself is seen in Figure 70, on the left, and on the right a polishing pad.

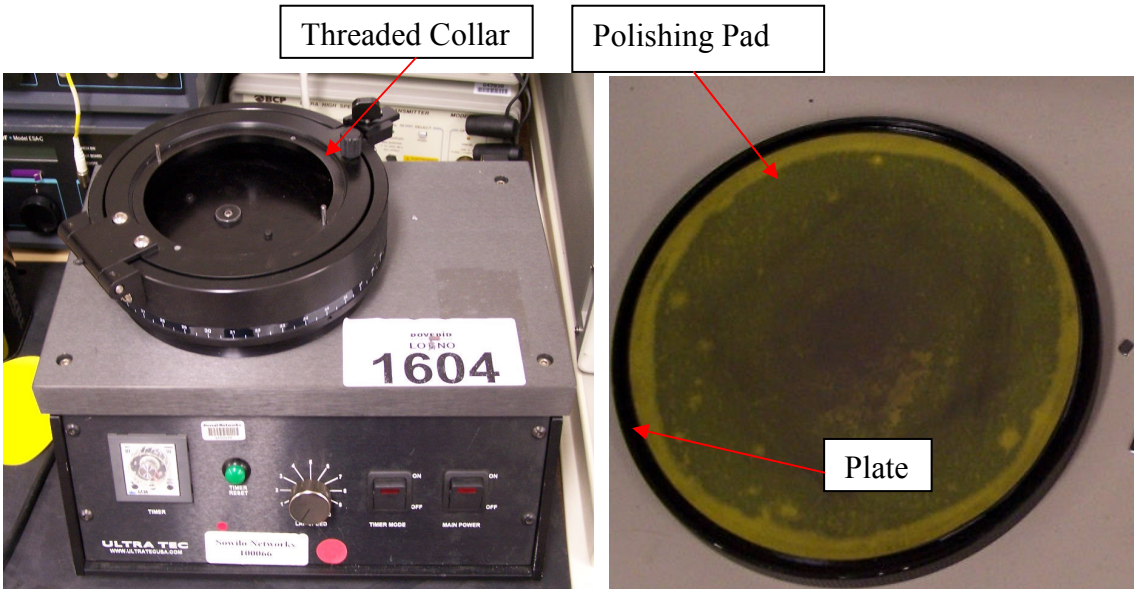

Figure 70. Ultra tec fiber polisher (left), polishing plate (right)

Pads for the polisher come with an adhesive and are placed on a plate which mounts to the polisher. When turned on the plate and pad make a figure eight motion to uniformly polish a fiber tip. If desired the speed, and polish time can be set. In order to adapt this tool to polish the edge of a die, a bracket was machined to hold the small silicon die over the pad. A picture of the bracket is seen in Figure 71. Two attach points, a hole and notch one on each end, allow it to slip over pegs on the outer rim of a collar which covers the polishing plate.

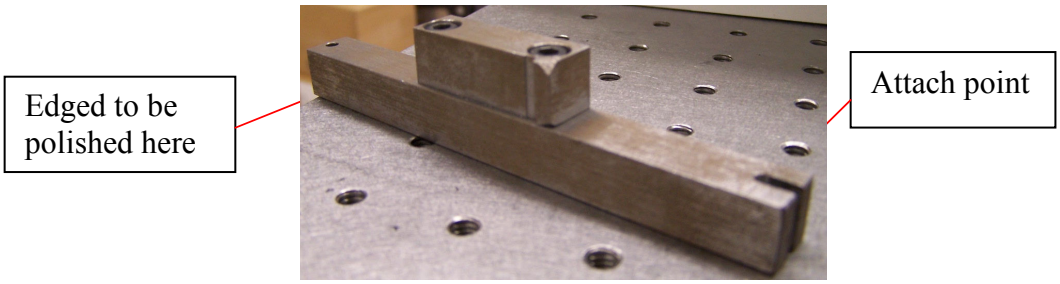

Figure 71. Bracket made for holding die over polisher

The protruding half inch bar stock in the middle is slightly offset from the longer piece so the die can be placed against the upper edge of the bracket to keep it flat. A small c-clamp is used to hold the die in place. A piece of brass is placed between the die and the clamp to distribute force over the die, as well as to prevent damage to its surface. In the bracket in Figure 71 the edge to be polished would face upwards, when inserted into the polisher the bracket would hold the edge of the die up against the polishing pad. The height of the bracket is adjusted by turning the threaded collar. Using this setup the edges of several die were polished, one with a 12µm grit, another with 12µm and 3µm grit, and a final with 12µm, 3µm and 0.3µm grits. The polishing time at each grit size is 10 minutes, at speed level of 5. Pictures of each of the three polished edges at 10x magnification are given in Figure 72, with the most polished edge on the right and least on the left.

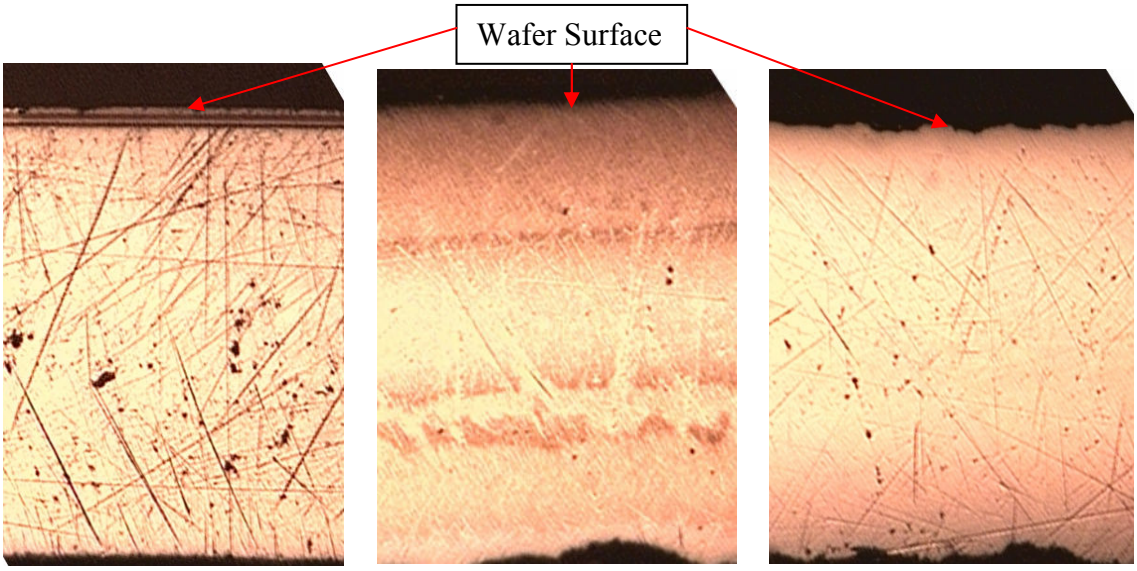

Figure 72. Edge of wafers after polishing (fine grit right, course grit left)

It can be seen from these pictures that the 12µm grit actually increases the surface roughness of the edge as compared to the saw alone. The 3µm and 0.3µm grits further improve the edge surface quality. For the image on the right however there can still be seen the underlying score marks of the initial 12µm polish. Improvements can be made to the process by either skipping the 12µm polish, or increasing the polish times for the 3µm and 0.3µm grits. Through the process of characterizing the polishing tool a consistent problem arose regardless of the polishing parameters of polishing time, force on the die, or seed of the pad. It was found that although the polishing technique could improve the edge of the wafer it induced damage to the device layer on the surface of the wafer near the facet. The damage observed is a chipping of the surface due to the pads movement perpendicular to the edge of the facet. Three pictures at 10x, 20x and 100x of the top edge of the wafer can be seen in Figure 73.

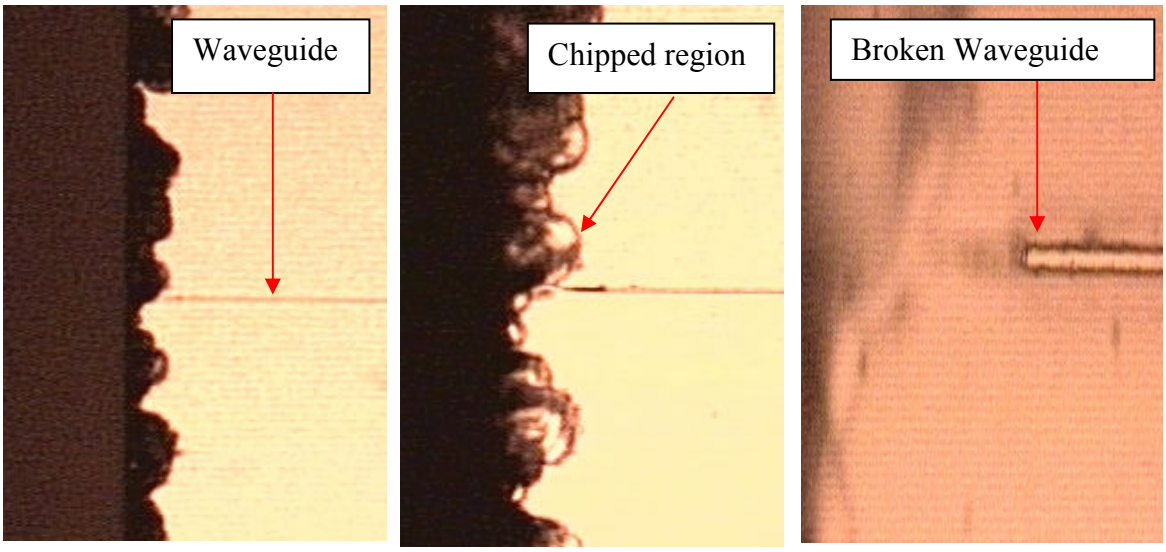

Figure 73. Top edge of wafer after polishing, at 10x, 20x, and 100x

It can be seen particularly in the 100x image that the chipping not only makes for a rough surface near the polished edge, but in many cases also removes portions of the waveguide in that region. Other methods such as sandwiching one die between two others during the polish was attempted in the hope that protecting the surface would eliminate the chipping however no noticeable improvement was observed. The severity of the chipping was seen to be dependent on the relative direction at which pad went across the edge of the die. When the pad went in a direction perpendicular to the edge in the direction from the back edge of the wafer to the front chipping was the worst. Despite this it was determined during imperial testing that the poorly controlled polishing method caused more losses through surface damage then there would be if it was just left as a sawed or cleaved facet. It was also considerably more difficult to get light to couple into a waveguide that had a chipped surface from polishing. For these reasons the polishing was not pursued as a viable method to reduce insertion losses at this time. Further characterization of the

polishing setup should be preformed in future work to minimize its damaging impact. In the testing of the final device wafer the majority of the dies were left as a sawed facet. In some cases the die itself was further cleaved back by marking with a diamond tip scribe and breaking. The primary purpose of further breaking the die is to remove the unneeded leading and trailing waveguide originally included to allow the devices input and output ports to line up. By removing the unneeded waveguide, losses from factors such as sidewall roughness that would have occurred in the region can be avoided. In turn the total power reaching the active device is much higher, making observation and measurement of the propagating light more efficient. In these devices losses from surface roughness is considerable because no smoothing techniques were implemented. Cleaving of the die in some cases when a good break occurred proved to greatly improve coupling.

After these edge facets are prepared, prior to device testing, the protective layer of photo resist must be removed. This is done to insure a clean surface on the wafer. Any particulate on the wafer can cause de-confinement and scattering, increasing losses. The resist is removed with acetone, then the die is washed with DI water, and dried.

6.2 Experimental setup

The process of testing and observing the operation of these waveguide devices requires the ability to couple light into the 2μm wide waveguide with high precision and minimal losses. In order to do this a means must be devised to align a beam of light with the waveguide, see the alignment process and inferred wavelengths being used, and measure

the power at the waveguides output. The primary experimental setup designed to accomplish these tasks, is build out of a set of Newport optical translation tables, laser posts, fiber holders, and various mounting brackets. A diagram of this test set up is given in Figure 74.

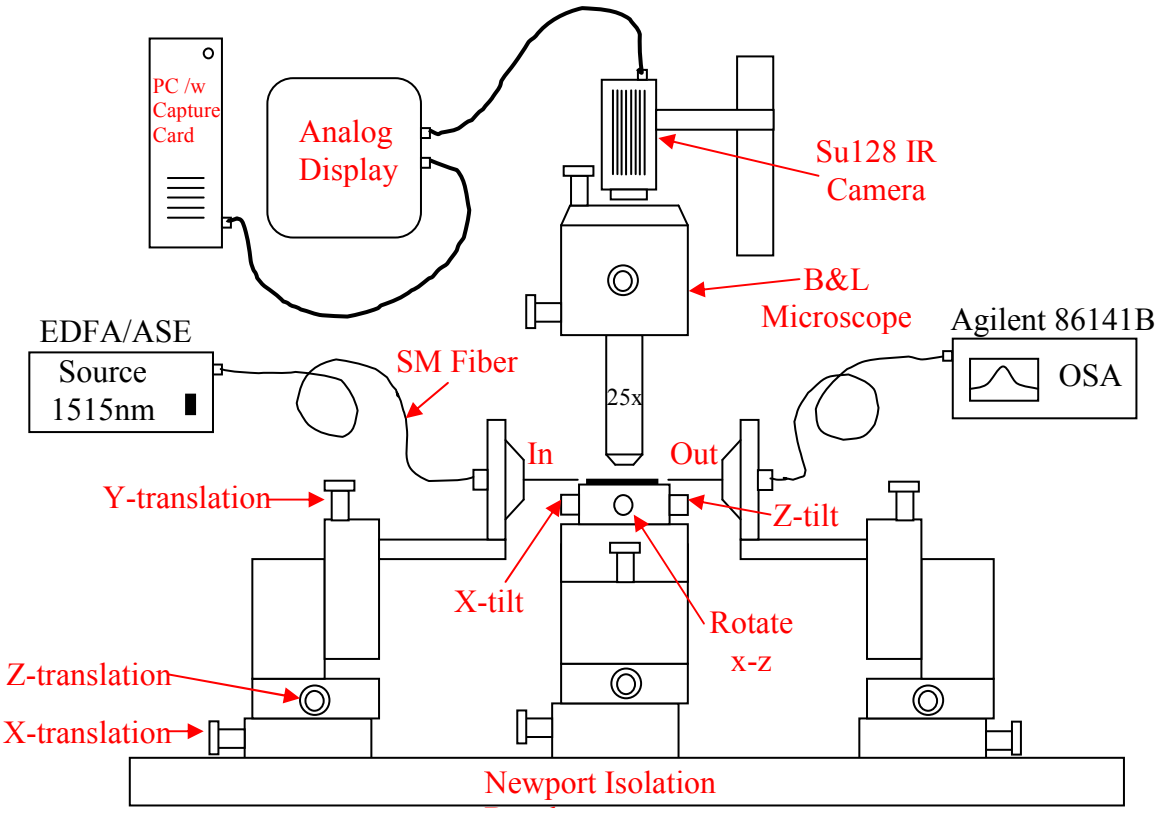

Figure 74. Waveguide alignment and test setup for x-z plane

The setup consists of four x-y-z translation platforms to provide alignment of the die to be tested, input fiber, output fiber, and location of a microscope. The input seen on the left holds a single mode fiber, which has had its protective shielding removed and its tip prepared as will be discussed later. This fiber tip used to illuminate the waveguide is

mounted in the fiber holder and can be aligned with a given waveguide device using the x-y-z translations stage. The other end of the fiber is striped, cleaved and mounted in a standard bare fiber connector. The connector is then attached to the desired input source, in this case either the EDFA/ASE, with wavelength content between 1521 and 1571nm and power of several milliwatts, or the AQ4321D tunable laser with a highly coherent output between variable between 1520 and 1620nm, and powers up to 6mw. A picture of each of these sources used is seen in Figure 75.

Figure 75. ASM (left), and tunable IR laser light source (right)

The center translation stage holds the die and is able to move independent of the input or output. The top of this stage also has the ability to be tilted in the x and z directions as well as rotated in the x-z direction. The ability to tilt and rotate the die, provides fine alignment of the waveguide and a means to correct for misplacement of the die when mounted to the translation stage. The output translation stage on the far right is similar to the input stage; however, it holds a prepared fiber tip to take in light coming from the waveguide output and transmits it to a measurement device, in this case, the Agilent 86141B OSA. This device is able to plot the power of an optical signal verses wavelength and is seen in Figure 76. Initial testing was preformed with a simple power meter;

however, the Optical Spectrum Analyzer (OSA) was eventually used as its ability to observe the spectral content of a signal, is important for wavelength splitting devices.

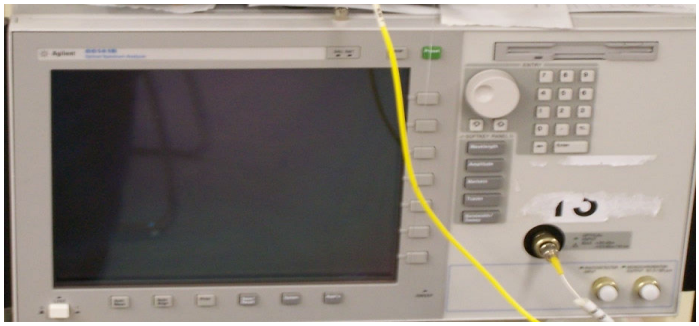

Figure 76. 86141B OSA

These three translation stages are critical to aligning the input and output fiber to the waveguide with submicron accuracy. Any deviation in angle or position of the fiber from perpendicularly aligned to the waveguide can greatly increase insertion losses.

Above the three alignment portions of the setup is microscope that has been detached from its base and connected to a laser post in order to hold it directly over the die. The microscope has its own set of translation stages in the x-y and z directions so it can be independently moved and focused with respect to the surface of the wafer. The primary purpose of the microscope is to observe the waveguides during testing and to allow visual aliment of the input and output fibers with the waveguide. The maximum magnification used is 25x, and was sufficient for the testing done. The use of higher magnification objectives were attempted, however alignment and focusing of the image became increasingly difficult due to the reduce depth of focus. At higher magnifications

vibrations also make observation increasingly difficult. At the top of the microscope there is a secondary observation port, it is here that a focusing objective is inserted and the SU128 IR camera, which can detect the near infrared wavelengths being used, is placed. The SU128-1.7T1 is an InGaAs photodiode array (128x128) with relatively uniform response between 900nm and 1700nm. The device has a sensitivity of 25.6nV/e^- to 55µV/e^- , 60µm dot pitch, and noise threshold of <270µV [82]. The camera is mounted on a laser post directly over the objective which can be manually adjusted to observe the image produced by the microscope. The camera visually confirms the guiding condition, and fine alignment of the input and output fibers. The BNC analog output of the camera is attached to both a CRT display and to the S-Video input of a PCI TV capture card (a BNC to Composite and Composite to S-Video adapters are used). The interface with the computer allows the digitalization and acquisition of pictures and movies from the camera for documentation. Two pictures of this set up can be seen in Figure 77.

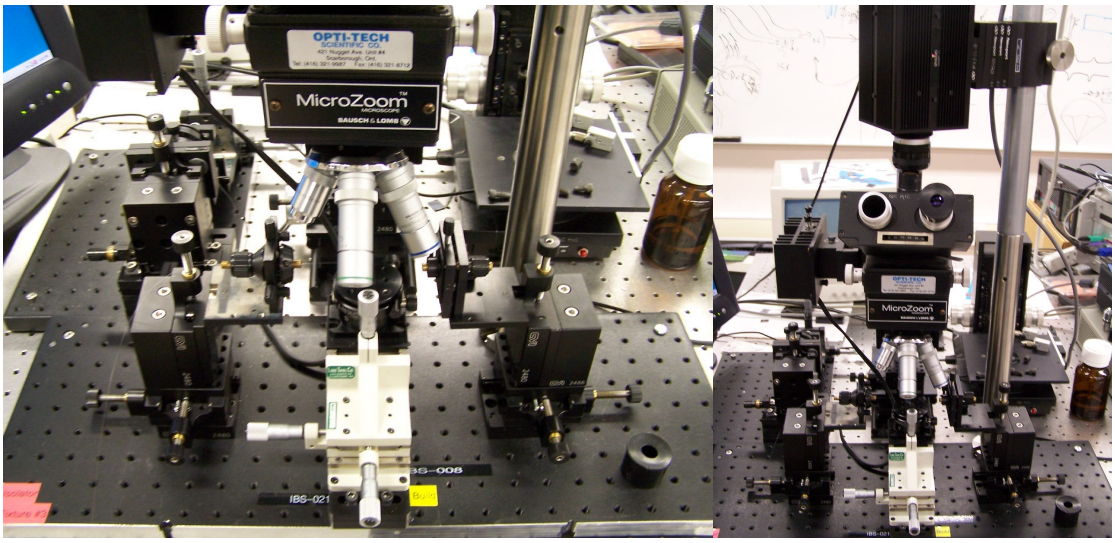

Figure 77. Picture of primary test setup for x-z plane

A second version of the setup is also implemented for viewing the edge of the wafer opposite the input source, rather then the wafers surface. A diagram of the second setup is given in Figure 78.

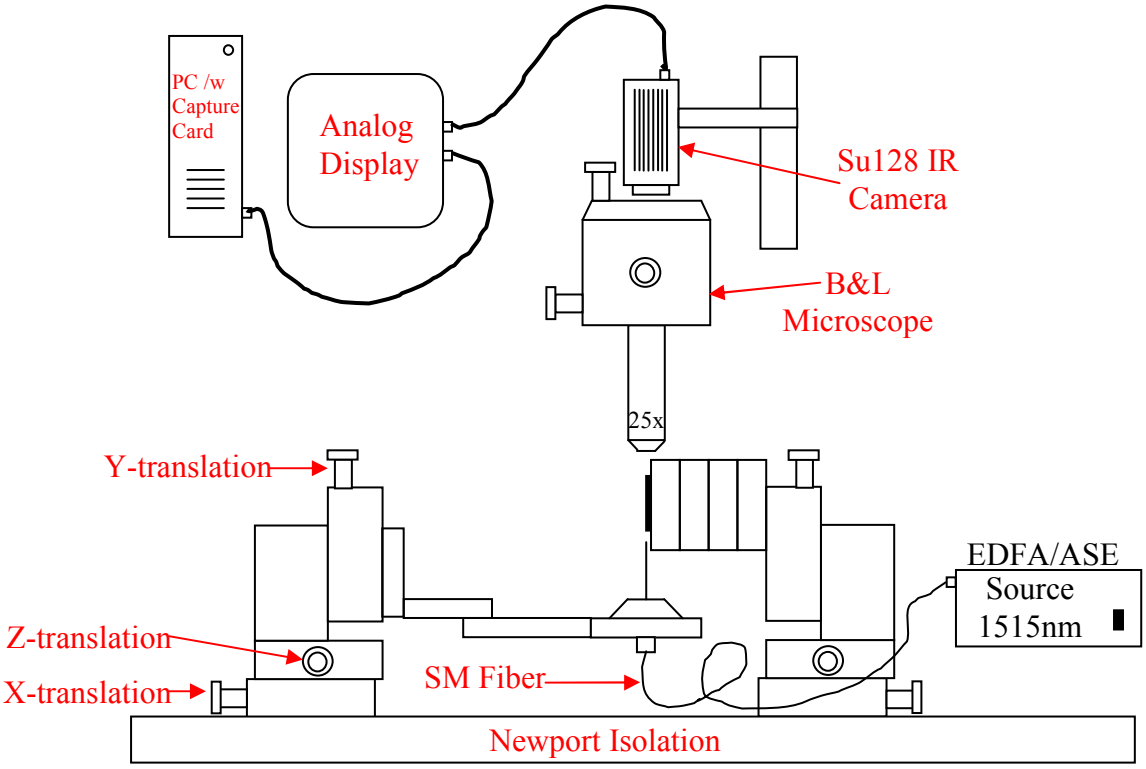

Figure 78. Secondary test setup y-x plane

This setup is similar to the primary test apparatus, and was built with the hope that it may be possible to observe the field profile on the exit facet of the waveguide. The setup consists of an input x-y-z translation stage which holds a prepared fiber tip near the input edge of the die. A second translation stage holds the die on its side. As both the die and input fiber are rotated by 90 degrees in this arrangement, the output edge of the die is facing upwards and can be viewed using the same microscope and camera setup. The

disadvantage to having the test apparatus rotated in this way is that fiber is not in the field of view of the microscope, making alignment of the fiber with a waveguide in the x-z plane a difficult, if not impossible, process. Despite the disadvantage this arrangement will provide valuable insight into what the edge of the wafer looks like when IR light passes through it. A picture of the second test apparatus, without the microscope and camera mounted above is given in Figure 79.

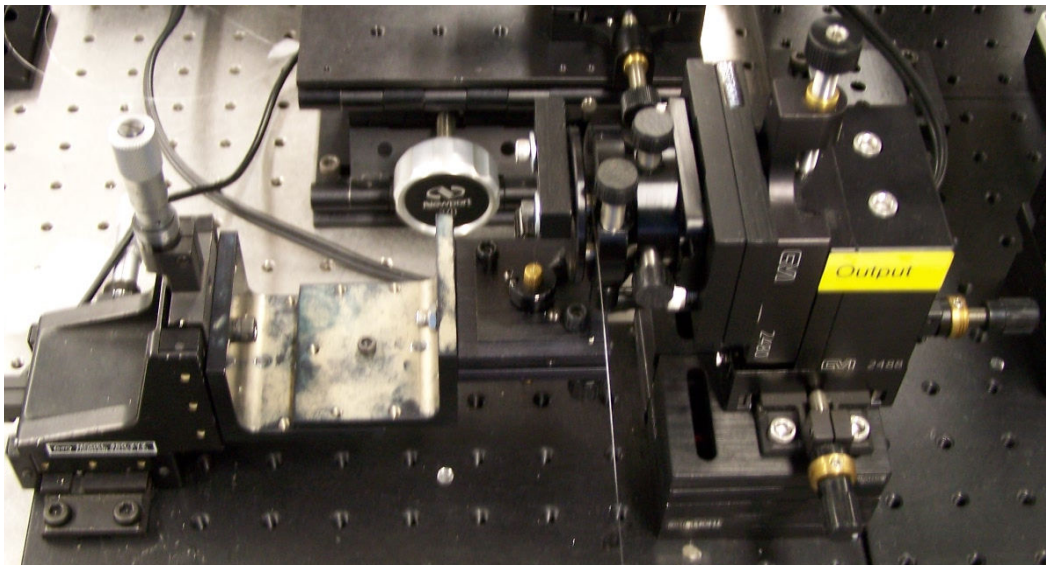

Figure 79. Picture of secondary test setup y-x plane

Using the experimental setups described here, these waveguide devices will be tested and pictures obtained. The nature of these test setups and design of the waveguide structures will allow their testing to be open ended. A further description of the testing process and results obtained will be discussed in a later section.

6.3 Input coupling techniques

Another factor, in addition to facet quality and alignment, critical to minimizing incretion losses is the technique used to couple light into the rib waveguide. The primary methods considered in this thesis include direct butt coupling with a cleaved or tapered fiber tip and focusing with a fiber lens or microscope objective. The cleaved method is the most direct, involves the least work to prepare, and has low losses for light leaving the fiber. The disadvantage to this method is that the spot size is limited by the diameter of the fiber core to 10μm. The cleaved tip is made by carefully striping back the protective plastic coating around the fiber and using precision cleaver as seen in Figure 80 to scribe and break the end of the fiber at a specified point.

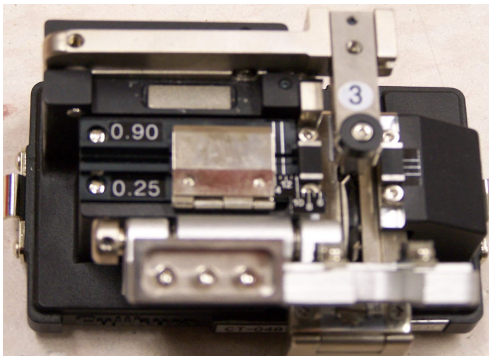

Figure 80. Precision fiber cleaver

The fiber taper is made by heating a portion of the fiber and pulling either end till it breaks. The regain where it is heated will stretch thinning the fiber and forming a tip that is submicron in size. The advantage of this method is that the tip is smaller than the width of the waveguide, so if properly aligned it can allow more light to couple into a given structure. Because the tip is not as smooth as a cleaved fiber however considerable

scattering will occur as light leaves the tip, the light will also diffract quickly. The tool used to make these tapers is the Ericson FSU 975 fiber fuser as seen in Figure 81. To use the fuser the middle of a fiber is striped, cleaned and inserted into the tool. When the correct taper recipe is run, the tool heats the fiber with an electric arc, and slowly pulls each end of the fiber until the taper is formed.

Figure 81. FSU 975 fuser

The fiber lens is created using the FSU 975 fuser as well. Rather then pulling the fiber a cleaved end is heated until a molten dome of glass forms on the end. This glass ball acts as the micro lens which focuses the light from the fiber. Unlike the taper this method provides low losses, however the spot size created is larger than either the tapered tip or fiber cleave. Another advantage of fiber lens is that optimal coupling can be achieved without having to bring the fiber within close proximity of the waveguide facet (3-4μm), but only to the focal point of the fiber lens (10-25μm). The final method that was attempted was the use of a cleaved fiber focused with a microscope objective. With this set up the focal length of the objective is about 12mm isolating the tip entirely from the

die. The method has a spot size similar to the fiber lens as well. The disadvantage to this method is that there are considerable reflections off of the lens surface introducing losses into the system. Although the fiber tip for this input method is cleaved, inserting it and aligning it with the objective can be difficult. Pictures of each of the four methods are given in Figure 82. The setup for the microscope objective seen on the far right required its own translation stage, as the fiber has to be properly aligned within the objective in addition to the objective being aligned with the facet of the die.

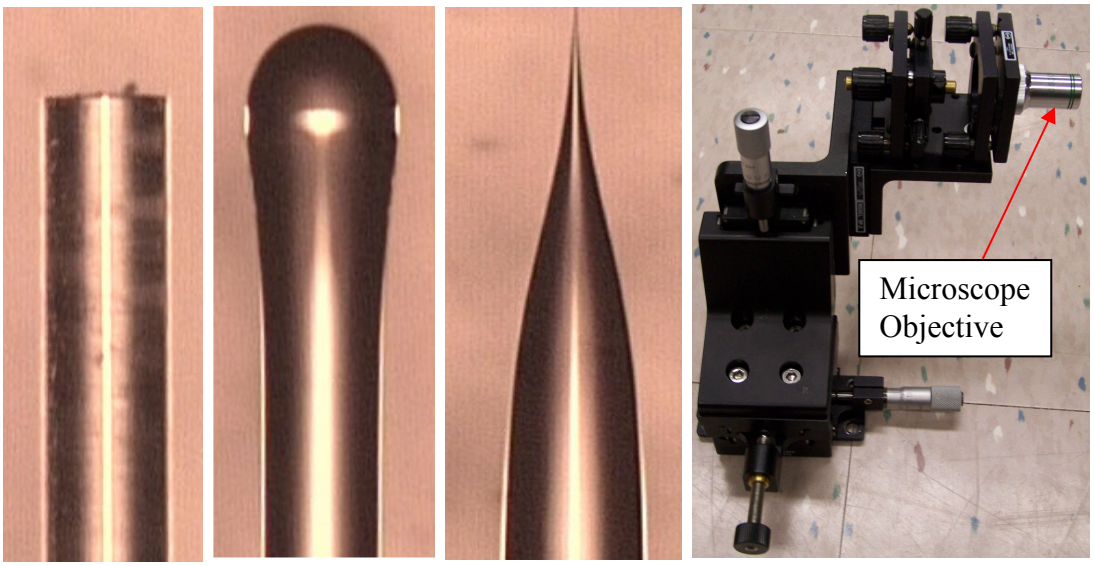

Figure 82. Types of input coupling methods used (cleave, Fiber lens, taper, microscope objective)

Due to difficulty in measuring the output power from the waveguide as will be discussed later, exact numbers proving which of these methods provides the lowest insertion losses could not be obtained, although similar performance was visually confirmed. In the majority of experiments the cleaved fiber end was used because it was simple to make,

less delicate than the taper, and relatively easy to align as compared to the lens structures. The intensity difference observed in the waveguide for type of fiber tips is minimal.

Other methods exist for improving alignment and coupling of light into a waveguide. Such methods include v-groves, grating couplers and waveguide tapers among others that should be considered in future versions of these waveguide devices. Each of these methods requires a layout modification and or an additional mask, which is why they could not be added in this thesis. The waveguide taper, which involves a simple layout change, could be the most effective improvement to increase coupling into the waveguide. The tapered waveguide is similar to the tapered fiber. It is similar because it is a waveguide that starts as a wide multimode region and funnels down to the single mode waveguide used by the device. Having the waveguide large at its input facet greatly improves the amount of light that is captured into the guiding region and reduces the sensitivity of alignment. The use of the waveguide taper eliminates the necessity of a prepared fiber tip because the wave waveguide taper increases the tolerance to beam diameter. Other methods such as the v-grove are achieved with a wet etch of the region just before the input of the waveguide. The wet etch will form a grove in the surface of the wafer due to the orientation of the crystal plane. The fiber can be set into this grooved region, insuring the correct alignment in both x-y and z directions. The groove structure can also insure high quality input facet as it is formed by a wet etch.

6.4 Results

The process of characterizing these devices through testing involves the careful alignment of the prepared die facet and fiber tip using the test setup from Figure 74. In order to insure the optimal alignment of the input with the waveguide several steps are taken. First, the die or piece of die is prepared, as discussed previously, and placed on the center translation table. The input fiber is also prepared and inserted into the fiber holder of the input translation stage. Careful handling of the fiber is important particularly with a tapered tip as allowing it to hit the side of the fiber holder or die can cause it to break. Prior to using the infrared camera a visual alignment and focus is done by looking through the top of the microscope, the same aperture used by the camera, since the focus is slightly different than the eye piece. Light leaving the microscope objective can be used to determine the approximant location on the die being viewed and if it is in focus, without having to look through the eye piece. This course alignment method is useful for the higher magnification of 25x when it is difficult to determine where one is looking. Once the input of the waveguide to be tested is located and focused, the fiber end must be aligned. This process can be assisted by inserting a visible laser beam, such as red, into the fiber from the opposite end. The location and focus of the fiber tip is determined when the laser light intensity is maximized at the waveguide facet. This method is particularly useful with the microscope objective as its focal point requires it to be so far from the edge of the waveguide facet that it can not be seen. Observing the fiber tip with visible laser light passing through it is also a good measure of its quality. If the tip of the fiber is not well cleaved or inherently rough, such as in the fiber taper, light will be seen

due to scattering. The less peek light that is seen emanating from the fiber or reflecting off of the waveguide facet then the lower the insertion losses will be. Once the fiber is aligned visually the light on the optical microscope can then be turned off and the infrared camera put into place. The other end of the input fiber should be removed from the visible light source and attached to the NIR source. Because the wavelength of the input has changed the focus of the microscope and fiber lens or input objective if used will also change slightly. This result stems from the fact that the lenses in the microscope used are optimized for a given wavelength, deviation from this value will cause the focal length to change. To correct for this the y caliper on the microscope can be adjusted slightly until the inferred beam as seen on the CRT comes into focus. In order to achieve coupling the y translation of the input fiber should be slowly varied as coupling is highly sensitive (0.8μm) to the y position of the fiber. A picture showing the fiber illuminating the edge of the wafer is seen in Figure 83 on the far left. The middle image shows a condition where the y-location of the input fiber is two high, no coupling is occurring. The picture on the far right represents the condition where light is coupling into the waveguide, as seen by the light in the guiding region. The propagation light in the waveguide is visible as there are small amounts of scattering off the edge of the waveguide.

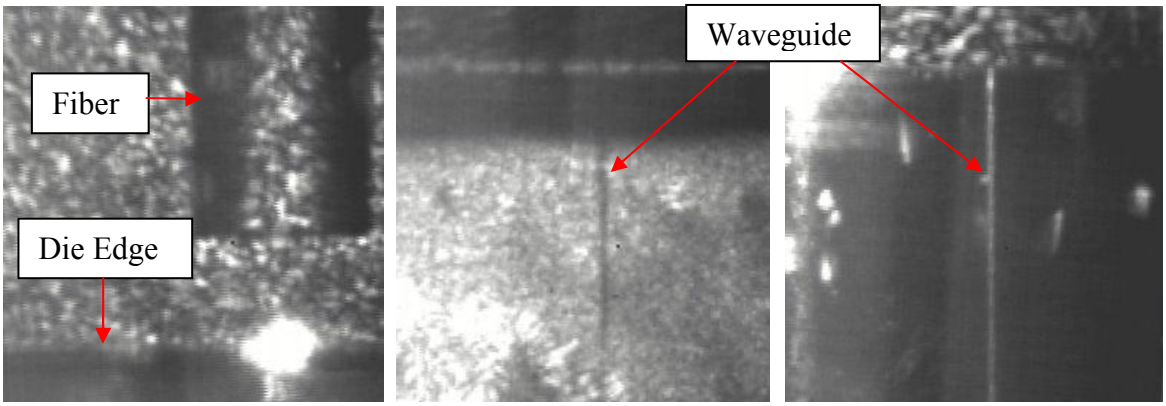

Figure 83. Input fiber illuminating die, fiber not alighted- no guiding, coupling condition

Once the y location of the fiber is determined the position of the input tip can be further optimized to increase coupling. If a cleaved fiber is used, the tip should be moved close to the edge of the die, if a micro lens or objective is used the spot should be focused on the edge of the die. Slight modifications to the rotation and tilt of the die can also improve coupling. Sensitivity to coupling in the x direction is very forgiving, as any light that enters the guiding silicon device layer will propagate and get trapped in the waveguide. In some cases better coupling may be achieved my moving the fiber slightly off x alignment, as the input facet may not be perfectly flat in the given location. If the image on the CRT is to bright the cameras exposure can be adjusted down. A picture of a portion of the single mode waveguide with the maximum achievable coupling that could be obtained is given in Figure 84 (exposure is set to half).

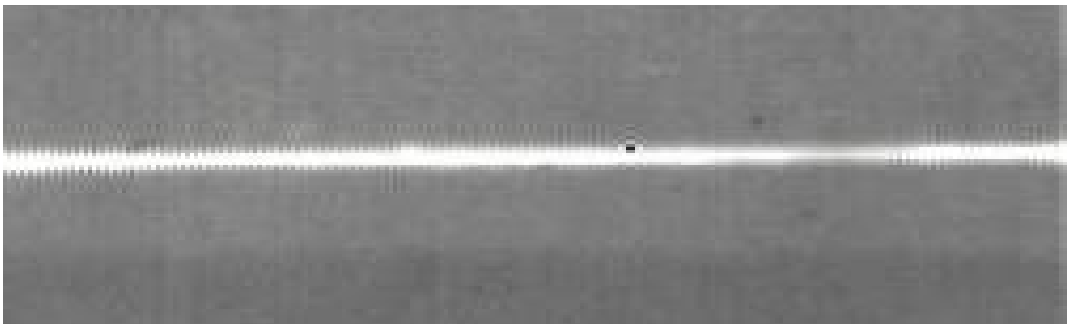

Figure 84. Single mode waveguide, with optimal coupling.

Using this procedure a large regain of the device can be visualized by taking several pictures as was done earlier, and stitching them together. The capture procedure was conducted for several of the designed structures, the 3dB splitter, MMI splitter, and y-splitter and can be seen in Figure 85 through Figure 88. The input to the structure is given on the left and the split output on the right. These images were captured with on a PC with an analog Hauppauge TV tuner. In each of these devices the leading waveguide is shortened by cleaving so that the behavior of splitting or coupling region can be easily observed. If this is not done too much light is lost by the time it reaches the splitting region for the camera to detect it. Further ways of reducing these losses will be described in the conclusion chapter of this thesis.

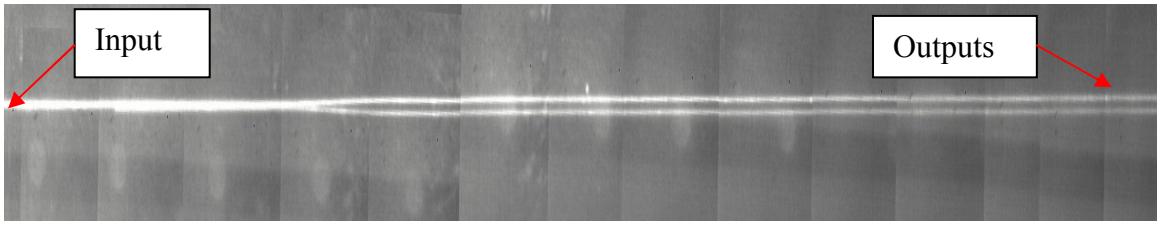

Figure 85. Operation of 3db coupler

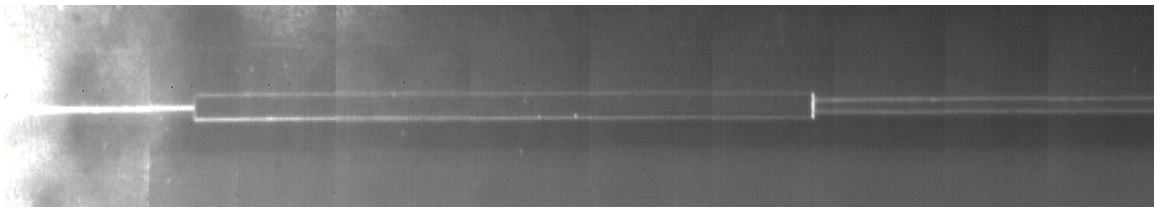

Figure 86. Operation of MMI coupler

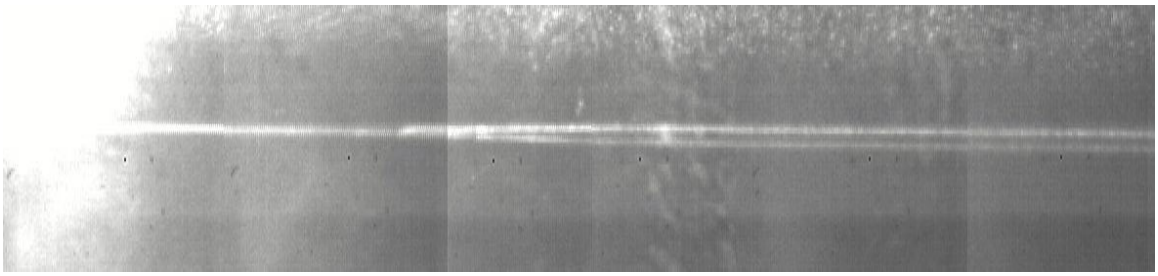

Figure 87. Operation of y-splitter s-curve

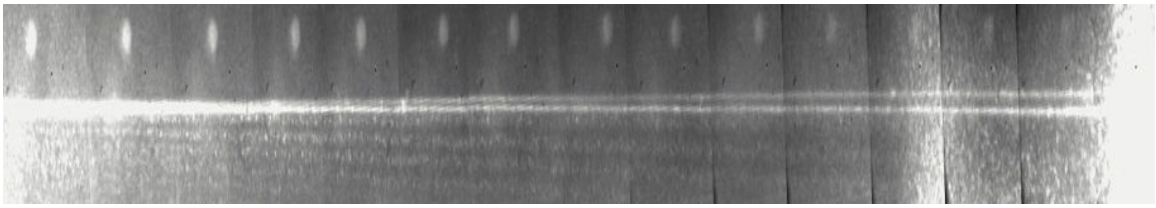

Figure 88. Operation of y-splitter linear curve

The setup for each of these pictures uses a cleaved input fiber with ASE source. The three guiding devices propagate light as expected, however are far from the ideal simulation. In the 3dB coupler splitting is not exactly 50-50; the intensity observed in the upper branch is slightly higher. This inconsistency can be attributed to fabrication variation. In the MMI coupler, there is a considerable amount of back reflection and scattering at the end of the multimode region. This type of scattering is caused by both fabrication variation in the MMI length, and the use of an input wavelength other then 1550nm for which the

device was designed. Because the ASE source is non-coherent much of the input signal will not be split. As the end of the multimode region does not corresponding to an image point of the input, the field will not couple into the output waveguides. Any portion of the field that does not couple into the output waveguides will either reflect back into the MMI region or scatter out into the air. The y-splitter, seen in Figure 88, provides more uniform splitting and lower losses then the MMI device, seen by the higher intensity in the output waveguides. This is expected due to the symmetric nature and wavelength independence of the y-branch. Although not shown the wavelength splitter was tested, its field distribution was similar to that of the 3dB coupler. A wavelength dependence however was not observed due to the high losses in a structure so long.

Several difficulties arose when attempting to quantify the operation of these devices by measuring their output power. It was found that regardless of where output fiber was located the maximum intensity measured stayed nearly constant between several hundred pico-watts to a few nano-watts. The intensity measured when the fiber was aligned with the waveguide was identical to the intensity when the fiber was several hundred micrometers away from it. This behavior is baffling as it is clear that light is propagating in the waveguide region but for some reason it could not be measured. Two major reasons are expected to be the cause. It was observed that a considerable amount light from the input fiber was being coupled into the substrate region of the die. This occurred because regardless of the input coupling method used the minimum spot size is still larger then the height of the device layer (1.2μm). As the substrate itself is confined on all four

sides by low index materials it behaves as a large slab waveguide propagating light to the other side of the die. The other reason contributing to the difficulty in measurement are the high losses which occur in the guiding region. This is evident as the observable propagation distances of most structures were no more then 5mm. The greatest indication of these losses is how bright the waveguide appears, implying that much of the light it is carrying is scattered by surface roughness. As a result of the small fraction of total power that enters the waveguide in addition to the high losses incurred during propagation it becomes nearly impossible to discern the output of the waveguide from that which has coupled into the substrate region. Further contributing to this problem are the high scattering losses at the exit facet of the waveguide. The size of the fiber used to capture light, so it can be measured by the OSA, also limits the resolution of the light distribution which can be measured. The reason that light propagating in the waveguide can be observed with the IR camera, but not easily measured with a fiber, is because the microscope and camera setup used is not only more sensitive but also has a higher spatial resolution. By looking at the setup top down the light in the substrate is effectively isolated from the field of view by the cladding layer.

Several options are available to avoid these problems so that quantitative parameters such as splitting ratio and loss per centimeter can be determined in future devices. The first improvement is to increase the amount of light that makes it into the waveguide by improving either coupling or alignment. This can be accomplished by taking advantage of methods such as v-grooves, or waveguide tapers. Reducing losses through methods

such as polishing or cleaving the output facet will reduce scattering which can improve measurement quality. The amount of light that enters the substrate region can be reduced by increasing the device layer thickness, and oxide thickness. By increasing these dimensions alignment will be less sensitive in the y axis. The impact of substrate guided modes can be avoided entirely by introducing a 90° bend. As light in the substrate is not guided by the waveguide it will always propagate straight through the die, where as light in the waveguide will change directions. For this reason the intensity in the substrate at the output of the waveguide bend should be relatively low. Although this is not a practical solution, it would be easy to fabricate and a good test to implement for future work.

A picture showing the output of a waveguide splitter is seen in Figure 89. The image on the left is illuminated with an ASE source, and the one on the right with a 1550nm source. In the lower left hand corner of each image is a tapered fiber being aligned with one of the output facets to be measured.

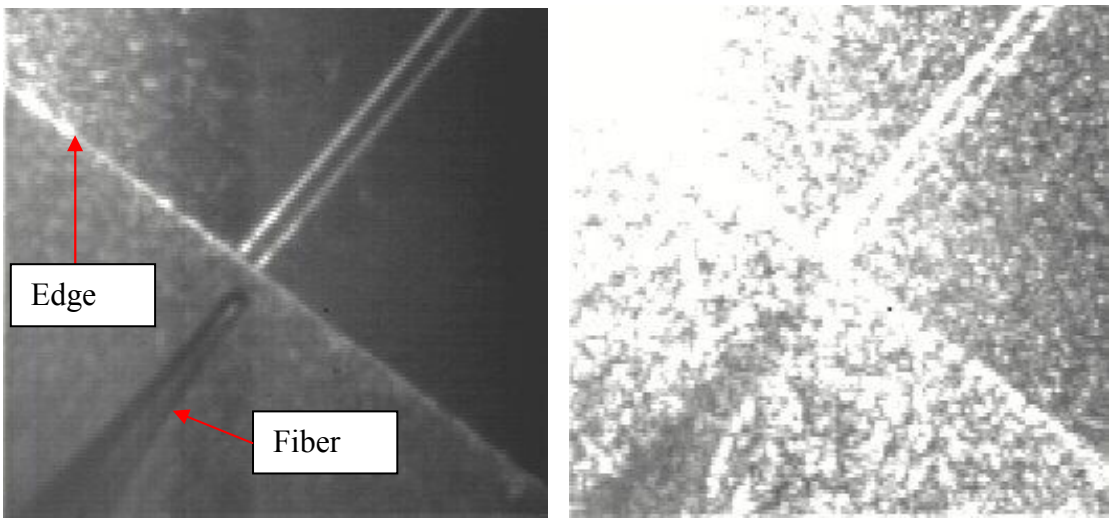

Figure 89. Output of coupler, ASE source (left) 1550 source (right)

The output edge of the die in these pictures is at a diagonal, due to the angle of the camera. It can be seen that light as strong or stronger the guided light is along most of the output edge. It is this light from the substrate that makes the waveguide output difficult to measure. The size of the fiber tip also gives a good representation of how difficult alignment can be. For the image on the right where a coherent source is used, at 6mw, it is difficult to observe the waveguide, due to interference (speckle). It is for this reason that the ASE source was used for the majority of testing.

Although further quantitative testing is limited, an attempt was made at viewing the side of the waveguide, with the second test apparatus diagramed in Figure 78. The most difficult aspect of this setup was properly aligning the fiber with the edge on the waveguide without a microscope. A picture of the sawed edge of a wafer at 25x observed through the infrared camera is given in Figure 90.

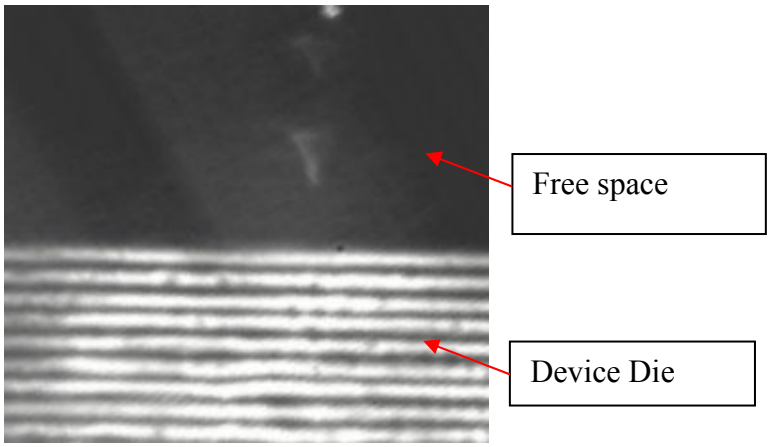

Figure 90. Edge of wafer under IR camera in secondary test set up

At this magnification it is not possible to resolve the waveguide crosses section which is only 0.8μm tall. The lines in the substrate region are caused by interface when the light reflects off the sides of the wafer. In this case the whole die is acting as a guiding structure and the interference is equivalent to the modal distribution of such a structure. It is clear that light is guided in the substrate region as light is confined. Although this test setup provides little information on the behavior of these structures, it has the potential to do so, if a higher magnification objective is adapted which can resolve the waveguide.

6.5 Summary

A test apparatus, testing produce, and the preliminary results have been presented in this chapter. Several methods were studied to improve insertion loss including changing the type of input and method of facet preparation. It was found that changing the type of input between tapered fiber, fiber lens, cleaved fiber, and microscope objective had little

impact on the observed coupling quality. Cleaving was determined to be the best method for preparing the waveguide facet, as polishing methods introduced more damage to the surface of the wafer then smoothing to the edge. Testing revealed that it was not possible to accurately measure the output intensity; however pictures showing the qualitative operation of each structure were obtained. The operation of the wavelength splitter could not be observed due to high losses that occurred in the long structure. Several methods for improving these results in future work are presented.

Chapter 7: Conclusion

7.1 Summary

The monolithic integration of optics and electronics on to a single substrate has the promise to solve many of the growing problems in electronics, particularly the increasing bandwidth requirements in microprocessors, and telecommunication networks. The advent of the SOI substrate may serve as the platform that connects these typically disconnected technologies.

In this thesis we have reviewed the potential of SOI as an integrated elecro-photonis platform, providing an evaluation of its current state of maturity. To prove the viability of

the technology several passive SOI rib waveguide structures including y-splitters, 3dB couplers, directional couplers, and MMI splitters have been designed, simulated, and tested with facilities available the Rochester Institute of Technology (RIT). During the design process an optimization method for waveguide couplers using a least squared regression is developed to reduce computation time, and characterize device operation. A fabrication process is developed to realize these waveguide structures, and the potential impacts of fabrication non-idealities are considered. Finally, the fabricated devices are tested with a specialized setup that is designed and built to align an input laser with the waveguide device and observe their operation. Although quantitative results could not be obtained because of poor output coupling, pictures of device operation are compiled.

7.2 Future Work

Several Changes to the design, fabrication and testing of these waveguide device should be considered to improve their performance, reliability and testability. These modifications will be discussed for future work. To make testing easier, particularly alignment of the fiber to the input waveguide, the use of waveguide tapers and/or v-grooves should be considered. The waveguide taper will increase the lateral tolerance, and the v-groove will help position the fiber. Further tolerance to testability can be added by using SOI wafers with thicker oxide and silicon device layers. These thicker films will over come the major disadvantage of the current design, a high sensitivity to y axis alignment. During future fabrication processes a pure aluminum should be used for the silicon etch hard mask. The use of pure aluminum will avoid several issues that were

encountered with impurity atoms disrupting the silicon etch and affecting waveguide uniformity. Any small particle or imperfection on a waveguide can greatly increase its losses. A further improvement of waveguide quality, with the end result of reducing losses, is achieved by using a smoothing method. Several oxidation techniques exist however the easiest reported are multiple RCA clean. It would also be possible to do this method on a per die bases after sawing or cleaving making it a versatile improvement that could be applied to even the current test wafer. The final fabrication improvement is the use of the Lam4600 plasma etcher for the first aluminm etch. Using a plasma etch in place of the current wet etch will reduce over etching, and better maintain waveguide width. Another approach would be to increase the design width of the waveguide structures to compensate for the anticipated width reduction.

Several test structures should be added to the layout as well, such as a ninety degree bend, and a larger waveguide (10μm) width. The ninety degree bend will provide a valid means to separate light from the substrate and guiding region, and the multimode waveguide can be used to further test the tolerance of input coupling to x location. The inclusion of additional structures such as the ring resonator, and etalon or grating filter should be considered. The testing of these structures can be improved by obtaining a better microscope setup, and characterizing the facet smoothening methods such as polishing and cleaving.

The over all trends in micro-optics are continuing towards developing and characterizing the passive components described in this thesis. Due to the demand for cheap telecommunication solutions, wavelength multiplexing structures and filters are continually being improved. Problems such as modulation on silicon, the silicon light source, and silicon photo detector in the NIR range, are still major issues that need to be refined before as valid SOI micro photonics platform can be realized.

References

[1] Allen Kent, and James G. *Williams, Encyclopedia of Computer Science and Technology: Volume 27 Supplement 12,* New York, Marcel Dekker Inc, 1999, pp. 181-200

[2] D.-X. Xu, P. Cheben, B. Lamontagne, S. Janz, and W. N. Ye, "Silicon-on-insulator (SOI) as a photonics platform," *207th ECS Meeting*, Dec 2004, Available: http://ecsmeet.peerx-press.org/ms_files/ecsmeet/2004/12/01/00004720/00/4720_0_art_file_0_1101916917_cnvpdf.pdf

[3] Wim Bogaerts, Roel Baets, Pieter Dumon, Vincent Wiaux, Stephan Beckx, Dirk Taillaert, Bert Luyssaert, Joris Van Campenhout, Peter Bienstman, and Dries Van Thourhout," Nanophotonic Waveguides in Silicon-on-Insulator Fabricated With CMOS Technology," *J. Of Lightwave Tech*., Vol. 23, No. 1, pp. 401-412, Jan 2005.

[4] Timo Aalto, "Microphotonic Silicon Waveguide Components." Doctoral Thesis, Technical Research center of Finland (VTT) in Espoo, Finland, 2004.

[5] William J. Dally, and John W. Poulton, *Digital Systems Engineering*, United Kingdom, Cambridge University Press, 2000, pp. 12-16

[6] L. Pavesi, "TOPICAL REVIEW: Will silicon be the photonic material of the third millenium?," *Journal of Physics: Condensed Matter,* Vol 15, Issue 26, pp. R1169-R1196, 2003

[7] Wai-Fah Chen, *The VlSI Handbook*, Boca Raton, Florida, CRC Press & IEEE Press, 2000, pp. 4-1 – 4-13

[8] K.E. Petersen, “Silicon as a Mechanical Material,” *Proceedings of the IEEE*, Vol. 70, No. 5, pp. 420-457, May 1982.

[9] Brigham Young University, “Wafer Formation,” Website: www.ee.byu.edu/cleanroom/EW_formation.phtml

[10] B. Jalali, S. Yegnanarayanan, T. Yoon, T. Yoshimoto, I. Rendina, and F. Coppinger, “Advances in Silicon-on-Insulator Optoelectronics,” *IEEE J. Quantum Electron.*, Vol 4, No. 6, pp. 938-946, Nov/Dec. 1998.

[11] D. Taillaert, R. Baets, P.Dumon, W. Wim Bogaerts, D. Van Thourhout, B. Luyssaert, V. Wiaux, S. Beckx, and J. Wouters, “Silicon-on-Insulator Platform for Integrated Wavelength-Selective Components,” *Proceedings of 2005 IEEE/LEOS Workshop on Fibers and Optical Passive Components*, pp. 115-120, Jun 2005.

[12] C.K. Tang, A.K. Kewell, G.T. Reed, A.G. Rickman, and F. Namavar, "Development of a library of low-loss silicon-on-insulator optoelectronic devices," *Proceedings from IEE Optoelectronics*, Vol.143, No.5, pp. 312-315, Oct 1996.

[13] Desmond Rodney Lim Chin Siong, “Device Integration For Silicon Micropotonic Platforms.” Doctoral Thesis, Massachusetts Institute of Technology, June 2000.

[14] Christopher C. Davis, *Lasers and Electro-optics: Fundamentals and Engineering*, United Kingdom, Cambridge University Press, 2000, pp. 472-475

[15] S. Abdalla, S. Ng, D. Celo, S. El-Mougy, T. Smy, and B. Syrett, “Optical switching in InGaAsP waveguides using localized index gradients,” *Journal of Vacuum Science & Technology A: Vacuum, Surfaces, and Films,* Vol. 22, No. 3, pp. 796-799, May 2004.

[16] G.T. Reed, "The optical age of silicon," *Nature*, Vol. 427, pp. 595-596, 2004.

[17] Jon Newey, "Optical modulators get ready for a high-speed network future," *Compound Semiconductor Magazine*, March 2002. Available: http://compound semiconductor.net/ zarticles/magazine/8/3/3/1

[18] Jasprit Singh, *Electronic and Optoelectronic Properties of Semiconductor Structures,* United Kingdom, Cambridge University Press, 2003

[19] William T. Silfvast, *Laser Fundamentals*, United Kingdom, Cambridge University Press, 2004, pp. 174-180

[20] Peter Capper, C T Elliott , *Infrared Detectors and Emitters: Materials and Devices*, Norwell, MA, Springer, 2001.

[21] J. I. Dadap, R. L. Espinola, R. M. Osgood, Jr., S. J. McNab, and Y. A. Vlasov, "Spontaneous Raman scattering in ultrasmall silicon waveguides," *Optical Society of America,* Vol. 29, pp. 2755-2757, 2004.

[22] Judy Hoyt, and L. Rafael Reif, "Growth and Processing of Strained Si/SiGe and Stress Effects on Devices," *6.774 Physics of Microfabrication: Front End Processing, Fall OpenCourseware Lecture,* 2004, Available: http://mfile.akamai.com/7870/rm/mitstorage.download.akamai.com/7870/6/6.774/ocw-6.774-02dec2004.rm

[23] J. Weber, L. Nebrich, F. Bensch, K. Neumeier, G. Vogg, R. Wieland, D. Bonfert and P. Ramm, "High quality strained Si / SiGe-Substrates for CMOS and Optical devices," Microelectronic engineering, Vol. 82, No. 3, pp. 215-220, March 2005.

[24] Graham T. Reed, and Andrew P. Knights, *Silicon Photonics: An Introduction,* West Sussex, England, John Wiley and Sons, 2004, pp. 1-249

[25] Mitsuo Fukuda, *Optical Semiconductor Devices,* New York, Wiley-IEEE, 1999, pp. 37-43

[26] Shigefusa F Chichibu, Shuji Nakamura, and Shigefusa Chichibu, *Introduction to Nitride Semiconductor Blue Lasers and Light Emitting Diodes,* New York, Taylor & Francis, 2000, pp. 4-8

[27] Perez-Arjona, G.J. de Valcarcel, and Eugenio Roldan, "Two Photon Absorption," *Revista Mexicana De Fisica*, Vol. 49, No. 1, pp. 91-100.

[28] Mitsuo Fukuda, *Optical Semiconductor Devices,* New York, Wiley-IEEE, 1999, pp. 37-43

[29] Sean Koehl, Victor Krutul, Dr. Mario Paniccia, "Continuous Silicon Laser Intel researchers create the first continuous silicon laser based on the Raman effect using standard CMOS technology," Intel White Paper, 2005. Available: ftp://download. intel.com/technology/silicon/sp/download/Silicon-Laser_WhitePaper.pdf

[30] S. Coffa, S. Libertino, G. Coppola, and A. Cutolo, "Feasibility analysis of laser action in erbium-doped silicon waveguides," *IEEE Journal of Quantum Electronics*, Vol. 36, No. 10, pp. 1206-1213, Oct 2000.

[31] Hei Wong, "Silicon integrated photonics: potentials and promises," *International Symposium on Electron Devices for Microwave and Optoelectronic Applications,* pp. 145-150, 17th Nov. 2003.

[32] A.G. Rickman, G.T. Reed, and F. Namavar, "Silicon-on-insulator optical rib waveguide loss and mode characteristics," *Journal of Lightwave Technology,* Vol. 12, No. 10, pp. 1771-1776, 1994.

[33] F. Grillot, L. Vivien, S. Laval, D. Pascal, and E. Cassan, "Size influence on the propagation loss induced by sidewall roughness in ultrasmall SOI waveguides," *IEEE Photonics Technology Letters*, Vol. 16, No. 7, pp. 1661-1663, July 2004.

[34] J.P.R. Lacey, and F.P. Payne, "A theoretical analysis of scattering loss from planar optical waveguides," *Optical and Quantum Electronics,* Vol. 26, No. 10, pp. 977-986, Oct. 1994.

[35] J.P.R. Lacey, and F.P. Payne, "Radiation loss from planar waveguides with random wall imperfections," *IEE Proceedings J. Optoelectronics*, Vol. 137, No. 4, pp. 282-288, Aug. 1990.

[36] Kevin K. Lee, Desmond R. Lim, Hsin-Chiao Luan, Anuradha Agarwal, James Foresi, and Lionel C. Kimerling, "Effect of size and roughness on light transmission in a Si/SiO2 waveguide: Experiments and model," *Applied Physics Letters*, Vol. 77, No. 11, pp.1617-1619, Sep. 2000.

[37] D.K. Sparacin, S.J. Spector, and L.C. Kimerling, "Silicon waveguide sidewall smoothing by wet chemical oxidation," *Journal of Lightwave Technology*, Vol. 23, No. 8, pp. 2455-2461, Aug. 2005.

[38] V.G. Ta'eed, D.J. Moss, and B.J. Eggleton, "Higher order mode conversion via focused ion beam milled Bragg gratings in Silicon-on-Insulator waveguides," *Optics Express*, Vol 12, No. 21, pp. 5274-5284, Oct. 2004.

[39] Y. Vlasov and S. McNab, "Losses in single-mode silicon-on-insulator strip waveguides and bends," *Opt. Express*, Vol. 12, No. 8, pp. 622-1631, April 2004.

[40] K. K. Lee, D. R. Lim, L. C. Kimerling, J. Shin, and F. Cerrina, "Fabrication of ultralow-loss Si/SiO2 waveguides by roughness reduction ," *Optical Letters,* Vol. 26, No. 23, pp. 1888-1890, Dec. 2001.

[41] Bhag Singh Guru, and Hüseyin R. Hiziroglu, *Electromagnetic Field Theory Fundamentals*, United Kingdom, Cambridge University Press, 2004.

[42] Eugene Hecht, *Optics Fourth Addition*, San Francisco, CA, Addison Wesley, 2002.

[43] Cooper Union Engineering lecture notes, "Optical Fibers as Open-Boundary Waveguides," Available: http://www.cooper.edu/engineering/projects/gateway/ee/solidmat/modlec4/node1.html

[44] ATIS, "Optical waveguide," Available: http://www.atis.org/tg2k/_optical_waveguide.html

[45] The Columbia Electronic Encyclopedia, Sixth Edition, Columbia University Press., 2003. Available: http://www.answers.com/topic/waveguide

[46] Tamir Theodor, *Guided-Wave Optoelectronics,* Germany, Springer-Verlag, Dec. 1990, pp. 1-200.

[47] OptiFDTD Technical Background and Tutorials on Finite Difference Time Domain Photonics Simulation Software, Optiwave, 2005. pp. 15-26.

[48] Kenji Kawano, Tsutomu Kitoh, *Introduction to Optical Waveguide Analysis: Solving Maxwell's Equation and the Schrödinger Equation*, New York, John Wiley & Sons, 2001, pp. 15-30.

[49] S.P Pogossian, L. Vescan, and A.Vonsovici, "The single-mode condition for semiconductor rib waveguides with large cross section," *Journal of Lightwave Technology*, Vol. 16, No. 10, pp. 1851-1853, Oct. 1998.

[50] Jinsong Xia, Jinzhong Yu, Yanping Li, and Shaowu Chen, "Single-mode condition for silicon rib waveguides with large cross sections," Optical Engineering, Vol. 43, No. 9, pp. 1953-1954, Sep. 2004.

[51] Seong Phun Chan, Soon Thor Lim, G.T Reed, and V.M.N Passaro, "Single-mode and polarization-independent silicon-on-insulator waveguides with small cross section," *Journal of Lightwave Technology*, Vol. 23, No. 6, pp. 2103-2111, June 2005.

[52] R.A. Soref, J. Schmidtchen, and K. Petermann, "Large single-mode rib waveguides in GeSi-Si and Si-on-SiO2," *IEEE Journal of Quantum Electronics*, Vol. l27, No. 8, pp. 1971-1974, Aug 1991.

[53] L.B Soldano, and E.C.M Pennings, "Optical multi-mode interference devices based on self-imaging: principles and applications," J. of Lightwave Tech., Vol. 13, No.4, pp. 615-627, April 1995.

[54] Tao Liu, A.R. Zakharina, M. Fallahi, and M. Mansuripur, Optical Data Storage Center, "Multimode Interference-Baced Photonic Crystal Beam-splitter," Available: http://www.optics.arizona.edu/ODSCsponsors/03-10-9IABFALLMEETING/C3-Mansuripur-Liu-Multimode%20Interference-Oct.%202003.pdf

[55] R. Hanfoug, L. M. Augustin, Y. Barbarin, J.J.G.M. van der Tol, E.A.J.M Bente, F. Karouta, D. Rogers, Y.S. Oei, X.J.M. Leijtens and M.K. Smit, "A Multimode Interference coupler with low reflections," *IEEE Lasers and Electro-Optics Society*, 2005.

[56] Edmond J Murphy, *Integrated Optical Circuits and Components: Design and Applications,* New York, Lucent Technologies, 1999, pp. 183-185.

[57] Martin Reed, "The free space radiation mode method in integrated optics." Doctoral Thesis, University of Nottingham, Nottingham, UK, May 1998.

[58] Kin Seng Chiang, Chung Ho Kwan, and Kai Ming Lo, "Effective-index method with built-in perturbation correction for the vector modes of rectangular-core optical waveguides," *Journal of Lightwave Technology*, Vol. 17, No. 4, pp. 716-722, Apr. 1999.

[59] Stephen Greedy, "*Advances in the Spectral Index Method for Optoelectronic design.*" Doctoral Thesis, University of Nottingham, Nottingham UK, 2002. pp. 38-45

[60] Allen Taflove, "Application of the Finite-Difference Time-Domain Method to Sinusoidal Steady-State Electromagnetic-Penetration Problems," *IEEE Transactions On Electromagnetic Compatibility*, Vol. 22, No. 3, pp. 191-202, Aug 1980

[61] OptiBPM Technical Background and Tutorials Waveguide Optics Modeling Software Systems, Optiwave, 2005, pp. 13-18.

[62] Alan Kost, "Lecture notes on Beam Propagation Method," The university of Arizona Optical Sciences Center. Available: http://www.optics.arizona.edu/kost/OPTI% 20515%20Web%20Site/Lecture%20Notes/Lecture%2013%20BPM%20Method.pdf

[63] Hyper textbook, "Diameter of an optical fiber," Available: http://hypertextbook.com /facts/1997/LaurenBoyd.shtml

[64] LASER Components (UK) Ltd. "Lens Theory," Available: http://www.laser components .co.uk/wwwuk/faq/linsth.htm

[65] Chih-Wei Hsu, Hsuen-Li Chen, and Way-Seen Wang, "Compact Y-branch power splitter based on simplified coherent coupling," *IEEE Photonics Technology Letters*, Vol. 15, No. 8, pp. 1103-1105, Aug. 2003.

[66] Optiwave, "Optimization: Design a 3dB Coupler using a Bisection Algorithm," Available: http://www.optiwave.us/bpm/Coupler%203dB/Coupler3dB.htm

[67] Indra Januar and Alan R. Mickelson, "Dual-wavelength (λ=1300-1650nm) directional coupler multiplexer-demultiplexer by the annealed-proton-exchange process in $LiNbO_3$," *Optics Letters*, Vol. 18, No. 6, pp. 417-419, March 1993.

[68] Wolfarm Mathworld, "Least Squares Fitting," Available: http://mathworld. wolfram.com/LeastSquaresFitting.html

[69] A.L. Campillo, J.W.P. Hsu, K.R. Parameswaran, and M. M. Fejer, "Direct imaging of multimode interference in a channel waveguide," *Optics Letters*, Vol. 28, No. 6, pp. 399-401, March 2003.

[70] Kyung-Sook Hyun, Byueng-Su Yoo, Jeong-Soo Kim, and Ilgu Yun, "1×8 Channel Power Splitter Using a Multimode Interference Coupler in InP/InGaAsP," *J. Appl. Phys.,* Vol. 40, No. 5A, pp. L443-L445, May 2001.

[71] Christopher Saint, and Judy Saint, *IC Mask Design,* New York, McGraw-Hill, 2002. pp.20-25.

[72] Maurizio Valle, *Smart Adaptive Systems on Silicon,* Boston, MA, Kluwer Academic Publishers, 2004, pp. 50-56.

[73] Vishal Shrotriya, Silicon On Insulator (SOI) Wafer Fabrication And concerns. Available: http://www.seas.ucla.edu/~vshro/files/MSE%20298%20SOI.pdf

[74] Ultrasil Corporation, Wafer specifications. Available: http://www.ultrasil.com/

[75] Shari Farrens, Viorel Dragoi, Paul Lindner, and Bernhard Wieder, "Chip manufactures look to wafer-bonding technology," *Compound Semiconductor Magazine*, Sep. 2002. Available: http://compound semiconductor.net/ zarticles/magazine/8/9/3/1

[76] Edward V Barnat, and Toh-Ming Lu, *Pulsed and Pulsed Bias Sputtering: Principles and Applications*, Norwell, MA, Kluwer Academic Publishers, 2003. pp. 1-13.

[77] RIT SFML, ARC product overview. Available: http://appserver.microe.rit.edu/ classes/emcr666_676/reference/arcs/Product_Overview_arcs.pdf

[78] RIT SFML, XL ARC Data Sheet. Available: http://appserver.microe.rit.edu/classes/ emcr666_676/reference/arcs/XL%20Data%20Sheet_barc.pdf

[79] RIT SFML, Process capabilities SSI Track-Coat Process. Available: http://smfl.microe .rit.edu/Process%20Information/SSI%20SMFLCOAT.pdf

[80] RIT SFML, Process capabilities SSI Track-Coat Develop. Available: http://smfl. microe.rit.edu/Process%20Information/SSI%20SMFLDEV.pdf

[81] Jerome J Cuomo, Stephen M Rossnagel, and William D Westwood, *Handbook of Plasma Processing Technology,* Norwich, New York, William Andrew Inc., 1990. pp. 196-204.

[82] Sensors Unlimited Inc, SU128-1.7T` InGaAs NIR Focal Plane Arrays. Available: http://www.astrainc.co.jp/Datasheet/SUI/FPA/SU12817T1FPAREV403.pdf

Appendix A: Mathcad sheet used to determine the single more condition

$n1 := 3.45 \qquad \gamma o := 1 \qquad um := 10^{-6} \qquad b := 0, .001 .. 4$

$no := 1 \qquad \gamma 2 := 1 \qquad \lambda := 1.33 \cdot um \qquad r := .6$

$n2 := 1.44$

$$q := \left(\frac{\gamma o}{\sqrt{n1^2 - no^2}} + \frac{\gamma 2}{\sqrt{n1^2 - n2^2}} \right)$$

$$adivb1(b) := \left(\frac{q + 4 \cdot \pi \cdot b}{4 \cdot \pi \cdot b} \right) \cdot \frac{1 + 0.3 \cdot \sqrt{\left(\frac{q + 4 \cdot \pi \cdot b}{q + 4 \cdot \pi \cdot r \cdot b} \right)^2 - 1}}{\sqrt{\left(\frac{q + 4 \cdot \pi \cdot b}{q + 4 \cdot \pi \cdot r \cdot b} \right)^2 - 1}}$$

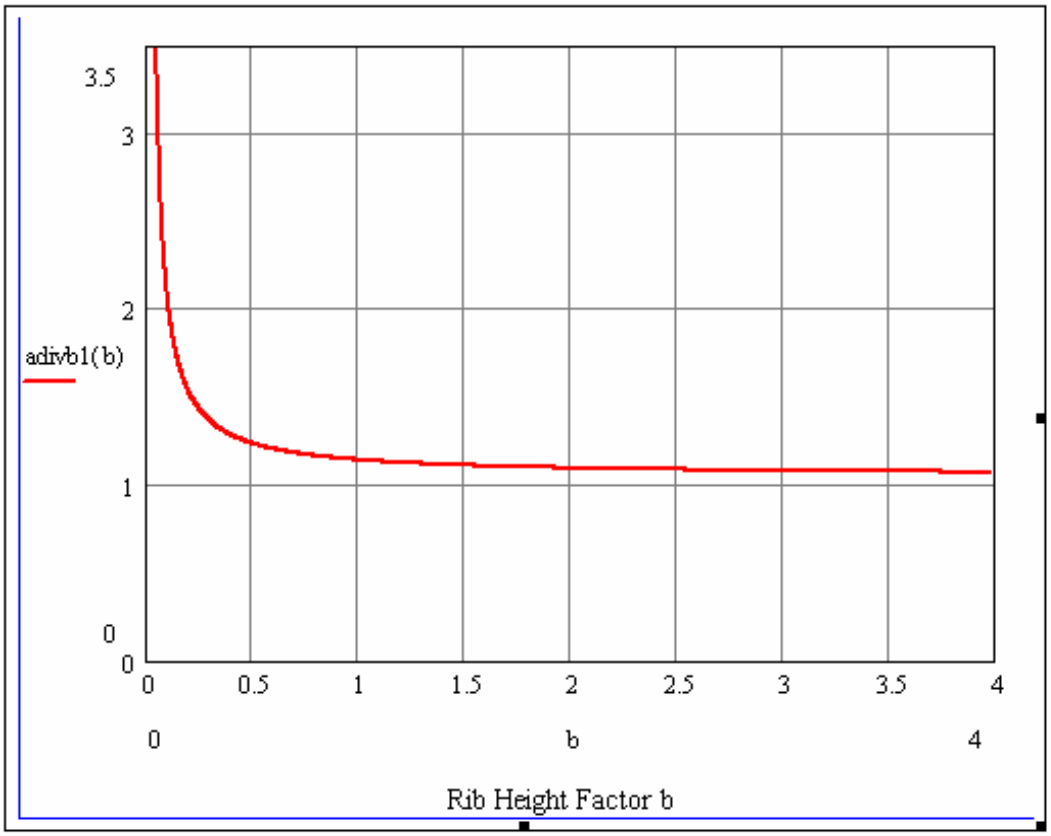

Appendix B: Optiwave script used to optimize the design of the 3dB coupler.

```
‘Script to generate 3dB coupler with 30µm output separation, 2.5µm separation in the
      coupling region and an transition region of 6000µm
‘
_____________________________________________________________________

WGMgr.DeleteAll

InputPlaneMgr.DeleteAll

‘Define thin silicon layer

Dim RegionSubstrate1
Set RegionSubstrate1 = WGMgr.CreateObj ( "RegionSubstrate", "RegionSubstrate1" )
RegionSubstrate1.SetZPosition    0, 17000
RegionSubstrate1.SetAttr "PropStep", "1.0"
RegionSubstrate1.SetAttr "RefIndex", "1.0"
RegionSubstrate1.SetAttr "PropStepGlobal", True
RegionSubstrate1.SetAttr "RefIndexGlobal", True
RegionSubstrate1.SetAttr "SubThickness", "5"
RegionSubstrate1.SetAttr "GlobalSubThickness", True
RegionSubstrate1.SetAttr "SubMaterial", "Substrate"
RegionSubstrate1.SetAttr "GlobalSubMaterial", True
RegionSubstrate1.SetAttr "CladMaterial", "Substrate"
RegionSubstrate1.SetAttr "GlobalCladMaterial", True
RegionSubstrate1.SetAttr "2DMaterial", "Substrate"
RegionSubstrate1.SetAttr "Global2DMaterial", True
RegionSubstrate1.AddRegionLayer "Bottomthic","Bottomthic","Layer"

 ‘Define output bends

Dim SBendSin1
Set SBendSin1 = WGMgr.CreateObj ( "WGSBendSin", "SBendSin1" )
SBendSin1.SetAttr "AngleOffset", CDbl( 0.000000 )
SBendSin1.SetPosition 10490,    0, 16490,   15
SBendSin1.SetAttr "WidthExpr", "Topwid"
SBendSin1.SetAttr "Depth", "0"
SBendSin1.SetAttr "StartThickness", "2.000000"
SBendSin1.SetAttr "EndThickness", "2.000000"
SBendSin1.SetProfileName "Ridgeguide"
SBendSin1.SetDefaultThicknessTaperMode True

Dim SBendSin2
Set SBendSin2 = WGMgr.CreateObj ( "WGSBendSin", "SBendSin2" )
```

```
SBendSin2.SetAttr "AngleOffset", CDbl( 0.000000 )
SBendSin2.SetPosition 10490, -4.5, 16490, -19.5
SBendSin2.SetAttr "WidthExpr", "Topwid"
SBendSin2.SetAttr "Depth", "0"
SBendSin2.SetAttr "StartThickness", "2.000000"
SBendSin2.SetAttr "EndThickness", "2.000000"
SBendSin2.SetProfileName "Ridgeguide"
SBendSin2.SetDefaultThicknessTaperMode True

‘Define linear coupling reagions, and output ports

Dim Linear1
Set Linear1 = WGMgr.CreateObj ( "WGLinear", "Linear1" )
Linear1.SetPosition    0,    0, 10490,    0
Linear1.SetAttr "WidthExpr", "Topwid"
Linear1.SetAttr "Depth", "0"
Linear1.SetAttr "StartThickness", "2.000000"
Linear1.SetAttr "EndThickness", "2.000000"
Linear1.SetProfileName "Ridgeguide"
Linear1.SetDefaultThicknessTaperMode True

Dim Linear2
Set Linear2 = WGMgr.CreateObj ( "WGLinear", "Linear2" )
Linear2.SetPosition  490, -4.5, 10490, -4.5
Linear2.SetAttr "WidthExpr", "Topwid"
Linear2.SetAttr "Depth", "0"
Linear2.SetAttr "StartThickness", "2.000000"
Linear2.SetAttr "EndThickness", "2.000000"
Linear2.SetProfileName "Ridgeguide"
Linear2.SetDefaultThicknessTaperMode True

Dim Linear3
Set Linear3 = WGMgr.CreateObj ( "WGLinear", "Linear3" )
Linear3.SetPosition 16490,   15, 17000,   15
Linear3.SetAttr "WidthExpr", "Topwid"
Linear3.SetAttr "Depth", "0"
Linear3.SetAttr "StartThickness", "2.000000"
Linear3.SetAttr "EndThickness", "2.000000"
Linear3.SetProfileName "Ridgeguide"
Linear3.SetDefaultThicknessTaperMode True

Dim Linear4
Set Linear4 = WGMgr.CreateObj ( "WGLinear", "Linear4" )
Linear4.SetPosition 16490, -19.5, 17000, -19.5
```

```
Linear4.SetAttr "WidthExpr", "Topwid"
Linear4.SetAttr "Depth", "0"
Linear4.SetAttr "StartThickness", "2.000000"
Linear4.SetAttr "EndThickness", "2.000000"
Linear4.SetProfileName "Ridgeguide"
Linear4.SetDefaultThicknessTaperMode True

‘Define input field profile

Dim InputPlane1
Set InputPlane1 = InputPlaneMgr.CreateObj ( "Mode", "InputPlane1" )
InputPlane1.SetZPosition    1
InputPlane1.SetReferenceIndexWaveguide2D "Unknown"
InputPlane1.SetReferenceIndexWaveguide3D "Linear1"
Set InputFieldMode1 = InputPlane1.CreateInputField ( "3D" , "Mode" ,
      "InputFieldMode1" )
InputFieldMode1.SetWaveguideID  "Linear1"
InputFieldMode1.SetAmplitude  "1.0"
InputFieldMode1.SetPhase  "0.0"
InputFieldMode1.SetTiltAngleType  "Auto"
InputFieldMode1.SetTiltIndexType  "Modal"
Set InputFieldGauss1 = InputPlane1.CreateInputField ( "3D" , "Gaussian" ,
      "InputFieldGauss1" )
InputFieldGauss1.SetWaveguideID  "Linear1"
InputFieldGauss1.SetAmplitude  "1.0"
InputFieldGauss1.SetPhase  "0.0"
InputFieldGauss1.SetTiltAngleType  "Auto"
InputFieldGauss1.SetTiltIndexType  "Average"
InputFieldGauss1.SetCenterX  "0.0"
InputFieldGauss1.SetCenterY  "0.0"
InputFieldGauss1.SetWidthTypeX  "Auto"
InputFieldGauss1.SetWidthTypeY  "Auto"
InputPlane1.SetEnabled  TRUE
‘
```

```
Topwidth = 2
Topthick = 0.8    'set top rib height
Bottomthick = 1.2   'set thin film height
Wavelength =1.55   'set desired propagation wavelength

ParamMGR.SetParam "Topwid", Cstr(Topwidth)      'apply parameters
ParamMGR.SetParam "Bottomthic", Cstr(Bottomthick)
ParamMGR.SetParam "Topthic", Cstr(Topthick)
ParamMGR.SetParam "Lamda", Cstr(Wavelength)
```

```
'--------------------------------------------------

Dim L2, x, StepSize, sep        'define variables
Const NumIterations =50         'set number of iterations, as a constant
Set L2 = WgMgr.GetObjFromID("Linear2")  'define object to be modified
StepSize = 200   'set step size
sep=-4.5    'waveguide separation

‘loop that controls the length of the coupling region between each iteration

For x=1 to NumIterations        'loop for Numiteration
   Dim Linear2     're-define linear region that is to move, fixes scripting bug
   Set Linear2 = WGMgr.CreateObj ( "WGLinear", "Linear2" )
   Linear2.SetPosition  200, sep, 6490, sep
   Linear2.SetAttr "WidthExpr", "Topwid"
   Linear2.SetAttr "Depth", "0"
   Linear2.SetAttr "StartThickness", "2.000000"
   Linear2.SetAttr "EndThickness", "2.000000"
   Linear2.SetProfileName "Ridgeguide"
   Linear2.SetDefaultThicknessTaperMode True

   L2.SetPosition  10490-(StepSize*x), sep, 10490, sep   'change length of linear

   ParamMGR.Simulate       'inishate bpm simulator
   WGMgr.Sleep( 50 )       'pause before next iteration

Next       'next loop
```

Appendix C: Script used to obtain output power for varying values of S and L at two different wavelengths.

```
 Wavelength = 1.55 ‘define parameters
Topwidth = 2
Topthick = 0.8
Bottomthick = 1.2

ParamMGR.SetParam "Topwid", Cstr(Topwidth)      ‘set parameters
ParamMGR.SetParam "Bottomthic", Cstr(Bottomthick)
ParamMGR.SetParam "Topthic", Cstr(Topthick)
ParamMGR.SetParam "Lamda", Cstr(Wavelength)

'--------------------------------------------------
Dim x, StepSize, f, y, sep
StepSize = 147
sep = 0.1
x=6

sep=1.4

For x=1 to 10         ‘sweep waveguide separation
   for y=1 to 40          ‘sweep coupling length
      Dim Linear2
      Set Linear2 = WGMgr.CreateObj ( "WGLinear", "Linear2" )
      Linear2.SetPosition  200, -3.4, 4000, -3.4
      Linear2.SetAttr "WidthExpr", "Topwid"
      Linear2.SetAttr "Depth", "0"
      Linear2.SetAttr "StartThickness", "2.000000"
      Linear2.SetAttr "EndThickness", "2.000000"
      Linear2.SetProfileName "Ridgeguide"
      Linear2.SetDefaultThicknessTaperMode True
      Linear2.SetPosition  13900-8000-(cl), -4+(2-sep), 13900-8000, -4+(2-sep)
      Dim SBendSin2
      Set SBendSin2 = WGMgr.CreateObj ( "WGSBendSin", "SBendSin2" )
      SBendSin2.SetAttr "AngleOffset", CDbl( 360.000000 )
      SBendSin2.SetPosition 13900-8000,   -4, 19900-8000, -7.4
      SBendSin2.SetAttr "WidthExpr", "Topwid"
      SBendSin2.SetAttr "Depth", "0"
      SBendSin2.SetAttr "StartThickness", "2.000000"
      SBendSin2.SetAttr "EndThickness", "2.000000"
      SBendSin2.SetProfileName "Ridgeguide"
      SBendSin2.SetDefaultThicknessTaperMode True
```

```
        SBendSin2.SetPosition  13900-8000, -4+(2-sep), 19900-8000-5500, -10+(2-sep)
        Dim Linear4
        Set Linear4 = WGMgr.CreateObj ( "WGLinear", "Linear4" )
        Linear4.SetPosition  -10,   -3, 4600,   -3
        Linear4.SetAttr "WidthExpr", "Topwid"
        Linear4.SetAttr "Depth", "0"
        Linear4.SetAttr "StartThickness", "2.000000"
        Linear4.SetAttr "EndThickness", "2.000000"
        Linear4.SetProfileName "Ridgeguide"
        Linear4.SetDefaultThicknessTaperMode True
        Linear4.SetPosition  19900-8000-5500, -10+(2-sep), 20000-8000-5500, -10+(2-sep)

        Wavelength = 1.55
        ParamMGR.SetParam "Lamda", Cstr(Wavelength)
        ParamMGR.Simulate
        WGMgr.Sleep( 50 )

        Wavelength = 0.98
        ParamMGR.SetParam "Lamda", Cstr(Wavelength)
        ParamMGR.Simulate
        WGMgr.Sleep( 50 )

    next
next
```